CREATING COMPETING CHARGE-TRANSFER PATHWAYS FOR WATER OXIDATION PHOTOCATALYSIS

A THESIS SUBMITTED TO THE GRADUATE SCHOOL OF ENGINEERING AND SCIENCE OF BILKENT UNIVERSITY IN PARTIAL FULFILLMENT OF THE REQUIREMENTS FOR THE DEGREE OF MASTER OF SCIENCE IN CHEMISTRY

By Hüseyin Orhun TUNÇER

July 2025

CREATING COMPETING CHARGE-TRANSFER PATHWAYS FOR WATER OXIDATION PHOTOCATALYSIS

By Hüseyin Orhun TUNÇER

July 2025

We certify that we have read this thesis and that, in our opinion, it is fully adequate, in scope and in quality, as a thesis for the degree of Master of Science.

_____

Ferdi Karadaş (Advisor)

_____

Emrah Özensoy

_____

Ömer Dağ

_____

Fahri Alkan

_____

Salih Özçubukçu

Approved for the Graduate School of Engineering and Science:

_____

Orhan Arıkan

Director of the Graduate School

ABSTRACT

CREATING COMPETING CHARGE-TRANSFER PATHWAYS FOR WATER OXIDATION PHOTOCATALYSIS

Hüseyin Orhun TUNÇER

M.S. in Chemistry

Advisor: Ferdi Karadaş

July 2025

Replacing fossil fuels with renewable energy requires scalable and economic catalysts. However, solar conversion to chemical energy is heavily dependent on rare-earth metal-based photosensitizers and catalysts. Thus, it is necessary to build photocatalytic dyads that consist of first-row transition metals. However, Fe(II) polypyridyls, unlike their Ru(II) and Ir(III) analogues, show weak octahedral field splitting, which changes the photophysics to be unfavorable for catalysis. In this thesis, we focused on coupling metal-to-ligand charge transfer (MLCT) states with metal-to-metal charge transfer (MMCT) states to improvethe water oxidation catalytic activityof Prussian blue analogue(PBA) based photocatalysts.

We first synthesised two of the most commonly studied Fe(II) polypyridyls, $Fe(bpy)_2(CN)_2$ and $K_2Fe(bpy)(CN)_4$. Then we coupled these chromophores with $[Co(bpy)(H_2O)_n]^{2+}$ and $[Zn(bpy)(H_2O)_n]^{2+}$ groups to prepare FeCo and FeZn compounds. FeZn compounds are used as a reference to investigate Fe cyanopolypyridyls in a network system since Zn ions are not expected to exhibit MMCT. With FeCo systems, it isaimed to investigate the role of the MMCT on the decay dynamics of the MLCT process. Characterization studies show that the local environment of Fe sites is affected by the coordination of Co and Zn ions to the cyanide bridge, resulting in a stabilization of the t_{2g} and e_g levels. We performed a series of photocatalytic experiments revealing that the highest catalytic activity is achieved for systems that possess MMCT processes directly coupled with the MLCT process through cyanide bridging group. Ultrafast transient absorption experiments indicate that the photophysics of the MLCT process is significantly different in Fe and FeCo compounds since ^{5}MC is stabilized in energy compared to the ^{3}MC state,

and MMCT serves as an alternate relaxation pathway for the excited MLCT state. Finally, we combined our experimental findings to establish Jablonski diagrams for Fe, FeZn, and FeCo compounds and further proposed a mechanism for the photocatalytic water oxidation process.

This thesis indicates that the cyanide bridge could provide an ideal platform to couple different charge transfer processes due to its rigid and short nature. The results also suggest that combining charge transfer processes could be a viable pathway to favor the decay dynamics of MLCT states for photocatalytic applications.

ÖZET

FOTOKATALİTİK SUYUN YÜKSELTGENMESİ İŞLEMİ İÇİN REKABETÇİ YÜK-TRANSFERİ YOLLARININ OLUŞTURULMASI

Hüseyin Orhun TUNÇER

Kimya, Yüksek Lisans

Tez Danışmanı: Ferdi Karadaş

Temmuz 2025

Fosil yakıtların yenilenebilir enerji ile değiştirilmesi ölçeklenebilir ve ekonomik katalizörler gerektirir. Bununla birlikte, güneş enerjisinin kimyasal enerjiye dönüşümü büyük ölçüde nadirmetal bazlı fotosensitizörlere ve katalizörlere bağlıdır. Bu nedenle, birinci sıra geçiş metallerinden oluşan fotokatalitik ikililer oluşturmak gereklidir. Ancak, Fe(II) polipiridilleri, Ru(II) ve Ir(III) analoglarının aksine, fotofiziği kataliz için elverişsiz olacak şekilde değiştiren zayıf oktahedral alan bölünmesi gösterir. Bu tezde, Prusya Mavisi Analoğu (PBA) bazlı fotokatalizörlerin su oksidasyonu katalitik aktivitesini iyileştirmek için metalden liganda yük transferi (MLCT) durumlarını metalden metale yük transferi (MMCT) durumlarıyla birleştirmeye odaklandık.

İlk olarak en sık çalışılan Fe(II) polipiridillerinden ikisini, $Fe(bpy)_2(CN)_2$ ve $K_2Fe(bpy)(CN)_4$'ü sentezledik. Daha sonra bu kromoforları $[Co(bpy)(H2O)_n]^{2+}$ ve $[Zn(bpy)(H_2O)_n]^{2+}$ grupları ile birleştirerek FeCo ve FeZn bileşiklerini hazırladık. FeZn bileşikleri, MMCT sergilemeleri beklenmediğinden ağ sistemlerindeki Fe siyanopolipiridiller için referans olarak kullanılmaktadır. FeCo sistemleri ile MMCT'nin MLCT sürecinin bozunma dinamikleri üzerindeki rolünün araştırılması amaçlanmıştır. Karakterizasyon çalışmaları, Fe bölgelerinin yerel ortamının Co ve Zn iyonlarının siyanür köprüsüne koordinasyonundan etkilendiğini ve bunun da t_{2g} ve e_g seviyelerinin stabilizasyonuyla sonuçlandığını göstermektedir. Bir dizi fotokatalitik deney gerçekleştirdik ve en yüksek katalitik aktivitenin MMCT süreçlerine sahip olan ve siyanür köprü grubu aracılığıyla MLCT sürecine doğrudan bağlanan sistemler için elde edildiğini ortaya koyduk. Ultra hızlı geçici absorpsiyon deneyleri, MLCT sürecinin fotofiziğinin Fe ve FeCo bileşiklerinde önemli ölçüde

farklı olduğunu, çünkü ^{5}MC'nin ^{3}MC durumuna kıyasla enerjide stabilize olduğunu ve MMCT'nin uyarılmış MLCT durumu için alternatif bir gevşeme yolu olarak hizmet ettiğini göstermektedir. Son olarak, Fe, FeZn ve FeCo bileşikleri için Jablonski diyagramları oluşturmak üzere deneysel bulgularımızı birleştirdik ve fotokatalitik su oksidasyon süreci için bir mekanizma önerdik.

Bu tez, siyanür köprüsünün sert ve kısa yapısı nedeniyle farklı yük aktarım süreçlerini birleştirmek için ideal bir platform sağlayabileceğini göstermektedir. Sonuçlar ayrıca, yük aktarım süreçlerinin birleştirilmesinin, fotokatalitik uygulamalar için MLCT durumlarının bozunma dinamiklerini desteklemek için uygun bir yol olabileceğini göstermektedir.

ACKNOWLEDGEMENTS

I would like first to thank my advisor, Ferdi Karadaş. Without him, I would not be able to achieve what I have done with this work and learn what I did. Thanks to him, I was able to learn most of what I know about metallorganic and cyanide-based inorganic compounds. Through studies I did in our group, I was able to learn about various characterization and experimentation techniques. And using my knowledge, I could interpret the experiments I did. When I was doing obvious wrongs, he was very patient and understanding with me. He was very helpful in teaching me concepts that I, sometimes even he, was unfamiliar with. Through his encouragement and recommendations, I went to several conferences and networking events to enhance my networking and expand my scientific view. I was also able to co-write two successful proposals for a last-generation synchrotron, SESAME. I am so glad to be in his lab and be his student. An advisor like him is very hard to come by.

I am grateful to the dear thesis committee members, Prof. Emrah Özensoy, Prof. Ömer Dağ, Asst. Prof. Fahri Alkan and Assoc. Prof. Salih Özçubukçu. I would like to thank them for taking their valuable time to comment on my thesis. And I appreciate any of their comments.

I would like to first thank Aliyu Ahmad and Yaren Yapalak for their efforts on this project. Before I began working on this project, they laid out the essentials of this study. I want to thank Prof. Benjamin Dietzek-Ivansic and his doctoral student, Dr. Ratnadip De, for collaborating on photophysics experiments. Without their experiment and very valuable analysis, we would not have been able to understand our compounds to this degree. Their valuable comments also taught us about how we should approach our photocatalytic systems as well. I would like to thank Dr. De for his significant contribution to the TAS studies part of this thesis.

I would like to also thank SESAME and TENMAK for financially supporting the 20240201 numbered project. I also thank TÜBİTAK for their financial support under the project of "TÜBİTAK 122N434" with the name of "Fonksiyonel Bileşenlerle Modifiye Edilen Yarıiletken Karbondioksitin Fotokatalitik Yöntemle C2+ Ürünlere Dönüştürülmesinde Kullanılması".

Dr. Sina Sadigh Akbari is a valuable member of our group. Thanks to him, I was able to learn the fundamentals of characterisation and synthesis of catalysts, as well

as understand the roads that lead to good catalysis. I would also like to thank him for his significant contribution to XPS analysis.

I would like to thank Dr. Mustafa Fatih Genişel, as our brief discussions allowed me to see that I had so much to learn. But these discussions also showed me the direction I want to go in. I would also like to thank him for helping with our XAS measurements, whether running test measurements for us or helping us during our actual measurements.

I want to thank our post-doctoral members, Dr. Sara Samuei and Dr. Ruby Phul. Their comments on my studies and observing their working style were very valuable. They helped me a lot with anything that I needed help with. I would also like to thank our past and current members for their useful comments and for being great and supportive labmates.

I would also like to thank my family for their understanding during my studies. They were so supportive, both mentally and financially. Without their guidance, I would not be in this department, let alone doing my Master's studies. I also thank my dear friends, especially Arda, who always stuck with me.

TABLE OF CONTENTS

CHAPTER 1 1

1.0 INTRODUCTION 1

1.1 Renewable Energy Sources 1

1.2 Photocatalytic Water Splitting 1

1.3 Light Absorbing Systems 3

1.3.1 Electron Transition Processes 4

1.3.2 Organometallic Photosensitizers 6

1.4 Quenching Processes 15

1.4.1 Quenching According to Quencher-Sensitizer Positioning 15

1.4.2 Energy Transfer Quenching 16

1.4.3 Electron Transfer Quenching 16

1.4.4 Photosensitizer-Catalyst Dyads 19

1.5 Prussian Blue Analogues (PBAs) 22

1.5.1 Catalytic Relevance of Prussian Blue Analogues (PBAs) 24

1.6 Objective of the Thesis 24

CHAPTER 2 26

2 Experimental 26

2.1 Chemicals and Reagents 26

2.2 Synthesis of Fe1 and Fe2 26

2.3 Synthesis of Cobalt and Zinc Precursors 27

2.4 Synthesis of FeM1 Dyads (M = Co, Zn) 27

2.5 Synthesis of FeM2 Dyads (M = Co, Zn) 28

2.6 Synthesis of CoFe PBA 29

2.7 Instrumentation 29

2.7.1 UV-Visible Spectroscopy 29

2.7.2 Attenuated Total Reflectance- Fourier Transform Infrared Spectroscopy (ATR-FTIR) 29

2.7.3 CHNS Elemental Analysis 29

2.7.4 Differential Pulse Voltametry (DPV) 29

2.7.5 X-Ray Photoelectron Spectroscopy (XPS) 30

2.7.6 X-Ray Absorption Spectroscopy (XAS) 30

2.7.7 Water Oxidation Photocatalysis 30

2.7.8 Turnover Number (TON) Calculation 31

2.7.9 Ultrafast-Transient Absorption Spectroscopy 31

CHAPTER 3 32

3.1 Introduction 32
3.2 Results and Discussions 33
3.2.1 Synthesis 33
3.2.2 Characterization 33
3.2.3 Photocatalytic Studies 48
3.2.4 Ultrafast-Transient Absorption Spectroscopy Studies 51
CHAPTER 4 59
4.0 CONCLUSIONS 59
4.1 Summary 59
4.2 Remarks 61
CHAPTER 5 62
5.0 BIBLIOGRAPHY 62

LIST OF FIGURES

Figure 1.1. A diagram showing H_2/O_2 production and consumption by water. 2

Figure 1.2. Diagram depicting a water oxidation catalyst and a photosensitizer mixed in water. 3

Figure 1.3. MO diagram of LC, MC (blue for centered transitions), LMCT, MLCT, MMCT, and LLCT (red for charge transfer transitions) processes. 5

Figure 1.4. Several reported Fe(II) polypyridyl complexes. Reprinted from [1] under Creative Commons, ACS. 8

Figure 1.5. All possible spin configurations with the lowest energy of a d_6 complex. 8

Figure 1.6. Jablonski Energy Diagram depicting energies of MLCT and MC states upon decreased ligand field strength. 10

Figure 1.7. Jablonski Energy Diagram depicting increased reorganization energy upon ^{5}MC stabilization. 11

Figure 1.8. Several reported Fe(II) NHC complexes. Reprinted from [1] under Creative Commons, ACS. 14

Figure 1.9. Electron transfer quenching according to thermodynamic and light-excited species of Fe(II) complexes. 17

Figure 1.10. Electron transfer quenching through MLCT and ^{5}MC states in Fe(II) complexes. 18

Figure 1.11. Electron transfer quenching upon MLCT excitation with $Ru(II)(bpy)_3^{2+}$. 19

Figure 1.12. WOC initiated by photosensitizer being quenched by the catalyst. 20

Figure 1.13. WOC initiated by photosensitizer being quenched by the sacrificial reagent. 21

Figure 1.14. Crystal Structure of a PBA with a molecular formula of $M_x[M'(CN)_6]_y$. Reused with permission from Ref. [1]. 23

Figure 1.15. A schematic representation of the Co catalyst bridged to the Fe(II) cyanopolypyridyl. 25

Figure 3.1. Scheme of **Fe** photosensitizers, **FeZn** networks with MLCT states, and **FeCo** networks with coupled MLCT-MMCT states. 32

Figure 3.2. (a) UV-Vis spectra of **Fe1**, **FeCo1,** and **FeZn1** between 325-700 nm. (b) UV-Vis spectra of **Fe2**, **FeCo2**, and **FeZn2** between 325-700 nm. 34

Figure 3.3. FTIR spectra of (a) **Fe1**, **FeCo1**, and **FeZn1** and (b) **Fe2**, **FeCo2,** and **FeZn2** in the 400-4000cm^{-1} region. 35

Figure 3.4. ν(CN) stretching of (a)**Fe1**, **FeCo1,** and **FeZn1**(b) **Fe2**, **FeCo2,** and **FeZn2** in the 1950-2200cm^{-1} region. 36

Figure 3.5. N 1s XP spectra of **FeCo1**, **FeCo2,** and CoFe PBA. 37

Figure 3.6. Fe 2p XP spectra of **FeCo1**, **FeCo2,** and CoFe PBA. 38

Figure 3.7. Co 2p XP spectra of **FeCo1**, **FeCo2,** and CoFe PBA. 39

Figure 3.8. N 1s XP spectra of **FeZn1** and **FeZn2**. 41

Figure 3.9. Fe 2p XP spectra of **FeZn1** and **FeZn2**. 42

Figure 3.10. Zn 2p XP spectra of **FeZn1** and **FeZn2**. 43

Figure 3.11. (a) Fe L3-Edge XA spectra of **Fe1**, **FeCo1,** and **FeZn1**. (b) Fe L3-Edge XA spectra of **Fe2**, **FeCo2,** and **FeZn2**. 44

Figure 3.12. (a) Fe L3-Edge XA spectra of **Fe1**, **FeCo1,** and **FeZn1**. (b) Fe L3-Edge XA spectra of **Fe2**, **FeCo2,** and **FeZn2**. 45

Figure 3.13. Co L3-Edge XA spectra of $K_3Co(CN)_6$ and $Co(NO_3)_2$. 46

Figure 3.14. Co L3-Edge XA spectra of $Co(bpy)Cl_2$, $Co(bpy)_2Cl_2$, **FeCo1,** and **FeCo2**. 47

Figure 3.15. DPV experiments with **Fe1**, **Fe2**, and **FeCo1** in 0.1 M TBAP in MeOH. 48

Figure 3.16. Photocatalytic water oxidation experiments with **Fe1, Fe2, FeCo1, FeCo2, FeZn1**, and **FeZn2**. 49

Figure 3.17. Photocatalytic water oxidation experiments with **FeCo1**, **Fe1**/CoFe PB, and **FeZn1**/CoFe PB. 50

Figure 3.18. Photocatalytic water oxidation experiments with **FeCo1**, **Fe1**/CoFe PB, and **FeZn1**/CoFe PB. 51

Figure 3.19. (a) TA spectrum of **Fe1** pumped at 570 nm in methanol. (b) TA spectrum of **FeCo1** pumped at 570 nm in methanol. (c) TA spectrum of **FeZn1** pumped at 570 nm in methanol. (d) TA kinetics of **Fe1**, **FeCo1,** and **FeZn1** pumped at 570 nm and probed at 540 nm in methanol. (e) TA spectrum of **FeCo1** pumped at 370 nm in methanol. (f) TA kinetics of **FeCo1** pumped at 370 and 570 nm and probed at 540 nm in methanol. 52

Figure 3.20. Fitting of TA spectra of **Fe1**, **FeCo1,** and **FeZn1** pumped at 570 nm in methanol. 54

Figure 3.21. (a) TA spectrum of **Fe2** pumped at 570 nm in methanol. (b) TA kinetics of **Fe2** pumped at 570 nm and probed at 540 and 650 nm in methanol. (c) TA spectrum of **FeCo2** pumped at 570 nm in methanol. (d) TA kinetics of **FeCo2** and **FeZn2** pumped at 570 nm and probed at 540 nm in methanol. (e) TA spectrum of **Fe2** pumped at 370 nm in methanol. (f) TA kinetics of **Fe2** pumped at 370 nm and probed at 540 and 650 nm in methanol. (g) TA spectrum of **FeCo2** pumped at 370 nm in methanol. (h) TA kinetics of **FeCo2** pumped at 370 and 570 nm and probed at 540 nm in methanol. 56

Figure 3.22. Fitting of TA spectra of **Fe2**, **FeCo2,** and **FeZn2** pumped at 570 nm in methanol. 58

Figure 3.23. Jablonski diagram of **Fe1** and **Fe2** based systems. 59

Figure 4.1. Schematic diagram of MLCT excitation of Fe(II) cyanopolypyridyls followed by decay to MMCT and MC states. 60

CHAPTER 1

1.0 INTRODUCTION

1.1 Renewable Energy Sources

As the demand for alternative energy sources has become increasingly evident, research into renewable energy technologies has expanded. These investigations encompass methods utilizing wind, nuclear, thermal, and solar energy. Among these, solar energy conversion is of particular interest due to its potential for sustainable energy storage and utilization.[2–5] Solar energy can be transformed into electrical energy via photovoltaic cells[6] or into thermal energy through solar thermal panels. Additionally, light-driven processes like photoelectrocatalysis are employed to enhance the electrochemical synthesis of specific chemicals.[2–4,7–13] Among various solar energy conversion strategies, the transformation of solar energy into chemical energy is considered one of the most sustainable storage approaches. Unlike direct electrical or thermal methods, chemical energy storage permits the production of chemical fuels and compounds, including inorganic gases such as hydrogen and methane, as well as organic molecules. These processes typically involve water splitting photocatalysis for hydrogen production or photoredox catalysis for organic chemical synthesis using light. Based on the thermodynamic considerations, light-induced conversion processes can be classified into reforming and other catalytic pathways, depending on the free energy change of the system.

1.2 Photocatalytic Water Splitting

Water constitutes a significant proportion of Earth's surface, making it a primary resource for renewable fuel production. Unlike organic-based photoredox catalysis—which operates via both energy and electron transfer mechanisms—water splitting exclusively involves electron transfer processes because it is governed by two half-reactions: reduction and oxidation.[2,4,7–9,14,15] In the reduction half-reaction, water molecules are converted into hydrogen gas, requiring the transfer of two electrons

per molecule[3,7–10,15–20]; the oxidation half-reaction produces oxygen and involves a similar number of electrons (Figure 1.1).[7,14,19–21] Since the number of electrons involved is doubled in oxygen evolution, the reaction timescales differ: hydrogen generation typically occurs within a 10^{-12}-10^{-9} seconds, whereas oxygen evolution requires a longer duration to complete, making oxygen production the rate-limiting step of water splitting.[4,7] When using sacrificial reagents capable of acting as either reductants or oxidants, water splitting photocatalysis can selectively produce hydrogen or oxygen alone. This simplifies the study of individual half-reactions.

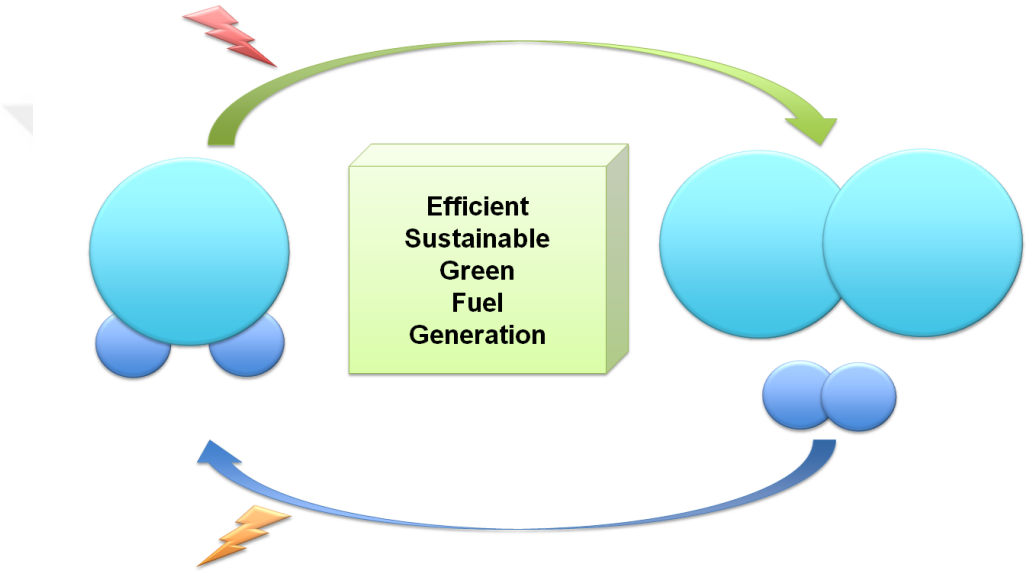

Figure 1.1. A diagram showing H_2/O_2 production and consumption by water.

A common approach for substituting the oxygen evolution reaction involves allyl amines, such as triethylamine, and hydroxy allyl amines, like triethanolamine, which possess relatively low oxidation potentials and can interact with various catalysts.[2,4] Evidence suggests that hydrogen produced via this route may include hydrogen atoms originating from these allyl amines. Other sacrificial reagents include silver nitrate and ascorbic acid. If the goal is to replace hydrogen production, persulfate salts can be used as oxidants (Figure 1.2).[14,20,21] It is important to note that the byproducts resulting from these sacrificial reagents are generally of limited interest, placing such experiments under idealized conditions. Recently, triethylamine has been replaced by benzyl alcohols, which upon oxidation yield benzaldehydes or ketones—valuable chemicals in their own right.[22–25]

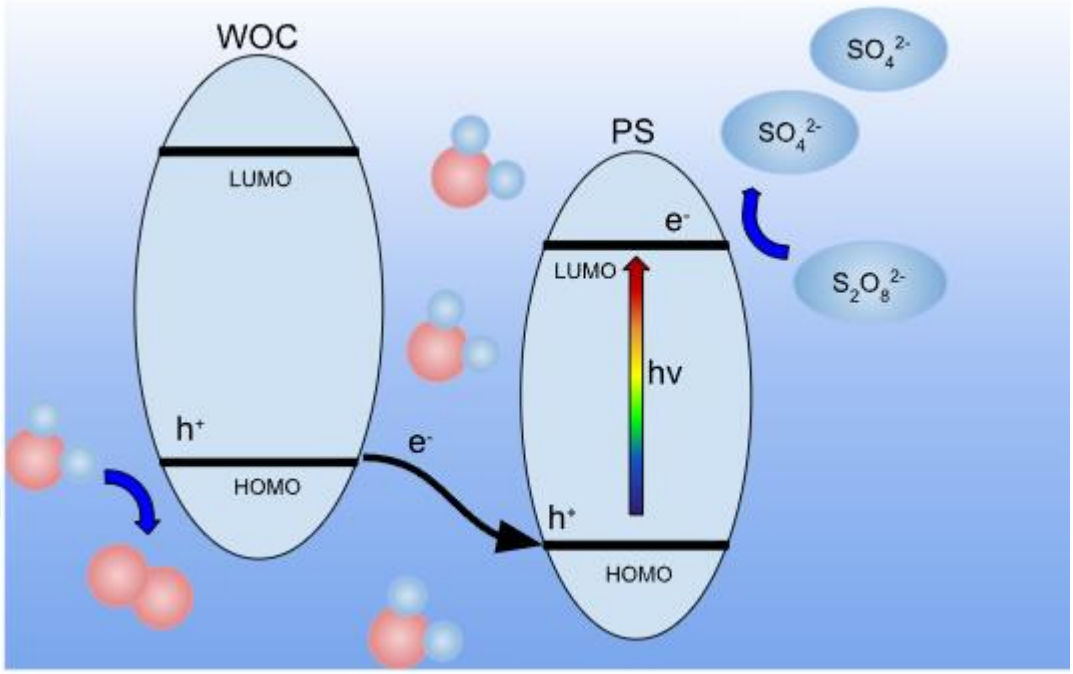

Figure 1.2. Diagram depicting a water oxidation catalyst and a photosensitizer mixed in water.

1.3 Light Absorbing Systems

Efficient solar light harvesting remains a significant challenge in both academic research and industrial applications. Achieving high efficiency in this process requires a thorough understanding of the photophysical behavior of the light-absorbing materials.[5,8,15,19,20,26] Light absorption can occur via two main classes of systems: bulk semiconductors and molecular photosensitizers, such as organometallic or organic compounds.

In semiconductors, light absorption leads to the generation of electron-hole pairs, with charge separation occurring across the extended crystal lattice.[2,7,8,15] Due to the large size and periodic structure of these systems, the discrete molecular orbitals (HOMO and LUMO) form continuous energy bands, namely the valence band and conduction band. Electrons in such systems are typically delocalized.

Conversely, in molecular systems, photoexcitation tends to be more localized. Understanding the dynamics of electron-hole separation and their subsequent recombination is crucial.[11,12,22,23,27] In semiconductors, charge separation often involves spatial migration of electrons and holes to different regions of the material (e.g., electron to the shell, hole to the core). In contrast, molecular systems often rely on charge-transfer mechanisms where the electron and hole are spatially separated within the same molecule. The electronic states are more localized than those of semiconductors.

1.3.1 Electron Transition Processes

Photosensitizers exhibit two primary types of electronic transitions: localized (centered) and charge-transfer transitions.[5,11–13,27–30] Centered transitions include Metal-Centered (MC), also referred to as Ligand-Field (LF) transitions, which are typical for transition metal complexes, and Ligand-Centered (LC), also known as Intra-Ligand (IL) transitions, common in organic chromophores. Charge-transfer transitions are categorized into four types: Metal-to-Metal Charge Transfer (MMCT) or Intervalence Charge Transfer (IVCT), Metal-to-Ligand Charge Transfer (MLCT), Ligand-to-Metal Charge Transfer (LMCT), and Ligand-to-Ligand Charge Transfer (LLCT), also termed Interligand Charge Transfer (ILCT) (Figure 1.3).

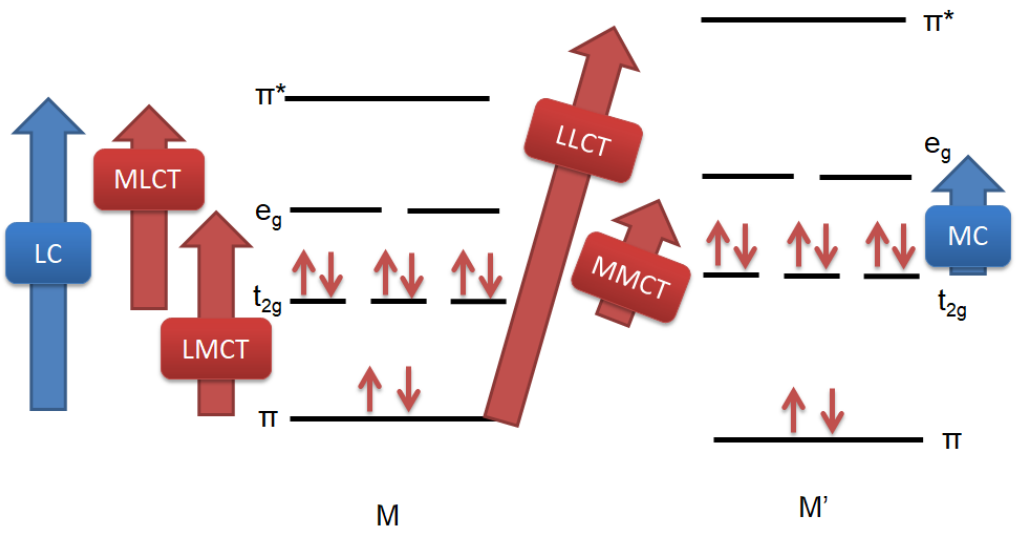

Figure 1.3. MO diagram of LC, MC (blue for centered transitions), LMCT, MLCT, MMCT, and LLCT (red for charge transfer transitions) processes.

Understanding the nature of electronic transitions is essential in the context of light absorption and photochemistry. In organic ligands, the highest occupied molecular orbitals (HOMOs) are typically composed of π orbitals. As a result, the most common transitions in such systems are spin-allowed singlet-to-singlet ($S = 0 \rightarrow S = 0$) $\pi \rightarrow \pi^*$ excitations.[10,16,18]

Most electronic transitions are spin-conserving, as transitions that involve a change in spin quantum number ($\Delta S \neq 0$) are spin-forbidden. Although spin-forbidden transitions can occur, they are quantum mechanically less probable and exhibit significantly lower intensity. For instance, spin-allowed $\pi \rightarrow \pi^*$ transitions generally have high molar extinction coefficients ($\varepsilon > 1000\ M^{-1}\ cm^{-1}$), whereas spin-forbidden transitions display moderate values ($\varepsilon \approx 10–100\ M^{-1}\ cm^{-1}$).[10,16,17]

Additionally, allowed transitions typically involve a change in orbital angular momentum ($\Delta l = \pm 1$), which is governed by selection rules such as the Laporte rule. Because d–d transitions involve excitation between orbitals of the same parity (no change in orbital angular momentum, i.e., $\Delta l = 0$), they are Laporte-forbidden. These transitions thus exhibit low absorption intensities, similar to those of spin-forbidden transitions. When both spin and Laporte selection rules are violated (as in spin-forbidden d–d transitions), the resulting absorptivity is even lower ($\varepsilon \approx 1–100\ M^{-1}\ cm^{-1}$).[31] Despite their low transition probabilities, such formally "forbidden" states can still be accessed under specific conditions and have proven valuable in applications like photoredox catalysis, where long-lived excited states are often advantageous. As previously discussed, d–d transitions are intrinsically forbidden due to selection rules related to spin and orbital angular momentum. This limitation necessitates alternative strategies for efficient light absorption using metal centers. One such approach is through organometallic compounds, where the HOMO and LUMO are often of distinct orbital character (e.g., metal-based vs. ligand-based), enabling charge-transfer (CT) transitions, which are generally more allowed than d–d transitions.[12,13,22]

The probability and efficiency of electronic transitions also depend significantly on the solvent polarity. Localized transitions are typically favored in non-polar solvents, whereas charge-transfer states are stabilized in polar solvents.[5,13,22–24] As a result, organometallic photosensitizers—particularly those bearing pyridine-like ligands—exhibit strong charge-transfer absorption bands (with molar absorptivities in the range of 1,000–10,000 M^{-1} cm^{-1}) when dissolved in polar solvents such as water or methanol.

The nature of the HOMO and LUMO, including whether they are metal- or ligand-centered, their energy levels, the presence of singly unoccupied molecular orbitals (SUMOs), and the oxidation state of the metal, all influence whether metal-to-ligand (MLCT) or ligand-to-metal charge-transfer (LMCT) transitions occur.[29,32,33] Additionally, the redox potentials of the metal centers and ligands contribute to the energetic feasibility of such transitions. While metal-to-metal charge transfer (MMCT) can also occur—often at comparable or even lower photon energies—its role in photocatalytic quenching remains underexplored relative to LMCT and MLCT processes, which are widely utilized in photocatalytic applications.

1.3.2 Organometallic Photosensitizers

The scenario differs significantly in transition metal complexes. Here, the HOMOs often consist of metal-centered d orbitals, except in d^0 systems or metallorganic compounds with strongly conjugated π-systems.[5,12,13,24,32,34–37] These metal complexes can exhibit a range of spin multiplicities in their ground states, varying from singlet (S = 0) to sextet (S = 5/2), due to the unpaired d-electrons. The spin multiplicity, defined by the term 2S + 1, determines the spin state of the system.

Among the most commonly employed organometallic systems are d^3 and d^6 complexes, such as Cr(III), Ru(II), Ir(III), and Re(I) complexes.[5,12,13,24,32,34–37] d^3 systems often display LMCT transitions. The octahedral Cr(III) ion has a half-filled t_{2g} orbital set, which lies low in energy due to the high positive charge, resulting in a small energy gap between ligand π orbitals and the metal t_2g orbitals. d^6 systems frequently undergo MLCT transitions. These metals have fully filled t_{2g} orbitals,

which are relatively higher in energy and can efficiently interact with ligand-based π* orbitals, promoting strong MLCT behavior.

It is essential to first examine the photophysical behavior of Ru(II) polypyridyl complexes, since their photophysics is well-established in light-driven catalysis.[22,23] Upon photoexcitation, these complexes typically undergo a singlet metal-to-ligand charge transfer (^{1}MLCT) transition. This excited state has a very short lifetime (hundreds of femtoseconds) and rapidly undergoes intersystem crossing (ISC) to form the corresponding triplet MLCT (^{3}MLCT) state.[38–40] This process is facilitated by strong spin–orbit coupling and the small energy gap between the ^{1}MLCT and ^{3}MLCT states.

The ^{3}MLCT state is relatively long-lived (lifetime of nanoseconds) and often luminescent.[41–43] Excited species emitlight as they decay back to the ground state. Importantly, the energy loss during the ^{1}MLCT → ^{3}MLCT relaxation is minimal, making these systems highly suitable for photocatalytic applications, where long-lived excited states are beneficial.

However, a major limitation of these systems lies in their environmental and economic sustainability. The decomposition of such complexes can release toxic, water-soluble heavy metals, such Cr, Ru and Ir, and many of the effective d^6 metals mentioned are rare and expensive, rendering large-scale catalytic applications impractical.

1.3.2.1 Polypyridyl Fe(II) Complexes

Attempts have been made to replace these rare metals with more abundant alternatives, such as Fe and Co, aiming to substitute Ru and Ir, respectively.[30,31,37] However, several challenges remain. Co-based systems typically only exhibit forbidden metal-centered (MC) transitions in the visible spectrum, though there is growing evidence in the literature supporting their potential in certain photoredox catalytic applications.[44] Fe(II) complexes can exhibit MLCT transitions similar to Ru(II), but their performance is hindered by unfavorable photophysical properties, such as short excited-state lifetimes and rapid non-radiative decay (Figure 1.4).[45–47]

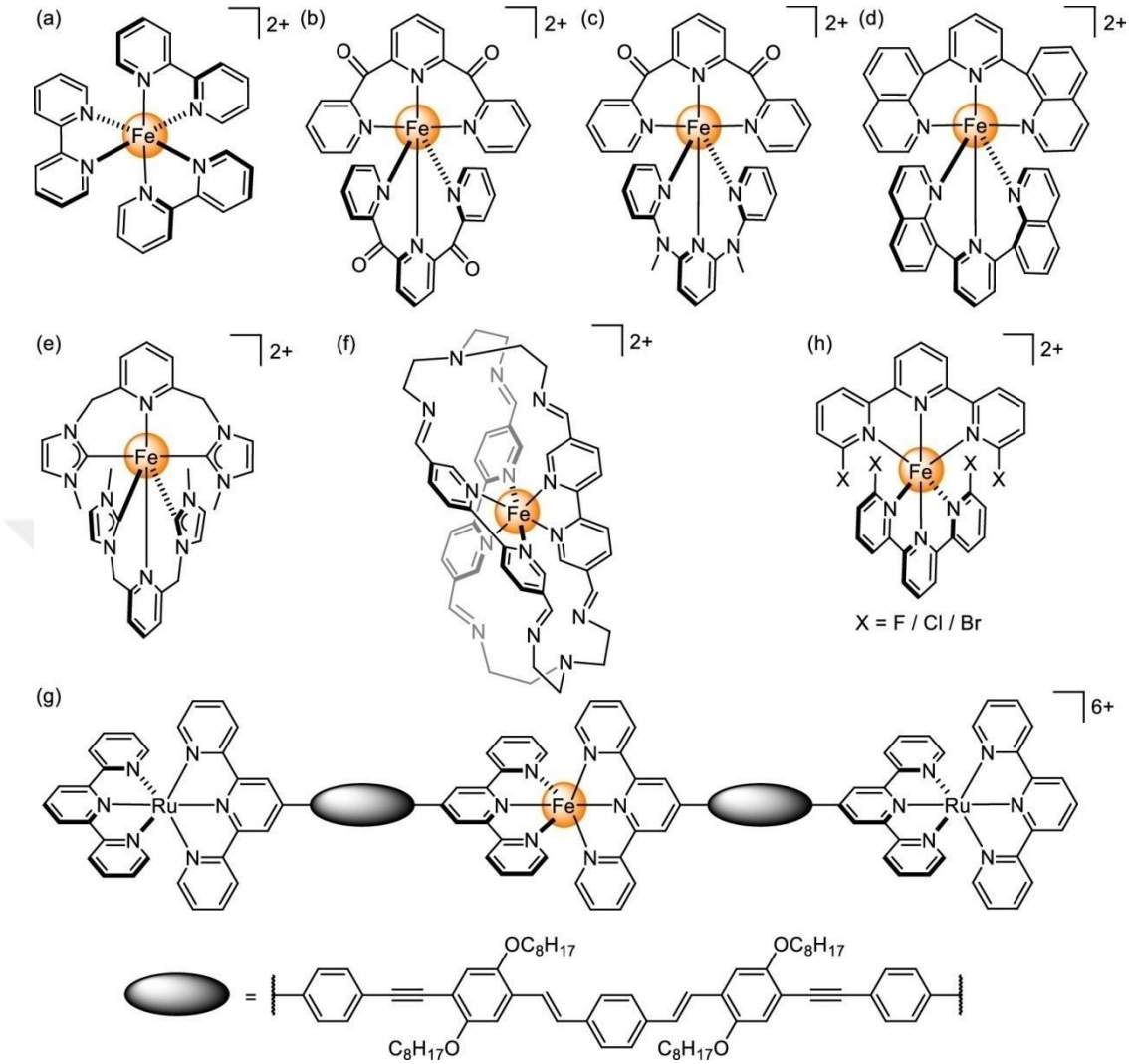

Figure 1.4. Several reported Fe(II) polypyridyl complexes. Reprinted from [1] under Creative Commons, ACS.

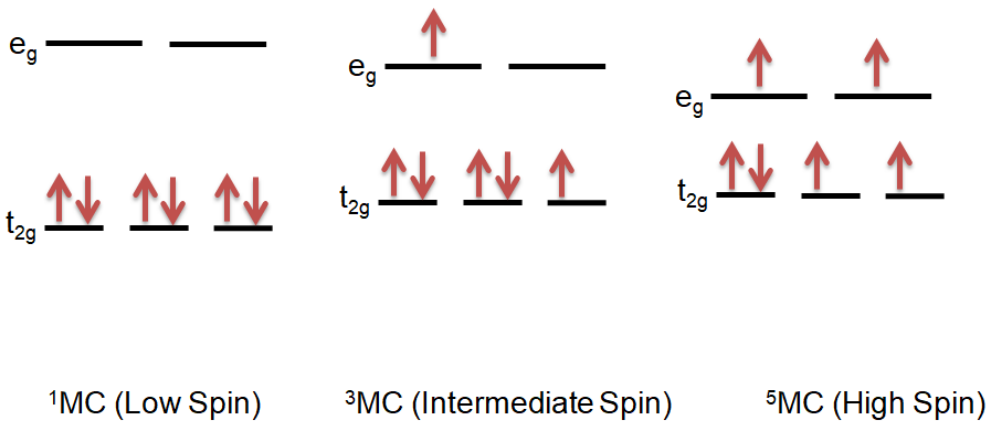

Figure 1.5. All possible spin configurations with the lowest energy of a d_6 complex.

In contrast to Ru(II) polypyridyl complexes, Fe(II) polypyridyl ones exhibit markedly different behavior due to intrinsic electronic and structural factors. Being a 3d transition metal, Fe(II) lacks the additional radial node found in 4d orbitals (as in Ru), leading to greater spatial overlap between Fe 3d and 4s orbitals.[30] This competition weakens metal–ligand (Fe–N) bonding, an effect referred to as the primogenic effect. As a result, the ligand field strength (octahedral field splitting, Δ_o) is reduced. This weaker ligand field leads to a critical consequence: the triplet metal-centered (^{3}MC) state becomes energetically comparable to or even lower than the ^{3}MLCT state(Figure 1.5). Due to differences in orbital characteristics, there is strong spin–orbit coupling between ^{3}MLCT and ^{3}MC states, enabling efficient internal conversion. Consequently, the ^{3}MLCT state rapidly decays into the ^{3}MC state. The decay of ^{3}MC to the ground state is a non-radiative process with a very short lifetime (~10 picoseconds), accompanied by moderate energy loss.[5,30,32,37] Since it is non-luminescent, this transition is not observable via photoluminescence spectroscopy. Instead, the ^{3}MC state can be detected through excited-state absorption features, such as triplet–triplet absorption around 600 nm. If the ligand field strength decreases further, a quintet metal-centered (^{5}MC) state can drop below the ^{3}MC state in energy. The relaxation from ^{5}MC to the ground state is also non-radiative but occurs on a longer timescale (~100 picoseconds) and with significant energy loss. This prolonged lifetime arises from the high spin-forbidden nature of the transition ($\Delta S = 2$, $\Delta s = 1$) and the substantial nuclear distortion involved.

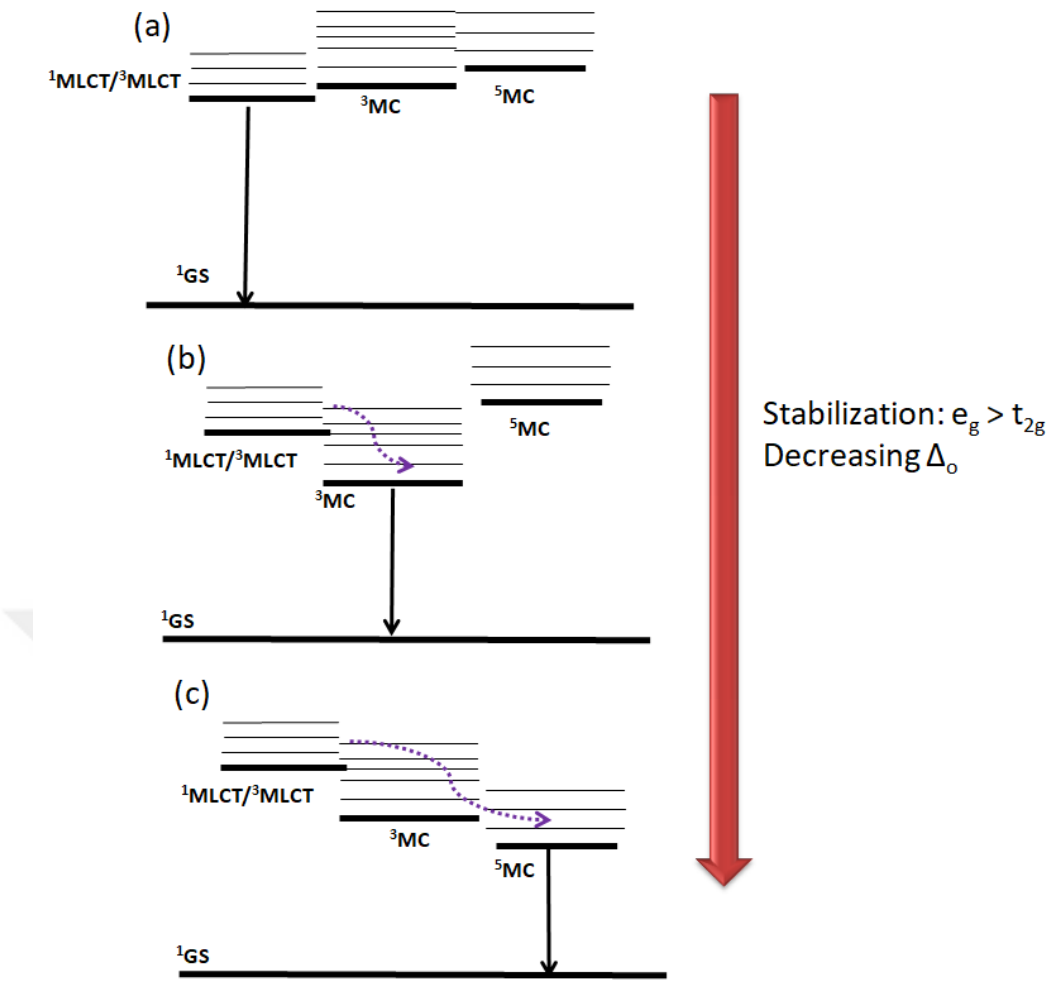

Figure 1.6. Jablonski Energy Diagram depicting energies of MLCT and MC states upon decreased ligand field strength.

This distortion is caused by the occupation of two electrons in antibonding e_g orbitals in the ^{5}MC state, whereas the ground state lacks such destabilizing occupancy(Figure 1.6).[48,49] If the ligand field weakens further such that the ^{5}MC becomes lower in energy than the initial ^{1}MLCT state, the system must undergo even greater reorganization energy for nuclear distortion during relaxation (Figure 1.7). This results in both an increased excited-state lifetime and a greater energy loss due to relaxation processes.

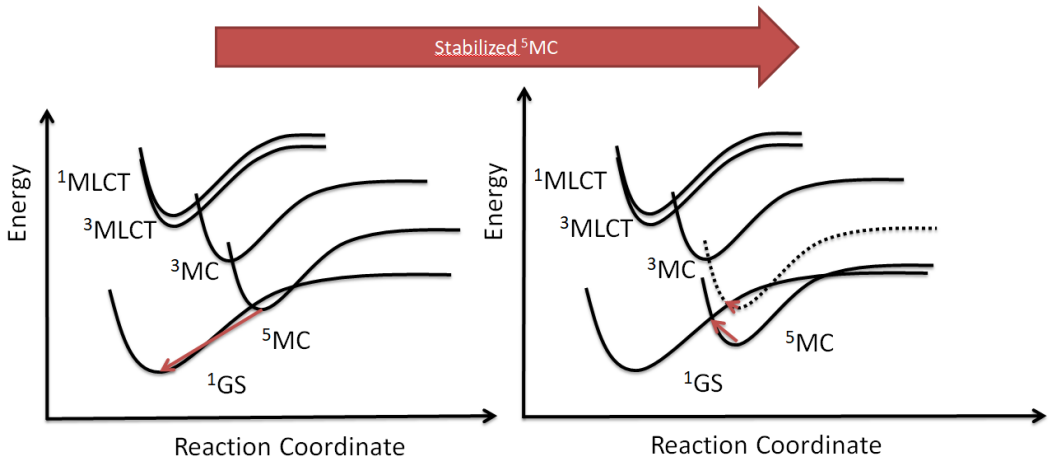

Figure 1.7. Jablonski Energy Diagram depicting increased reorganization energy upon ^{5}MC stabilization.

In summary, the poor photophysical performance of Fe(II) complexes compared to Ru(II) arises from weaker Fe–ligand bonding (primogenic effect), reduced ligand field strength, low-lying MC states that deactivate MLCT states, fast and non-luminescent decay channels, which cannot be examined by photoluminescence spectroscopy, high energy loss via spin-forbidden and vibrationally distorted transitions. These factors pose substantial limitations for photocatalytic applications of Fe(II) systems, despite their earth abundance and favorable redox properties. In principle, the effects of ligand field strength can be investigated by analyzing the energy positions of the forbidden ^{3}MC and ^{5}MC transitions. However, these transitions are difficult to observe spectroscopically due to their intrinsically low absorptivity. The ^{5}MC state, in particular, exhibits very weak absorption features in the near-infrared (NIR) region, often below the detection limits of conventional spectroscopic techniques.[50–54] Similarly, the ^{3}MC state, while somewhat more detectable, typically has an extinction coefficient of only ~50-100 M^{-1} cm^{-1}, making it challenging to distinguish, especially when it overlaps with the much more intense MLCT absorption band.

As a result, direct observation of MC states in transient absorption spectroscopy is often hindered, and the data obtained can be difficult to interpret unambiguously. This limits the ability to accurately assess ligand field effects through conventional time-resolved spectroscopic methods, thereby complicating the study of excited-state

dynamics in transition metal complexes, particularly those involving early 3d metals like iron.

Although Fe(II) polypyridyl complexes possess redox potentials ($Fe^{2+/3+}$) that are comparable to Ru(II) analogs, and often show similar ground-state electrochemical behavior, their excited-state photophysics diverge significantly. This divergence is primarily due to the primogenic effect, which leads to weaker Fe–ligand interactions, thereby reducing the octahedral ligand field splitting (Δ_o). As a result, the ^{5}MC (quintet metal-centered) state is significantly stabilized and becomes the dominant excited-state species, observable in transient absorption spectroscopy, in contrast to the desirable MLCT (metal-to-ligand charge transfer) state typically observed in Ru(II) complexes.

1.3.2.2 Cyanopolypyridyl Fe(II) Complexes

To reproduce Ru-like photophysics in Fe-based systems, it is essential to increase the ligand field strength. One approach has been the substitution of bipyridine ligands with cyanide (CN^-), a well-known strong-field ligand.[38,48,49,55–58] In bicyano-substituted Fe(II) complexes, although some destabilization of the ^{5}MC state is observed, it remains the lowest-energy excited state. When a third cyanide is introduced, ^{3}MC (triplet metal-centered) features become apparent, indicating that the ^{3}MC state is now more stable than ^{5}MC. Adding a fourth cyanide results in minimal additional effect—the ^{3}MC remains the lowest excited state.

Interestingly, solvent effects play a critical role in the energetic ordering of excited states. When the solvent is changed from protic solvents like water or methanol to aprotic solvents such as DMSO, MLCT features begin to emerge. This behavior is attributed to acid-base interactions between the cyanide ligand and solvent molecules. In aqueous or methanolic media, hydrogen bonding occurs between the solvent hydrogen and cyanide nitrogen, resulting in electron donation from water's oxygen lone pairs into the π^* orbitals of the cyanide. This increases π^* electron density, enhancing π^*–t_{2g} interactions, which in turn stabilize both t_{2g} and e_g orbitals, but with a greater effect on t_{2g}.

As a consequence, the MLCT state becomes destabilized in water/methanol due to the stronger stabilization of the t_{2g} orbitals. In DMSO, however, no such hydrogen bonding occurs, and thus the t_{2g} orbital is relatively less stabilized, allowing the ^{3}MLCT state to become lower in energy than the ^{3}MC state. This makes tetracyanoferrate complexes viable photosensitizers in aprotic solvents like DMSO or acetone, providing a promising Fe-based alternative to Ru(II) polypyridyl complexes.

Nevertheless, a significant challenge remains for polar protic solvents such as water and methanol, which are essential for many sustainable photocatalytic applications. Two main strategies have been explored to address this, which are to replace polypyridyl ligands with even stronger-field ligands than cyanide or to introduce a fifth cyanide ligand, though this approach has critical drawbacks.

1.3.2.3 Other Fe(II) Complexes

The latter approach often necessitates the exclusion of bidentate ligands and leads to mono-dentate ligand coordination, which is susceptible to ligand loss upon photoexcitation.[59] Because photoexcitation typically involves population of antibonding orbitals, significant nuclear distortion occurs, potentially destabilizing the metal–ligand framework and resulting in photodecomposition.

Consequently, attention has turned to the first approach. Recent studies have shown that N-heterocyclic carbenes (NHCs), with their strong σ-donating, radical-like carbon lone pair, are even stronger field ligands than cyanide.[60–74] Importantly, NHC ligands destabilize the ^{5}MC state more effectively than CN^-, promoting long-lived MLCT character even in aqueous environments. Furthermore, NHCs offer modularity and synthetic flexibility, with numerous ligand frameworks already reported in the literature, allowing for fine-tuning of photophysical properties (Figure 1.8).[60,61,63,69]

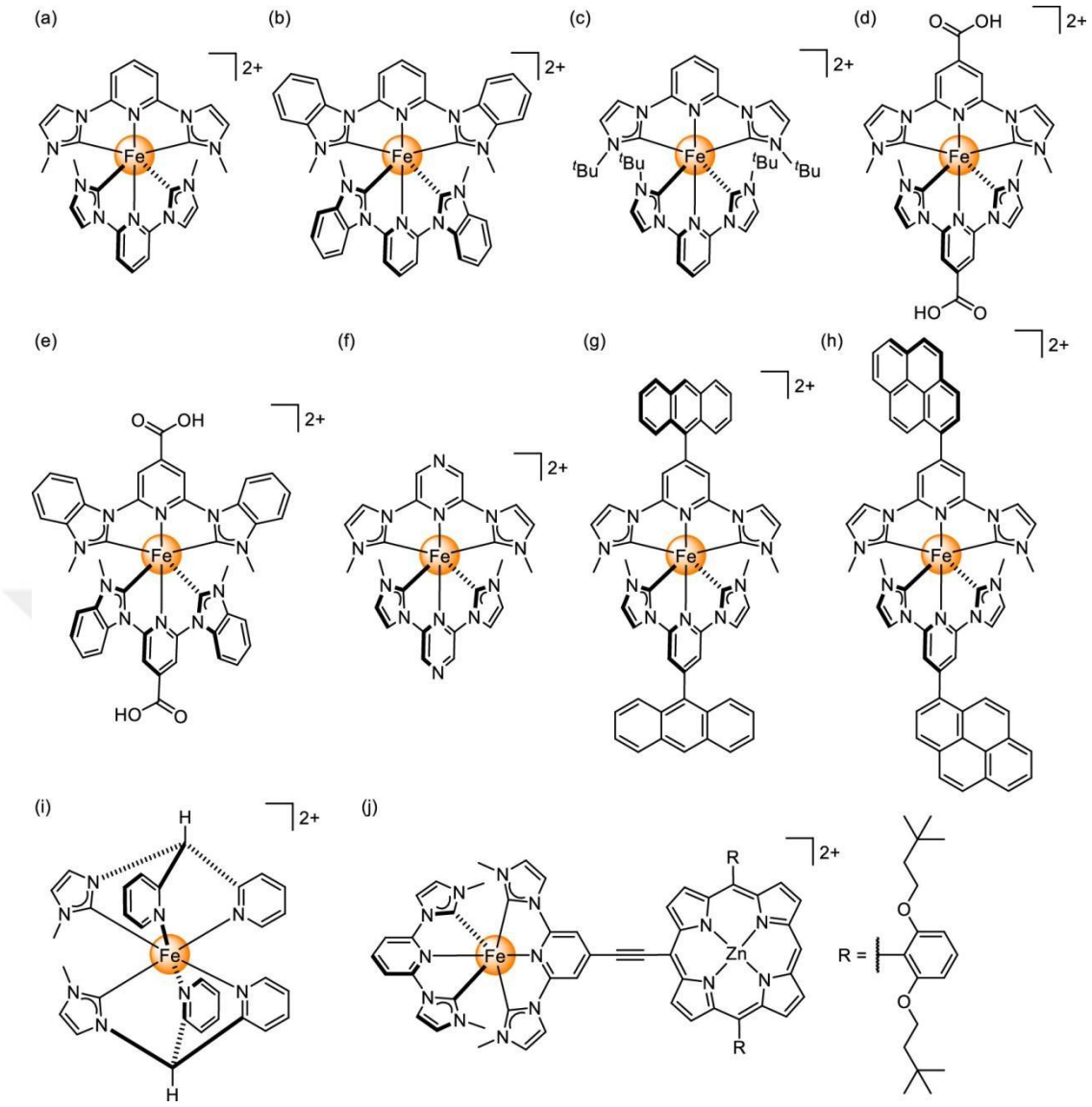

Figure 1.8. Several Fe(II) NHC complexes. Reprinted from [1] under Creative Commons, ACS.

The design flexibility of N-heterocyclic carbenes (NHCs) arises from their structural composition—aromatic heterocyclic rings—which can be easily functionalized and integrated into larger ligand systems, such as pyridyl or imidazole frameworks. This tunability stands in contrast to cyanide ligands, which, despite their strong-field character, are chemically less adaptable for modular ligand design.

However, the synthetic accessibility of NHC-based iron complexes remains a significant challenge. Industrial-scale production of carbene ligands is limited, and their coordination to Fe requires stringent synthetic conditions. The commonly used

base, potassium tert-butoxide (tBuOK), is highly caustic and pyrophoric, necessitating strict air- and moisture-free conditions, often under liquid nitrogen temperatures. These technical barriers have driven researchers to explore alternative systems with improved synthetic practicality and photophysical performance.

Recent work has focused on novel cyanometallate derivatives and Fe(III)-carbene complexes. For instance, tetracyano-bipyrimidine complexes, derived from bipyridyl-like ligands, have demonstrated MLCT stability even in protic solvents like methanol, as confirmed by Resonant Inelastic X-ray Scattering (RIXS) studies.[57] Furthermore, our group reported that cationic pyrazinium ligands enabled the formation of photostable and MLCT-stable pentacyano-ferrate(II) complexes.[59] However, these systems suffer from relatively short excited-state lifetimes, primarily due to vibrational relaxation caused by hydrogen bonding between cyanide and protic solvents.

Other advances include strained Fe(II) complexes, which have been shown to stabilize the ^{3}MC state long enough to reach nanosecond lifetimes, a promising development for Fe-based photosensitizers.[75]

1.4 Quenching Processes

While organometallic complexes can participate in both energy and electron transfer processes, redox-based catalysis is typically more effective when a dedicated catalytic site is involved. As a result, it is common to combine a photosensitizer and a catalyst, which can be arranged in two main ways: physically mixed, as separate but coexisting components, and covalently linked.[76]

1.4.1 Quenching According to Quencher-Sensitizer Positioning

The linkage between the quencher and the sensitizer changes the mechanism of excited-state quenching, which can proceed via two pathways. Dynamic quenching occurs when the photosensitizer is first excited by light and then collides with the quencher (the catalytic site) in solution. This process is diffusion-limited and affected by concentration, viscosity, and temperature.

Static quenching happens when the photosensitizer–quencher complex pre-forms before light absorption. Upon excitation, electron or energy transfer occurs intramolecularly, which is not limited by diffusion and is typically more efficient.Static quenching is often preferred due to its predictability and faster kinetics, especially in applications requiring high catalytic turnover.

1.4.2 Energy Transfer Quenching

Energy transfer occurs via two distinct pathways, as Dexter Energy Transfer and FRET. Dexter Energy Transfer consists of a short-range mechanism that requires orbital overlap between the donor (photosensitizer) and acceptor (quencher). Its effective only at distances less than ~5 Å. It does not require the donor to be luminescent, making it compatible with non-emissive excited states. It involves the exchange of electrons and is sensitive to molecular geometry and electronic coupling. Whereas Förster Resonance Energy Transfer (FRET) is a longer-range mechanism that can operate over 10–100 Å, depending on spectral overlap and orientation. FRET requires the donor to be luminescent, since the transfer is based on dipole–dipole interactions and spectral overlap between donor emission and acceptor absorption. It is often referred to as dispersive energy transfer. While both Dexter and FRET affect the fate of the excited state, they generally do not alter the catalytic outcome, as they do not change the energetic states of the components involved.

1.4.3 Electron Transfer Quenching

In organometallic photosensitizers, the ligands are typically aromatic systems, such as bipyridines or related heterocycles. When these ligands undergo oxidation or reduction, the resulting ligand-centered radicals tend to be highly reactive and unstable, making them unsuitable as primary sites for redox activity in catalytic cycles (Figure 1.9). In contrast, metal-centered redox events—particularly those involving first-row or second-row transition metals—tend to produce more stable and controllable oxidation states, which are better suited for catalytic electron transfer.

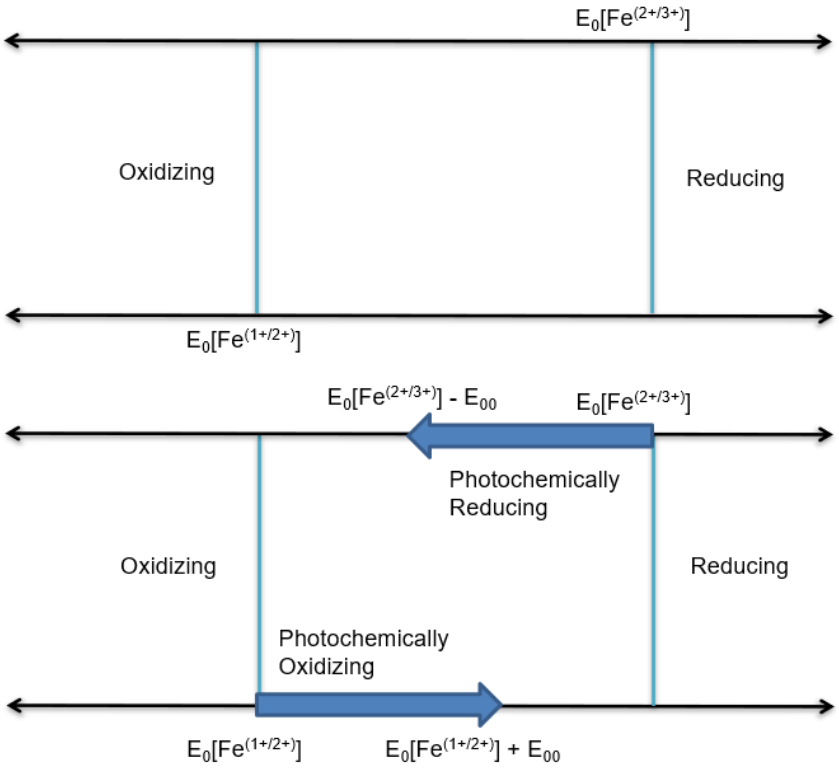

Figure 1.9. Electron transfer quenching according to thermodynamic and light-excited species of Fe(II) complexes.

An important factor in photosensitizer design is the stability of the metal in various oxidation states. For iron, Fe^{2+} and Fe^{3+} are relatively stable and well-characterized, while Fe^{4+} is highly reactive and short-lived, and Fe^{+} is extremely unstable, rarely observed under typical photochemical conditions. Thus, redox processes involving Fe(II) typically cycle between Fe^{2+} and Fe^{3+}, with care taken to avoid accessing higher or lower oxidation states that could result in decomposition or unwanted side reactions.

Initially, Fe(II) polypyridyl complexes with long-lived ^{5}MC (quintet metal-centered) excited states were presumed to engage in catalysis through a metal-to-ligand charge transfer (MLCT) mechanism, analogous to Ru(II) complexes.[77] However, detailed photochemical kinetics studies using transient absorption spectroscopy (TAS) have revealed that catalysis actually proceeds through the ^{5}MC state rather than the MLCT state (Figure 1.10). This finding underscores the need to carefully characterize the identity and reactivity of the true active excited state in iron-based photosensitizers,

as ^{5}MC states can possess sufficient energy and lifetime to drive redox transformations, even in the absence of traditional MLCT behavior.[78]

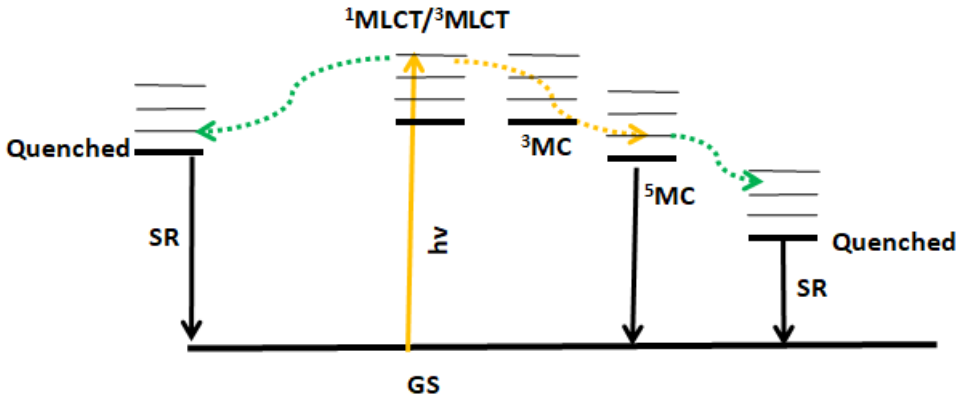

Figure 1.10. Electron transfer quenching through MLCT and ^{5}MC states in Fe(II) complexes.

To fully understand quenching mechanisms in dyad systems, it is important to distinguish between the two main modes of excited-state deactivation: energy transfer and electron (redox) transfer. While both processes can quench the excited state of a photosensitizer, only electron transfer mechanisms are directly involved in catalysis, whereas energy transfer typically affects excited-state lifetimes without contributing to chemical transformation.

1.4.3.1 Electron Transfer Quenching with d^6 Systems

Electron transfer quenching is essential for driving photoredox and water splitting catalysis. There are two main quenching pathways, which are oxidative quenching and reductive quenching. With oxidative quenching, the excited-state photosensitizer donates an electron to the quencher, becoming oxidized. With the latter process, the excited-state photosensitizer accepts an electron, becoming reduced.[12,13,22,23,76,78]

These pathways are central to the photocatalytic cycle, which typically involves three key steps: photoexcitation, where the photosensitizer absorbs a photon, promoting it to an excited state (e.g., MLCT or MC); the first redox step (quenching), where either oxidative or reductive quenching occurs, initiating the catalytic cycle. Finally, the second redox step, where a subsequent redox event restores the ground-state photosensitizer, allowing the cycle to repeat (Figure 1.11).

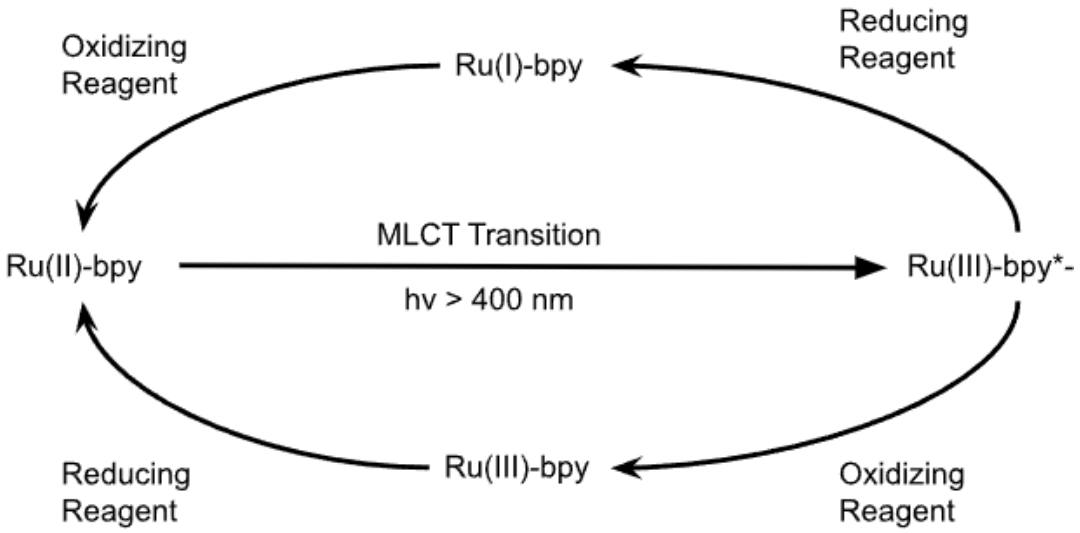

Figure 1.11. Electron transfer quenching upon MLCT excitation with $Ru(II)(bpy)_3^{2+}$.

This framework emphasizes that both quenching and regeneration of the photosensitizer are necessary for sustained catalysis. In dyad systems, where the photosensitizer and catalyst are either physically associated or covalently linked, the nature of quenching (static vs. dynamic) and the specific quenching mechanism (electron or energy transfer) profoundly impact efficiency, kinetics, and mechanism of catalysis.

1.4.4 Photosensitizer-Catalyst Dyads

As most quenching systems consist of two components, photocatalytic dyads, which consist of chemically bonded photosensitizers and quenching catalysts, are commonly used in the literature. In the field of photocatalytic dyads, the majority of molecular systems reported to date rely on rare-earth or precious metal-based photosensitizers, such as Ru(II), Ir(III), or Re(I) complexes.[36,79] These systems are favored due to their favorable photophysical properties, including long-lived MLCT states and predictable redox behavior. However, their reliance on scarce and expensive metals poses sustainability and scalability challenges.

To date, only two molecular dyad systems have been reported in the literature that utilize Fe-based photosensitizers in combination with Co-based catalysts.[35,80] In both cases, the cobalt center was not shown to directly quench the excited-state Fe photosensitizer, leaving the mechanistic details of the electron transfer processes

unclear. This lack of demonstrated Fe-to-Co photoredox quenching indicates that true cooperative dyadic electron transfer remains an unresolved challenge in earth-abundant metal systems.

Moreover, research into dyads for water oxidation catalysis is significantly underdeveloped when compared to systems designed for proton reduction and hydrogen evolution. The two Fe–Co dyads mentioned earlier were also limited to hydrogen evolution reactions (HER), with no comparable molecular systems currently reported for oxygen evolution (OER) based on Fe photosensitizers.

This reveals a critical gap in the literature: while Fe and Co are earth-abundant and attractive for sustainable photocatalysis, integrated dyad systems for overall water splitting, particularly those involving Fe-based photosensitizers in OER, are nearly nonexistent. This highlights an opportunity for future work to develop robust, earth-abundant molecular dyads that operate effectively in both halves of water splitting—a necessary step toward scalable solar fuel generation (Figures 1.11 and 1.12). For photocatalytic water oxidation dyads, there are two paths in which quenching can occur, as shown in Figures 1.11 and 1.12.

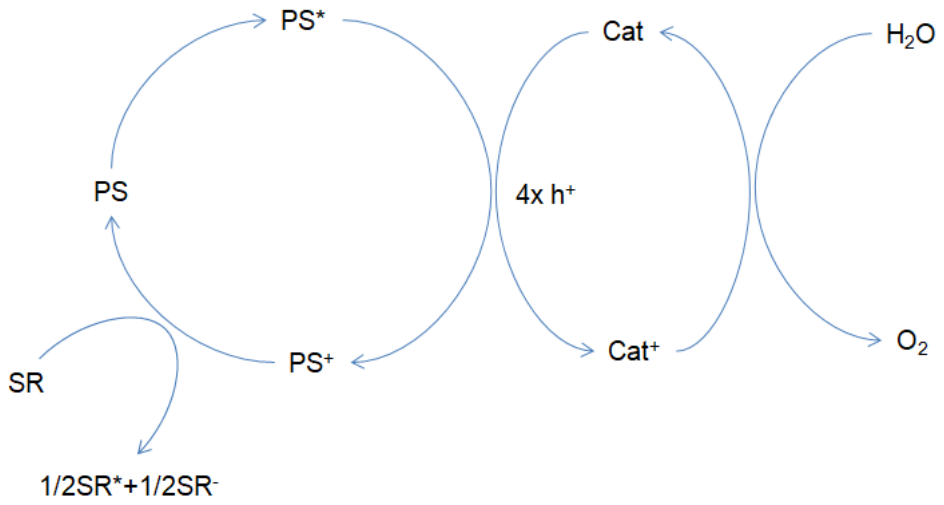

Figure 1.12. WOC initiated by photosensitizer being quenched by the catalyst.

Figure 1.12 illustrates a photocatalytic cycle where the light-excited photosensitizer is first quenched by the catalytic site. This results in several (4 times) oxidations of

the catalyst. It can either change the oxidation state of the catalytic metal or the species of the oxygen (from O^{2-} to O-O related species). After 4 e^- oxidation, oxygen is released. Oxidised photosensitizer then reacts with a sacrificial reagent to go back to its initial state.

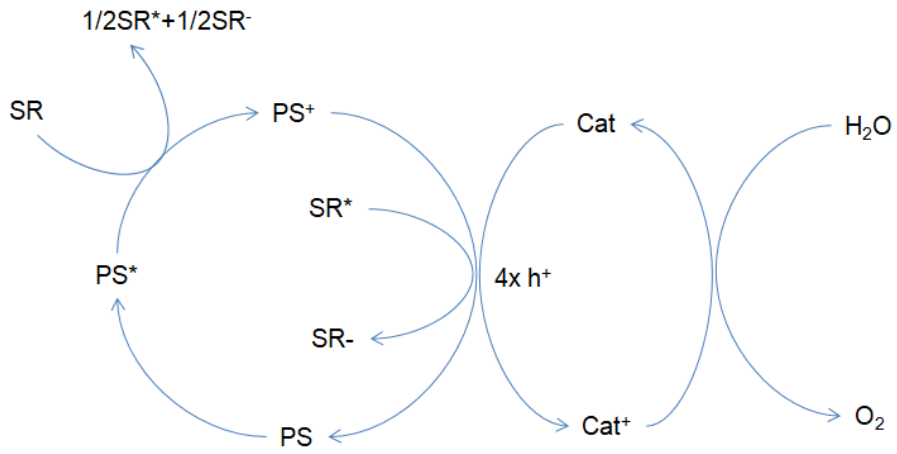

Figure 1.13. WOC initiated by photosensitizer being quenched by the sacrificial reagent.

The above figure shows the reverse case, where the sacrificial reagent first interacts with the excited photosensitizer. This can release radicalic species, which can be used in the later oxidation cycles. Oxidized photosensitizer then reacts with the catalyst, similar to the previous case. Thus, oxygen is released.

Among the limited examples of Fe-based photocatalytic dyads, only one system has been reported that incorporates a Fe(II) photosensitizer.[35] In that study, quenching of the excited Fe(II) state by the Co(III) catalyst was not observed, suggesting that the photocatalytic hydrogen evolution reaction (HER) was initiated through electron transfer between the excited Fe(II) carbene complex and a sacrificial electron donor, rather than the Co catalyst itself. Notably, the Fe(II) photosensitizer in this system was characterized by a ^{3}MC (triplet metal-centered) excited state, which is typically considered non-luminescent and unreactive in traditional photoredox schemes. Nonetheless, efficient hydrogen production was achieved, raising the possibility that a transient ^{3}MLCT state, though short-lived and not spectroscopically observed, could still play a mechanistic role. However, this remains a hypothesis without direct experimental confirmation.

1.5 Transient Absorption Spectroscopy (TAS)

Normally, photophysics studies of metal complexes, especially those of d_6, are done through photoluminescence spectroscopy.[76] Upon excitation of a certain band, the behaviour of the emitted light is studied. This is helpful to understand the photophysical and photochemical behaviour of emissive photosensitizers. However, not all photosensitizers have emissive excited states. Fe(II) and Co(III) are among these photosensitizers. As triplet and quintet MC states just vibrationally relax, no light is emitted upon this relaxation.[1,31,59,75]

To study the photophysics of such species, another spectroscopy method called transient absorption spectroscopy (TAS) is used. The aim of this technique is to measure the change of absorption after a solution of photosensitizer is excited with a laser, with a so-called pump, under white light, with a so-called probe. The spectra of the solution is collected at different times after the solution is pumped. This can either be done at nano to microsecond scale with TAS or at pico to nanosecond scale with ultrafast TAS.

The main feature of every TAS spectrum is the ground state bleach (GSB). As an absorbance band is excited, the electronic configuration of the excited species goes from the ground state to the excited state. As the ground state is less populated, the absorption will decrease. Along with this, new absorption bands will appear as well. These are the so-called excited state absorption (ESA). This is due to excitation of the excited electron or excitation to the hole left in the ground state.

1.6 Prussian Blue Analogues (PBAs)

Prussian Blue Analogues (PBAs) belong to a class of Hofmann-type coordination compounds, where cyanide ligands bridge two different transition metals (Figure 1.14).[14,20,21,81] Cyanide (CN^-) is a simple inorganic ligand consisting of a negatively charged carbon triple-bonded to a neutral nitrogen, with both atoms carrying lone pairs. Due to the high electronegativity and negative charge of carbon, primary metal coordination typically occurs through the carbon terminus. Once all cyanide carbon atoms are coordinated, available nitrogen lone pairs can bind to secondary metal centers, provided that steric hindrance around the carbon-bound metal is minimal.

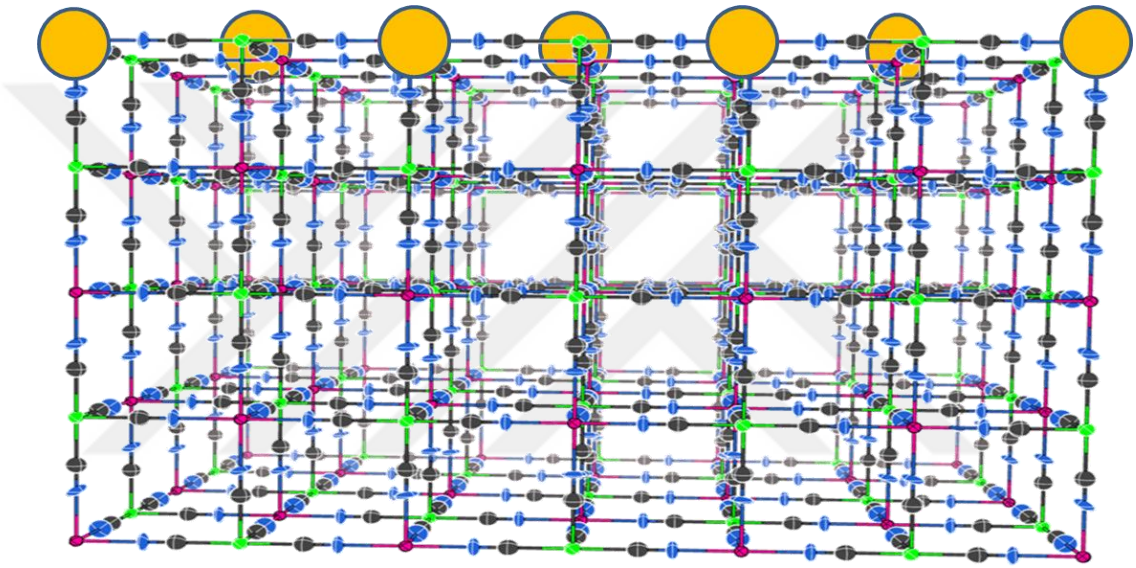

Figure 1.14. Crystal Structure of a PBA with a molecular formula of $M_x[M'(CN)_6]_y$.Reused with permission from Ref.[1].

This binding geometry leads to linear, M–C≡N–M' bridges, which commonly generate extended three-dimensional frameworks. Given the octahedral coordination geometry of most cyanometallates (with ~90° ligand–ligand angles), PBAs typically adopt cubic crystal structures. These particles often agglomerate into nanocubes, ranging from tens to hundreds of nanometers in size.

The simplicity of their synthesis, along with their well-defined crystalline structures, has made PBAs attractive for a variety of applications, including catalysis, magnetism, and sodium/potassium ion batteries.[81–83]

1.6.1 Catalytic Relevance of Prussian Blue Analogues (PBAs)

From a catalytic perspective, the coordination flexibility of cyanide is particularly significant. Not all nitrogen sites are fully coordinated, leaving open coordination sites on the metal centers.[14] These can interact with solvent molecules, such as water, introducing potential reactive sites for catalytic processes like water oxidation or reduction.

Because of their modular coordination environments and synthetic tunability, PBAs have been actively studied for their photophysical and electrocatalytic properties.[82,84,85] One of the earliest known examples is Fe(II)Fe(III) PBA, commonly known as Prussian Blue, which also holds historical significance as the first synthetic blue pigment. The importance comes from the MMCT transition around 700 nm, which causes Fe(II)-CN-Fe(III) to go to Fe(III)-CN-Fe(II). This can easily happen as the metal-to-metal distance is very short, around 4.8Å.[81]

In our previous works, we explored the catalytic capabilities of PBAs by systematically modifying the coordination environment at either the carbon-bound or nitrogen-bound metal centers, focusing particularly on the activity of water-coordinated metal sites. Our group has reported several key advances, including electrocatalytic water splitting using PBA frameworks[82], photocatalytic water splitting by integrating PBAs with semiconductors[20], tuning the local chemical environment of the Co site in CoFe PBAs to investigate structure–activity relationships[14,86–88] and employing pentacyanoferrate complexes as electron relays to mediate charge transfer between Co-based catalysts and various organic photosensitizers.[83]

1.7 Objective of the Thesis

Achieving efficient photosensitizer-catalyst communication is a key factor in achievingefficient photocatalysis. To study the dyad interactions, most groups prefer long bridging ligands, which are bound to slow down the impending quenching. Catalytic performance and photophysical interactions of PBA-based dyads with

Fe(II) cyanopolypyridyls are yet to be examined. Cyanide acts both as a strong field ligand and a short-distance bridging ligand. The cobalt site can be modified further to both increase the solubility of the dyad and decrease the linkage in the PBA network. The latter part is important for achieving porous structures. Thus, well-studied Fe1 and Fe2 are linked to Co(bpy) and Zn(bpy) cores to study the photophysics and catalytic efficiency of such dyads as the focus of this thesis (Figure 1.15).

Chapter Three focuses on the catalytic systems consisting of Fe1 and Fe2 photosensitizers. The photophysics implications of binding various transition metals are studied through ultrafast-transient absorption spectroscopy. These implications are justified through metal-ligand interactions as observed through FTIR, UV-Vis, and X-Ray Absorption Spectroscopies. For the first time, the photophysical behaviour of higher-lying MLCT bands is inspected. Quenching behaviour of FeCo dyads is inspected through fitting of TAS kinetics.

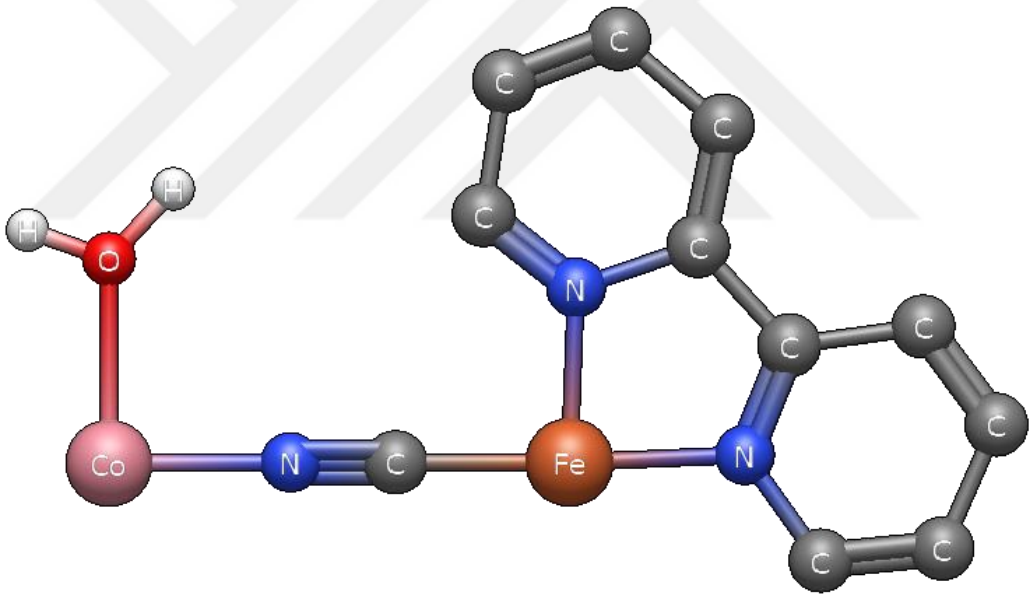

Figure 1.15. A schematic representation of the Co catalyst bridged to the Fe(II) cyanopolypyridyl.

CHAPTER 2

2 Experimental

2.1 Chemicals and Reagents

Anhydrous cobalt (II) chloride (Sigma-Aldrich), ferrous ammonium sulphate hexahydrate (Sigma-Aldrich),anhydrous zinc (II) chloride (Sigma-Aldrich), 2,2'-bipyridyl (Acros Organics), potassium cyanide (Sigma Aldrich),sodium persulfate (Acros Organics), tetrabutylammonium perchlorate (Sigma-Aldrich),cobalt (II) nitrate (Sigma-Aldrich),potassium hexacyanoferrate (III) (Roth), sodium dihydrogen phosphate and sodium hydrogen phosphate (Sigma-Aldrich), acetone (Sigma-Aldrich), diethylether (Aldrich), chloroform (Sigma-Aldrich), methanol (Sigma-Aldrich) were used without further purification. Aqueous solutions were prepared with Milli Q deionized water (resistivity: 18 MΩ*cm).

2.2 Synthesis of Fe1 and Fe2

Both photosensitizers have been prepared according to Schilt's method.[89]

Dicyano-bis-(2,2'-bipyridine)-iron(II) Trihydrate, Fe1, $[Fe(bpy)_2(CN)_2]\bullet 3H_2O$:
A 7.5 mmol of 2,2-bipyridine (1,10-phenanthroline) together with 2.5 mmol of ferrous ammonium sulfate hexahydrate were dissolved in 100 mL of de-ionized water to obtain a dark-red solution and heated to 85°C. After reaching the desired temperature, a freshly prepared solution of 2.5 g of potassium cyanide in 5 mL of de-ionized water is added all at once to the hot solution. After thorough stirring for 2 hours, the hot mixture is set aside to cool at room temperature and aged overnight. The dark violet (almost black precipitate obtained was washed three timeswith 250 mL of deionized water and decanted. 5 mL of concentrated sulfuric acid was added to the precipitate after the final decantation, and it was diluted slowly with 250 mL of deionized water while stirring. The recrystallized product was collected by suction filtration, washed with small portions of water until free of sulfuric acid, sucked dry, and finally dried in the desiccator at room temperature. C: 58.8%. N: 18.7%. H: 4.14%.

Potassium Tetracyano-mono-(2,2'-bipyridine)-iron(II) Trihydrate, Fe2, $K_2[Fe(bpy)(CN)_4]\cdot 3H_2O$:

500 mg of $[Fe(bpy)_2(CN)_2]\cdot 3H_2O$ was dissolved in 100 mL aqueous solution containing 2.5 g of KCN in a conical flask. The conical flask was sealed, and the solution was heated at 90 ^oC for about 20 hours. Then, the solution was allowed to cool down at room temperature and filtered to remove any unreacted solids. The volume of the filtrate was reduced to about 20 mL in the rotatory evaporator, and crystallized in the refrigerator to obtain a dark orange-red crystalline product. The crystallized product was collected by suction filtration, washed with small portions of acetone, and finally dried in the desiccator at room temperature.C: 37.6%. N: 19.5%. H: 2.45%.

2.3 Synthesis of Cobalt and Zinc Precursors

$CobpyCl_2$ and $ZnbpyCl_2$ are prepared following previously established protocols.[90] Briefly, 2 mmol of 2,2'-dipyridyl in 20 mL of acetone was mixed with a solution containing 2 mmol anhydrous cobalt/zinc(II) chloride in 20 mL of acetone. The resulting solution was stirred for two hours, filtered, and dried in a desiccator to obtain a light-blue or white precipitate, respectively. For Co: C: 42.2%. N: 9.61%. H: 2.82%. For Zn: C: 41.4%. N: 9.01%. H: 2.68%.

2.4 Synthesis of FeM1 Dyads (M=Co, Zn)

0.15 mmol of $[Fe(bpy)_2(CN)_2]\cdot 3H_2O$ in 20 mL of methanol was added to a solution containing 0.15 mmol of $CobpyCl_2$/ $ZnbpyCl_2$ in 20 mL of methanol and mixed for 3 hours. The solution obtained was filtered to remove any unreacted solids. Slow diffusion of diethyl ether into the solution yielded the formation of reddish-brown/open reddish powders, respectively. The powder was collected by centrifugation and washed with small portions of acetone, and dried in the oven at 60^oC. For **FeCo1**: C: 52.9%. N: 15.0%. H: 4.01%. For **FeZn1**: C: 48.8%. N: 14.7%. H: 3.13%.

2.5 Synthesis of FeM2 Dyads (M=Co, Zn)

0.15 mmol of $K_2[Fe(bpy)(CN)_4]\bullet 3H_2O$ in 20 mL of methanol/water (1:1) was added to a solution containing 0.15 mmol of $CobpyCl_2$/$ZnbpyCl_2$ in 20 mL of methanol/water (1:1). The resulting solution was stirred vigorously for 3 hours and allowed to stand overnight. Then, the obtained brown/open brown, respectively, precipitatesare centrifuged, washed with de-ionized water, and dried in the oven at 60^{o}C. For **FeCo2**: C: 39.7%. N: 11.3%. H: 3.01%. For **FeZn2**: C: 44.9%. N: 20.1%. H: 2.77%.

2.6 Synthesis of CoFe PBA

CoFe PBA is synthesized according to previous literature.[20]A 30 mL cobalt(II) nitrate solution with a concentration of 30 mM is reacted with 30mL 20 mM Potassium hexacyanoferrate(III) for 3 hours. Subsequent centrifugation is followed by drying the solid in the oven at 60 °C.C: 18.0%. N: 20.5%. H: 2.99%.

2.7 Instrumentation

2.7.1 UV-Visible Spectroscopy

UV-Vis absorption spectra of the solutions were obtained using an Agilent Cary 5000 UV–Vis-NIR spectrophotometer, using a quartz cuvette with a path lengthof 1 cm. All measured solutions had a concentration of 30 μM.

2.7.2 Attenuated Total Reflectance- Fourier Transform Infrared Spectroscopy (ATR-FTIR)

FTIR spectra were recorded on Bruker Alpha Platinum–ATR Spectrometer model. The spectra were recorded in transition mode within the wavenumber range of 400 – 4000 cm^{-1} for 64 scans and 4 cm^{-1} resolution.

2.7.3 CHNS Elemental Analysis

The elemental analysis of carbon, hydrogen, and nitrogen were carried out on Thermo Scientific FLASH 2000 Series CHNS/O elemental analyzer. The measurements were performed using BBOT as a standard and V_2O_5 as a catalyst. The data is reported as mass percent.

2.7.4 Differential Pulse Voltametry (DPV)

Electrochemical experiments were carried out on a Gamry Instruments Interface 1000 potentiostat/galvanostat at 25 ºC. Using the conventional three-electrode setup, with Pt wire as the counter electrode, Ag/AgCl (3.5 M KCl) as the reference

electrode, and glassy carbon (GC) coated electrode (3 mm in diameter) as the substrate for working electrode.The electrochemistry was performed in a N_2-saturated solution of 1mM sample solution in 0.1 M TBAP Methanol solution.

2.7.5 X-Ray Photoelectron Spectroscopy (XPS)

XPS analysis was performed on Thermo Fisher Scientific K–Alpha X-ray photoelectron spectrometer, using Al Kα micro-focused monochromator, with a photon energy of 1486.6 eV, as the X-ray source and equipped with a flood gun for charge neutralization. Charge correction is done according to the previously assigned Co species of CoFe PB.

2.7.6 X-Ray Absorption Spectroscopy (XAS)

XAS analysis is conducted on the HESEB Beamline of the SESAME synchrothron. Previously set Fe and Co L-edge parameters on the beamline are used. Total electron yield is calculated using the current drain from the mirrors that are hit by the incident and final beams. Normalization is done by subtracting the lowest point of the L3 edge from the data. The data is divided by the maxima of the selected (generally e_g) peak.

2.7.7 Water Oxidation Photocatalysis

Photocatalytic experiments were conducted in a Pyrex flask totally sealed with a septum with a 4.5 mL headspace. A 10 mL 0.1 M pH7 phosphate buffer solution (PBS) containing 10 mg catalyst, 5 mM sodium persulfate ($Na_2S_2O_8$), were prepared. A solar light simulator with a 200W Xe lamp is used. The spot is adjusted to 76 mW cm^{-2} with a Si detector. A 420 nm cutoff filter is used. First, the round bottom flask is sonicated for half an hour. Then, the mixture was purged with N_2 gas thoroughly for 25–30 min. The photocatalytic experiment was carried out for 3 hours, and the amount of oxygen evolved was determined by injecting 100 μL of the headspace gas at a 1-hour interval into a gas chromatograph twice (Agilent 7820, a gas chromatograph equipped with a molecular sieve and a thermal conductivity detector

(TCD), using argon as the carrier gas). In cases of catalyst addition, 10 mg photosensitizer compound and 10 mg CoFe PBA is added.

2.7.8 Turnover Number (TON) Calculation

TON was calculated, assuming that evolved oxygen was achieved per every existing Co in the catalyst or Fe in the photosensitizer.

$$TON = \frac{Moles\ of\ O_2}{Moles\ of\ Co/Fe\ \ (as\ indicated\ above)}$$

(eq. S1)

2.7.9 Ultrafast-Transient Absorption Spectroscopy

We utilized a custom-built ultrafast transient absorption (TA) setup for the fs-TA measurements. A Ti:Sapphire regenerative amplifier (Coherent, Astrella) generated ~85 fs pulses centered at ~800 nm, operating at a 1 kHz repetition rate. The laser output was divided: one portion was focused onto a rotating CaF_2 crystal to produce a white-light continuum spanning 300-800 nm, subsequently divided into reference and probe beams for the measurements. The second portion was directed into an optical parametric amplifier (TOPAS prime, Light Conversion) to generate tunable pump pulses, specifically 370 nm, and 570 nm pulses for this study. A mechanical chopper reduced the pump pulse repetition rate to 500 Hz for alternating pump-on and pump-off measurements. The relative polarization of the pump and probe beams was adjusted to the magic angle (54.7°) using a Berek compensator and polarizer. Probe and reference spectra were recorded with a Czerny-Turner spectrograph (Princeton Instruments, SP2150) equipped with CCD detectors (Pascher Instruments AB). Transient absorption data were analyzed using the python-based KiMoPack package, where the coherent artifact region was removed (chirp correction) and global fitting analysis was performed on the chirp-corrected data.

CHAPTER 3

3.1 Introduction

Although dyad systems for photocatalytic water splitting gathered large interest, efficient systems can only be achieved by the usage of photosensitizers and/or catalysts consisting of expensive rare earth metals.[8,22,23,36,79]Dyad bridging is done through hard-to-synthesise organic ligands[23,36,79], which increases the cost and decreases the scalability of such catalysts. The research of such dyad systems consisting of first transition row metals, which are cheap, is quite rare.[35,79] Especially, Fe(II) photosensitizers tend to be quenched through not the energetically favored MLCT state but the relaxed ^{5}MC state.[29,35,91]

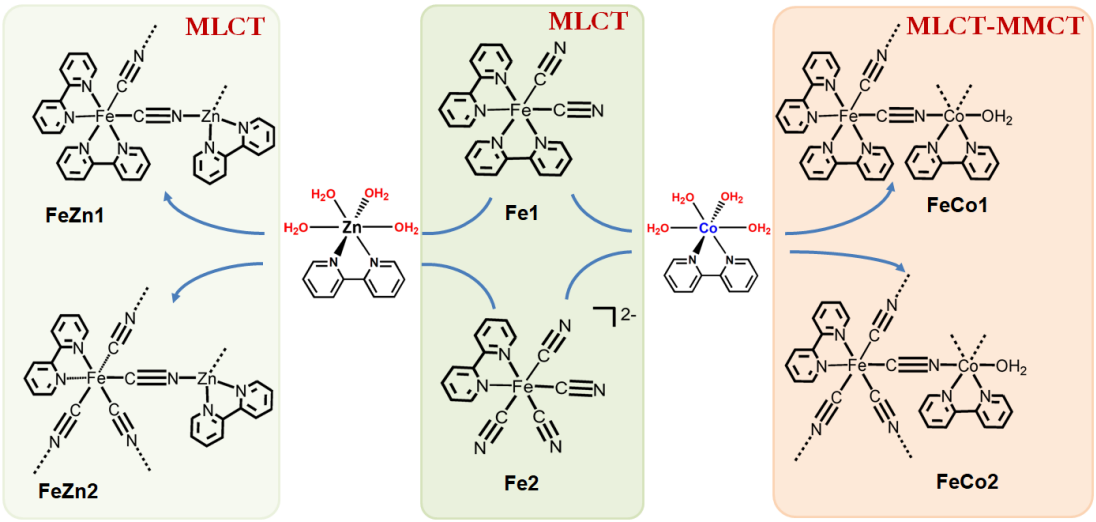

Figure 3.1. Scheme of **Fe** photosensitizers and **FeZn** networks with MLCT states and **FeCo** networks with coupled MLCT-MMCT states.

Here, in this work, we studied the coordination environment and photophysics of **Fe1** and **Fe2** photosensitizers in PBA networks to establish a structure-property

correlation (Figure 3.1). Zinc is selected as a transition metal that will not lead to an MMCT with the Fe ions, whereas cobalt is selected due to its catalytic activity. Cyanide ligand is selected both to destabilize the ^{5}MC state and to place Co and Fe sites in close proximity (M-M distance is around 5Å. Catalytic activity is probed through water oxidation. Photophysics of Fe (II) cyanopolypyridyls are studied

through ultrafast-transient absorption spectroscopy. The ligand field strength effects are explained by FTIR, UV-Visible, and X-Ray Absorption Spectroscopy techniques.

3.2 Results and Discussions

3.2.1 Synthesis

As shown in our previous works, $Co(bpy)Cl_2$ and its zinc analog have been synthesised. Upon dissolving the blue colored tetrahedral Co complex in methanol, the solution turnedpinkish. This seems to be due to solvent coordination to Co, which causes Co to go from tetrahedral to octahedral. Fe(II) cyanopolypyridyl complexes have been synthesised according to previous literature.[92] Due to solubility concerns with precursors, dyads with **Fe1** have been synthesised in MeOH, and dyads with **Fe2** have been synthesised in a 1:1 water:MeOH solution. Although **Fe2**has low solubility with water, centrifuging was enough to achieve the solid dyad.Precipitation with diethyl ether and chloroform washing had to be done with **Fe1** dyads. It is noticed that **Fe1** dyads are more soluble than **Fe2** dyads. This is due to decreased linkage due to decreased cyanide number. Co dyads are more soluble than Zn dyads. This could either be due to Co sites being octahedral and Zn being tetrahedral or just due to polarisation difference between Co and Zn.

3.2.2 Characterization

3.2.2.1 UV-Visible Absorption Studies

Methanol solutions of all compounds were prepared for UV-visible spectroscopy analysis, with concentrations around 30-300 μM to achieve 0.4 absorbance. Methanol solutions of all compounds exhibit two main bands at 370 nm and 570 nm, which are attributed to ^{3}MLCT bands of the Fe(II) chromophores (Figure 3.2.(a) and Figure 3.2.(b)).[93,94]

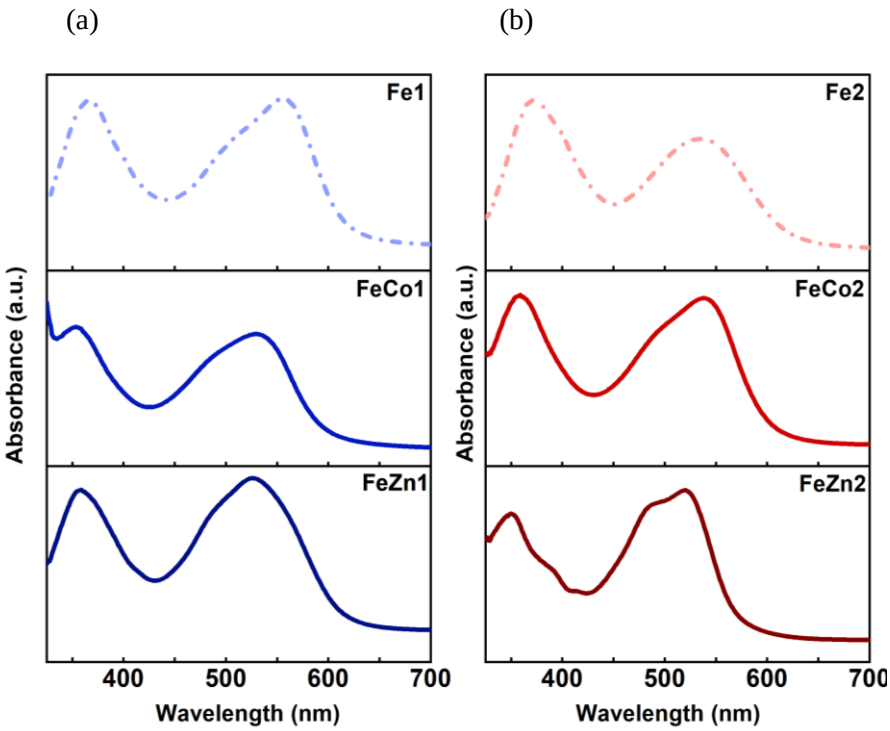

Figure 3.2. (a) UV-Vis spectra of **Fe1**, **FeCo1,** and **FeZn1** between 325-700 nm. (b) UV-Vis spectra of **Fe2**, **FeCo2**, and **FeZn2**between 325-700 nm.

These transitions occur from the t_{2g} band of Fe(II) center to π* orbitals of the 2,2'-bipyridyl ligand. It is important to note that the 370 nm band also contains the Laporte (d-d) forbidden ^{1}MC transition (from Fe t_{2g} to e_g), and the 570 nm band is assumed to contain Laporte and spin forbidden ^{3}MC transitions (from t_{2g} to e_g). Both of these transitions are less allowed than the MLCT transitions, which is due to both the rather high dipole moment of methanol and the forbidden nature of the MC transitions. Although **Fe2** shows only one band at around 550 nm, it is considered to be the result of two overlapped bands (Figure 3.2.(b)). This becomes apparent upon binding of the metals to the nitrogen site, as **FeCo2** and **FeZn2** show double bands. Going from **Fe** to FeCo and then to**FeZn**, increased MLCT bandgaps are obtained, which are of around 10-40 meV(Figure 3.2.(a,b)).[95] This change is attributed to the change in Fe t_{2g} level. As the second metal ions are bound to the N-atom of the cyanide ligand, they act as Lewis acids, causing π-back donation. The relatively weaker π-back donation between the Fe t_{2g} and the π* of the bound CN ligand (–CN–M) leads to the stabilization of the Fe t_{2g} level in **FeM1** and **FeM2** (M = Co and Zn) compounds compared to those in **Fe1** and **Fe2**. No change in bpy π* level is expected, since the coordination environment of bpy groups remains the same.[93,95]

3.2.2.2 Infrared Studies

O-H stretchings are observed in the 2900-3650 cm^{-1} region. These features are attributed to chemisorbed and physiosorbed water/hydroxyl species. Peaks of ν(C-H) are obtained in the 2950-3150cm^{-1} region.[14]

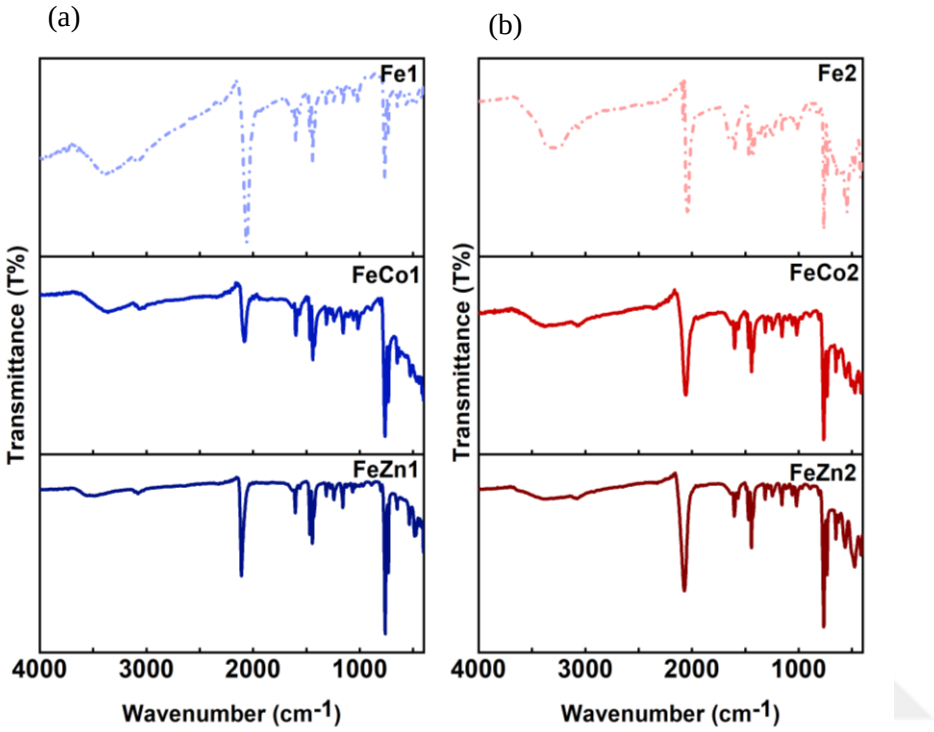

Figure 3.3. FTIR spectra of (a) **Fe1**, **FeCo1**, and **FeZn1**and (b) **Fe2**, **FeCo2,** and **FeZn2** in the 400-4000 cm^{-1} region.

This is due to C-H bonding in the bipyridyl groups. Normally, H_2O bending would be observed for PBAs. This peak overlaps with other vibrations of the bipyridyl group, such as C-C and C-N stretching/bending. One would also observe Fe-C and M-N (M= Co, Zn) below 800 cm^{-1}. But C-C bendings and Fe-N and M-N of bipyridyl groups also obscure these signals. Thus, structural characteristics of only the Prussian blue could be obtained from ν(C-N).

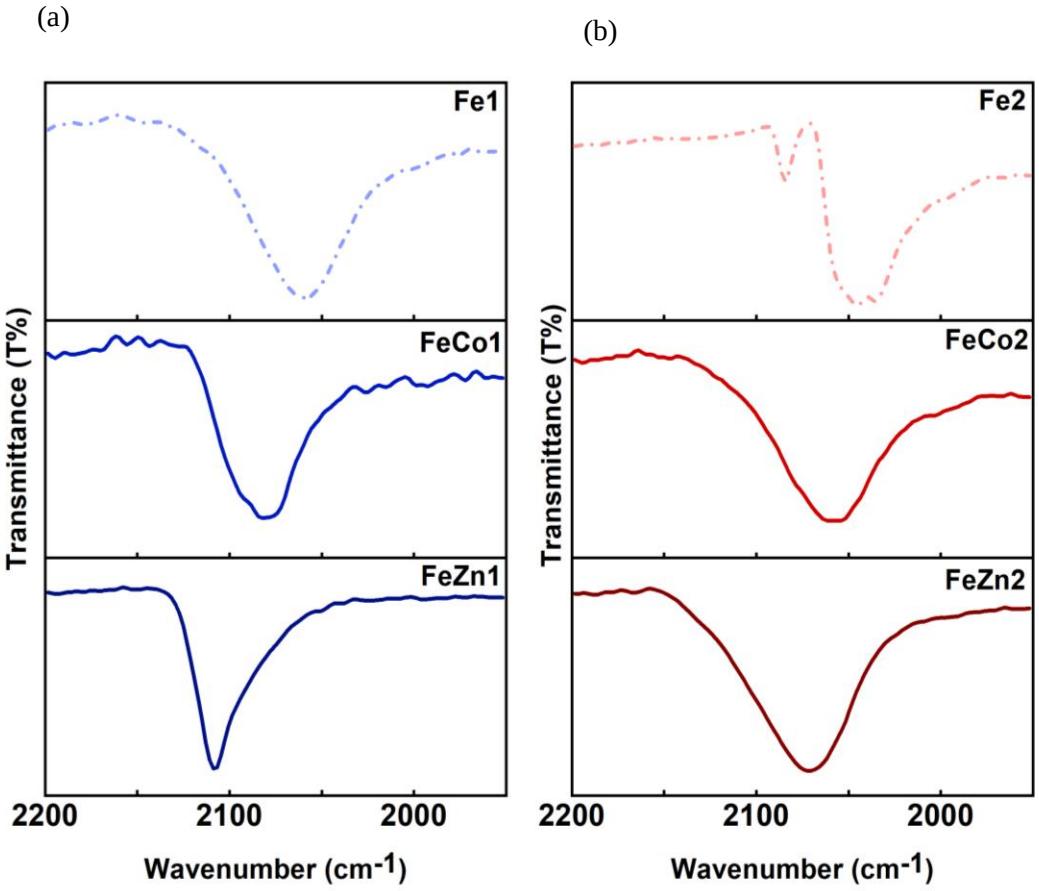

Figure 3.4. ν(CN) stretching of (a)**Fe1**, **FeCo1,** and **FeZn1**and (b) **Fe2**, **FeCo2,** and **FeZn2**in the1950-2200cm^{-1} region.

All compounds show asymmetric and symmetric cyanide [ν(CN)] stretches in the 2000-2200 cm^{-1} interval (Figure 3.4(a,b)).[14,81] Two peaks are seen with **Fe1**, which are attributed to $\nu(CN)_{as}$ and $\nu(CN)_{s}$, respectively (Figure 3.4(a)). For **Fe2**, in addition to these peaks, one peak around 2080 cm^{-1} is obtained (Figure 3.4(b)). Although this peak has not been previously attributed to any vibrational mode, the weak intensity suggests that this mode is a combination band, originating from the combination of 4 CN ligands. Similar to UV-Vis Spectroscopy, a trend is observed, where ν(CN) frequency increases going from **Fe** to **FeCo** and then to **FeZn** compounds (Figure 3.4. (a,b)). This trend is in agreement with the previous trends of other PBAs.

As previously mentioned, the cyanide ligand has two main molecular orbitals, filled σ* (HOMO) and empty π* (LUMO), which interact with metals, creating a σ-donation and a π-back donation interaction, respectively.[81]The cyanide bond strength is, thus, sensitive to the nature of the binding metal, including its oxidation number

and the electronegativity. Since both the HOMO and LUMO of cyanide have anti-bonding characters, decreasing the electron density of these orbitals results in increased bond strength. The stabilization of the t_{2g} level observed by UV-Vis spectroscopy studies and the shift of the CN stretch to higher wavenumbers suggest an enhancedσ donation between the Fe center and the CN ligand when secondary metal ions are coordinated to the N site of the CN ligand.

3.2.2.3 XPS Studies

The high-resolution XP spectra of N, Fe, and Co elements of **FeCo1** and **FeCo2** are displayed in Figures3.5-7. XP spectra of $CoFe(CN)_6$ (CoFe PBA) are also analyzed as a reference for comparative analysis.

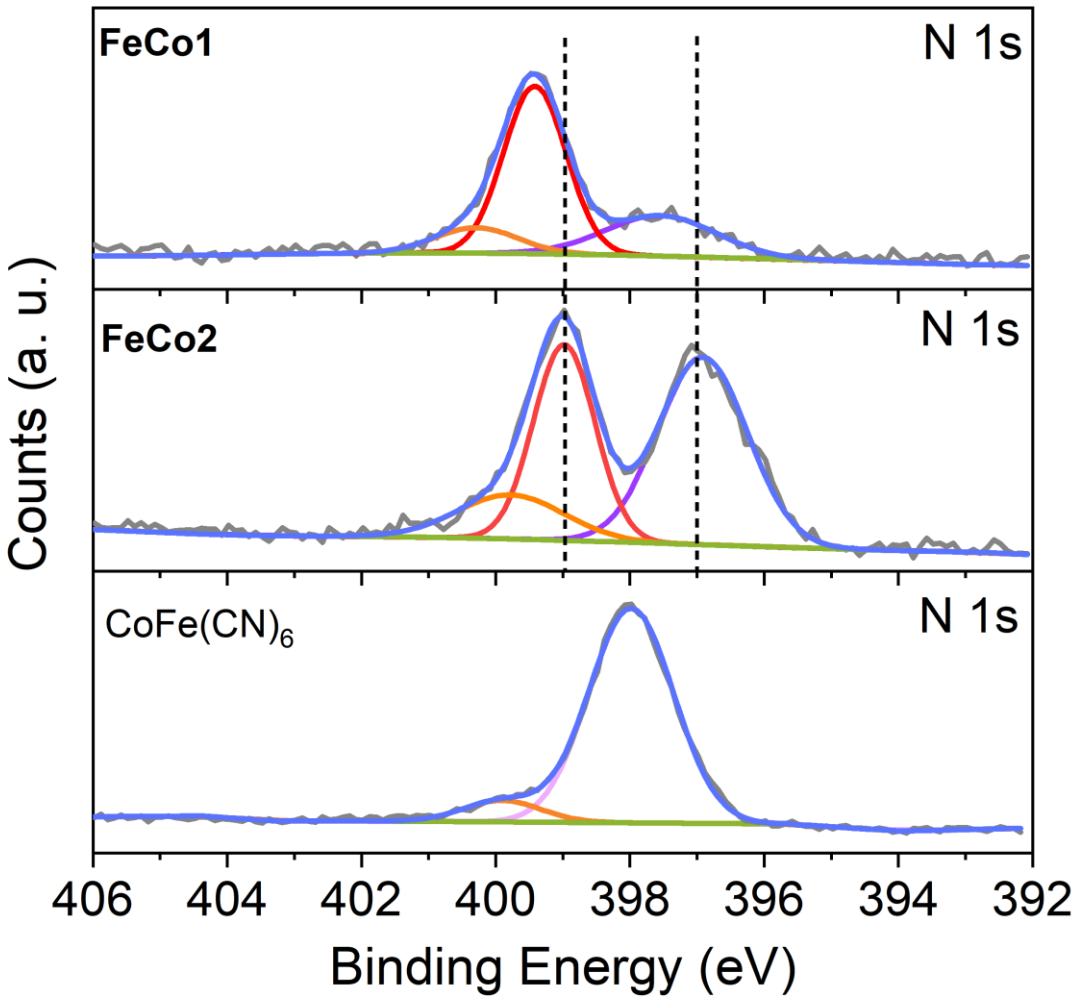

Figure 3.5. N 1s XP spectra of **FeCo1**, **FeCo2,** and CoFe PBA.

The N 1s spectrum of CoFe PBA shows two distinct peaks at binding energies of 398.0 eV and 400.0 eV, corresponding to nitrogen in C≡N and N–H bonding environments (Figure 3.5).[96]In contrast, the N 1s spectrum of **FeCo2** is deconvoluted into three peaks located at 397.0 eV, 399.0 eV, and 399.8 eV, which are attributed to C≡N, pyridyl-N, and N–H, respectively.The shift of the C≡N peak to a lower binding energy in **FeCo2** compared to CoFe PBA suggests variations in the local chemical environment, probably due to the presence of both bridging and terminal cyanide ligands within the structure. Similarly, the N 1s spectrum of **FeCo1** resembles that of **FeCo2**; however, the observed peaks shift to higher binding energies, indicating a distinct electronic environment in the **FeCo1** structure. Moreover, the reduced intensity of the C≡N peak in **FeCo1** aligns with a lower cyanide ligand concentration, further highlighting structural differences among the samples.

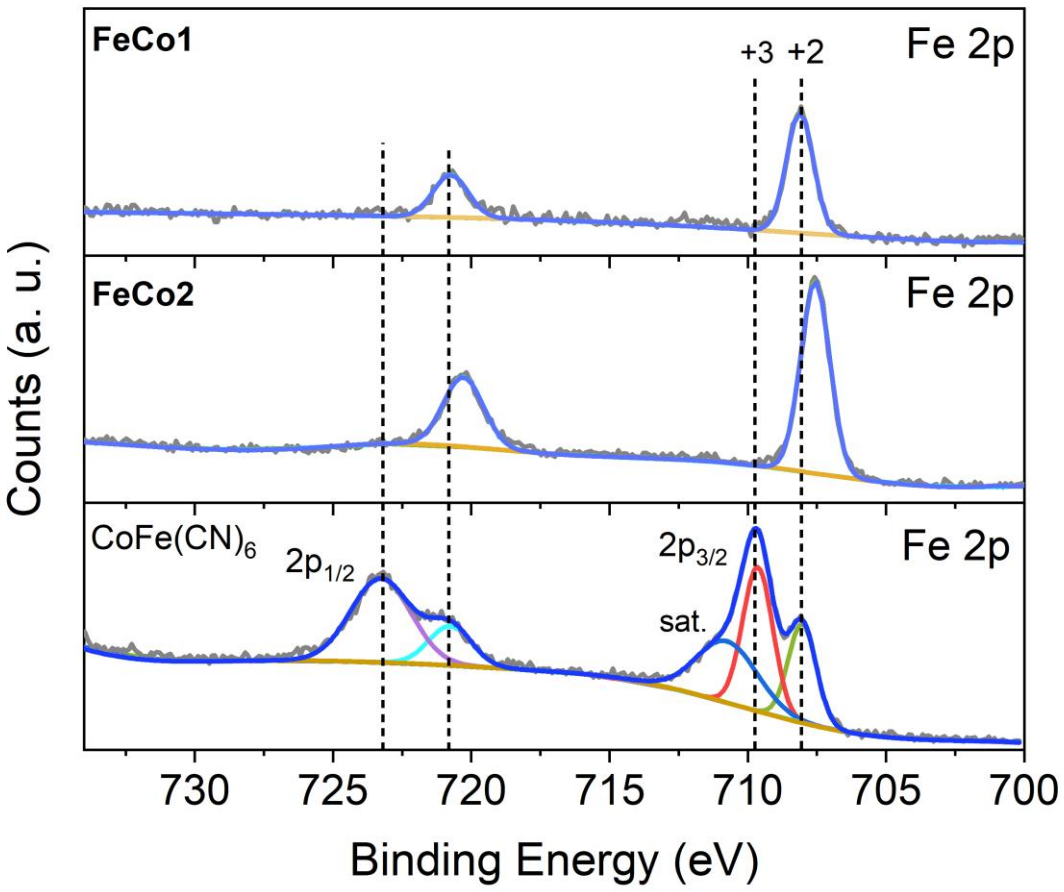

Figure 3.6. Fe 2p XP spectra of **FeCo1**, **FeCo2,** and CoFe PBA.

For all compounds, the Fe 2p signal is deconvoluted into Fe $2p_{3/2}$ and Fe $2p_{1/2}$peaks (Figure 3.6). In CoFe PBA, the Fe $2p_{3/2}$ peak exhibits contributions from both Fe^{2+}

and Fe^{3+} oxidation states, appearing at 708.1 eV and 709.7 eV, respectively, along with a characteristic satellite shake-up peak at 710.9 eV.[97,98]However, the Fe^{3+} species is not identified in the Fe 2p spectra of **FeCo2** and **FeCo1**, suggesting that these compounds exclusively contain Fe^{2+}. Furthermore, the Fe 2p peaks in **FeCo1** are shifted to higher binding energies compared to **FeCo2**, indicating a more electron-deficient iron center. This shift is attributed to the coordination environment in **FeCo1**, where two π accepting bipyridyl ligands are bound to the iron center, whereas **FeCo2** contains only a single bipyridyl ligand in its coordination sphere (Figure 3.1).

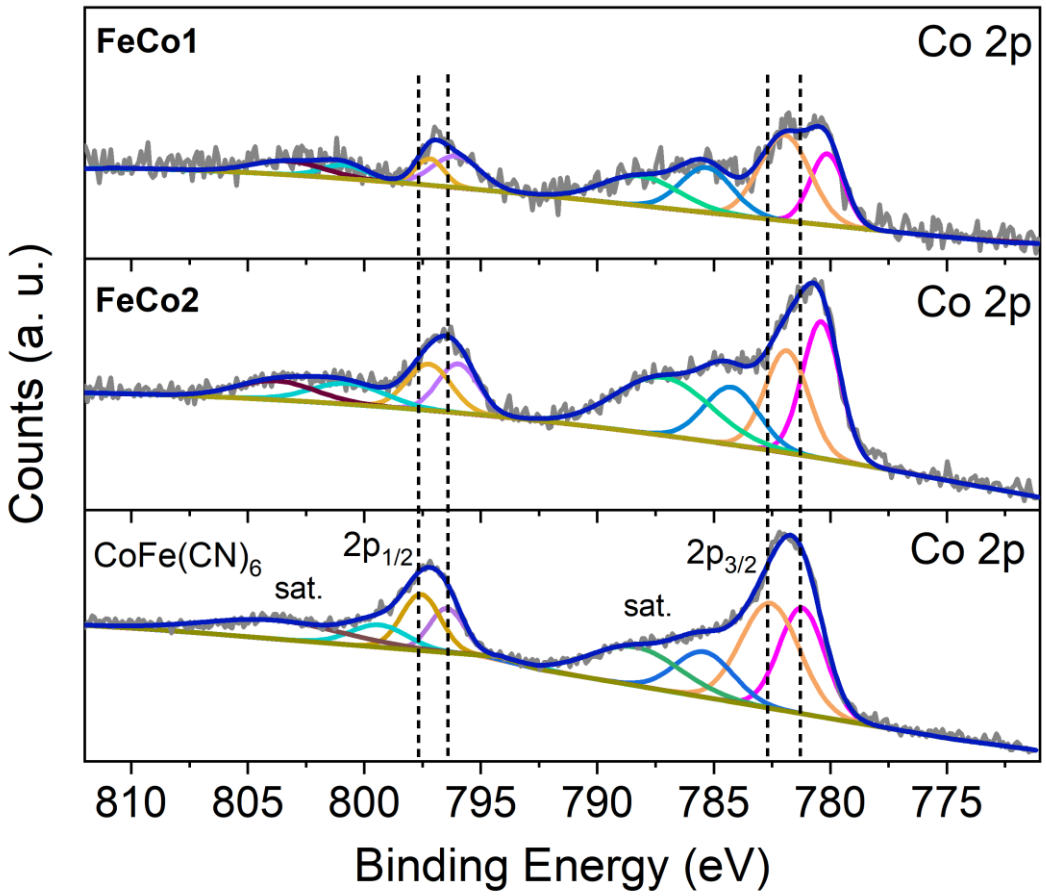

Figure 3.7. Co 2p XP spectra of **FeCo1**, **FeCo2,** and CoFe PBA.

A clear assignment of Co^{2+} and Co^{3+} oxidation states is challenging due to peak broadening, multiplet splitting, and the contribution of satellite peaks (Figure 3.7).[99] The Co $2p_{3/2}$ and Co $2p_{1/2}$ signals can be deconvoluted into two primary components, accompanied by shake-up satellite peaks at higher binding energies. Previous studies

indicate that the Co $2p_{3/2}$−$2p_{1/2}$ spin-orbit splitting is typically around 15 eV for diamagnetic Co^{3+} complexes and 16 eV for paramagnetic Co^{2+} species.[100,101] Furthermore, Co^{2+} ions generally exhibit broader $2p_{3/2}$ and $2p_{1/2}$ lines with more intense satellite features compared to Co^{3+}.[99,102]The presence of broad main peaks and strong satellite signals in the spectra confirms the existence of Co^{2+}cations.The possible presence of $Co^{3+}$is suggested by the observed spin-orbit splitting values, which range between 15–16 eV, an intermediate region between those of pure Co^{2+} and Co^{3+}. Nevertheless, a definitive conclusion regarding the precise oxidation states of cobalt cation on XPS remains challenging. Notably, for **FeCo1** and **FeCo2**, the cobalt spectra exhibit a slight shift to lower binding energies, indicating differences in the local chemical environments of the cobalt centers within these structures. For a comprehensive comparison, the XPS results of **FeZn1**and **FeZn2** samples are presented in Figure 3.8-10. The N 1s and Fe 2p spectra of these compounds exhibit profiles that closely resemble those observed for **FeCo1** and **FeCo2**, demonstrating consistent electronic and chemical properties across the series. This similarity reinforces the validity of the interpretations used in describing the XPS analysis.

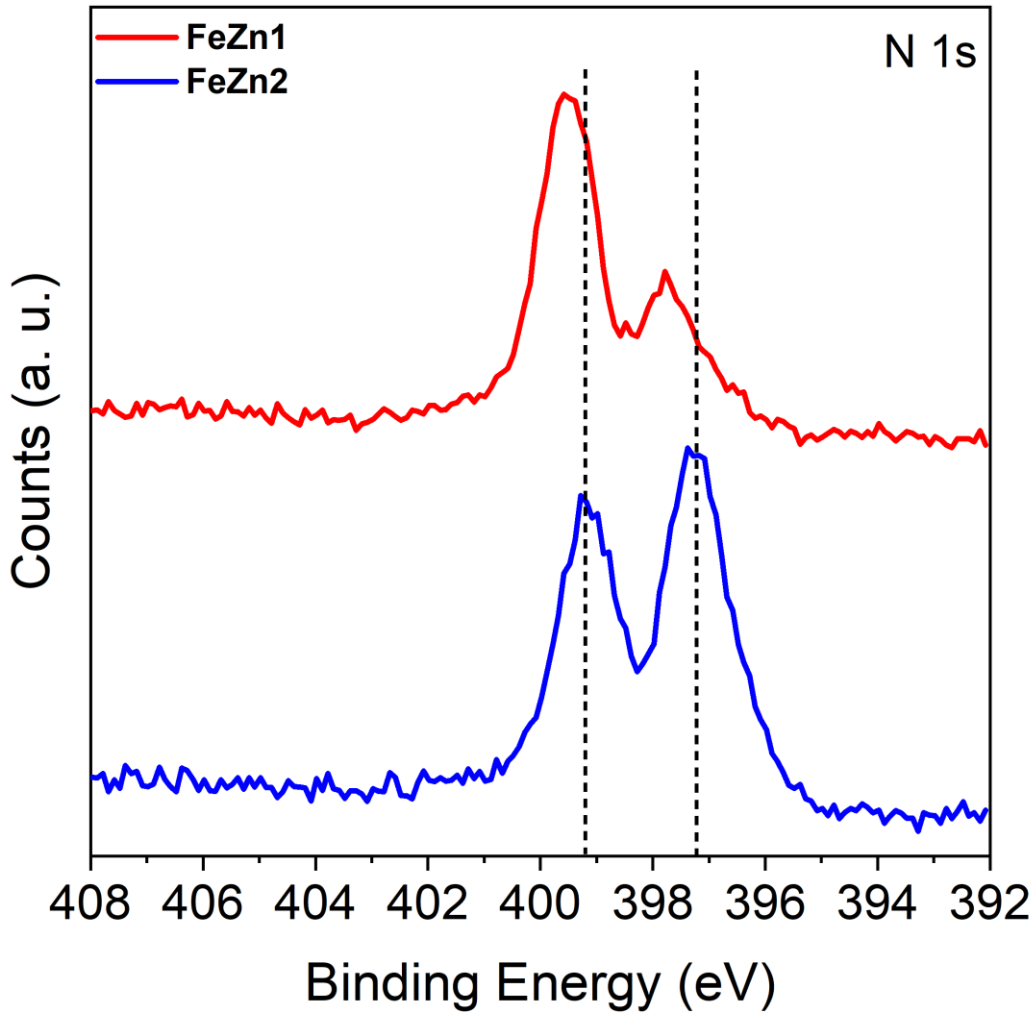

Figure 3.8. N 1s XP spectra of **FeZn1** and **FeZn2**.

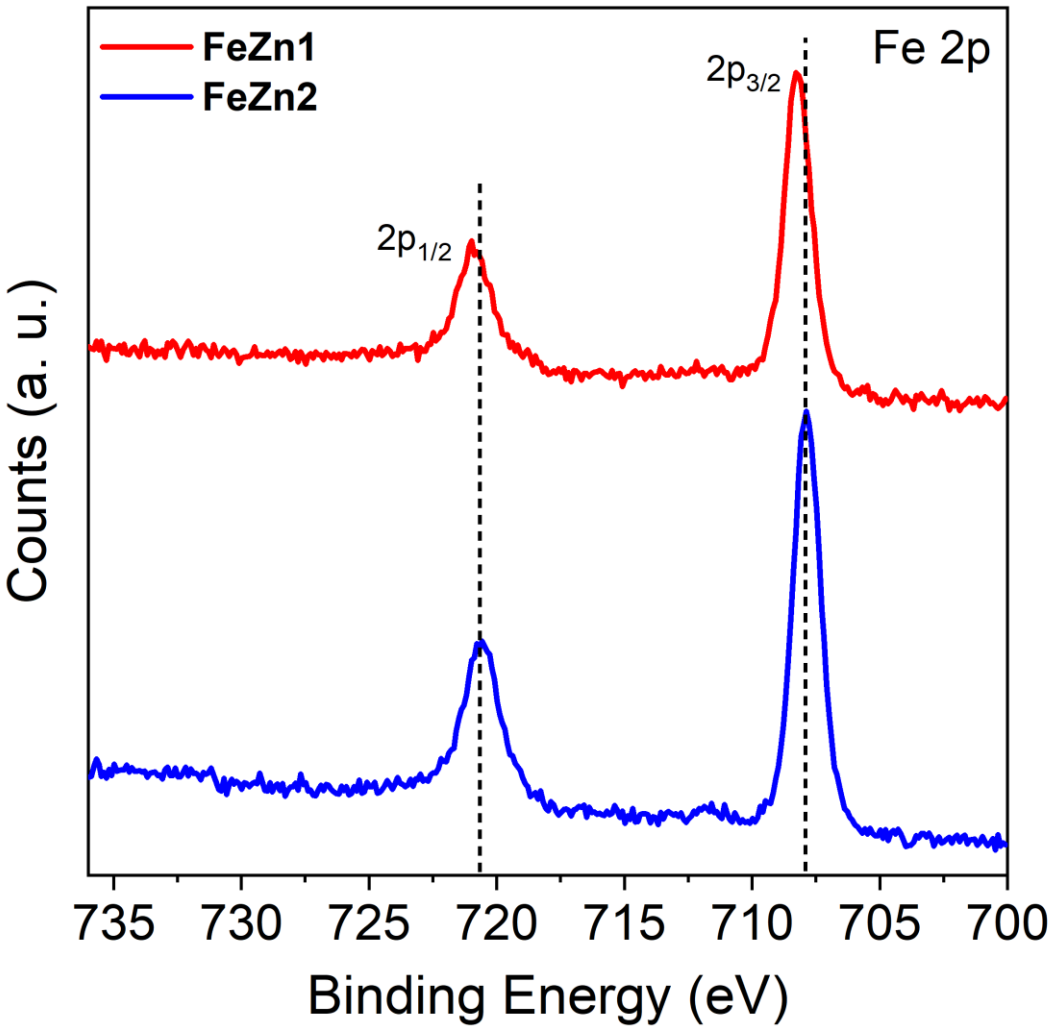

Figure 3.9. Fe 2p XP spectra of **FeZn1** and **FeZn2**.

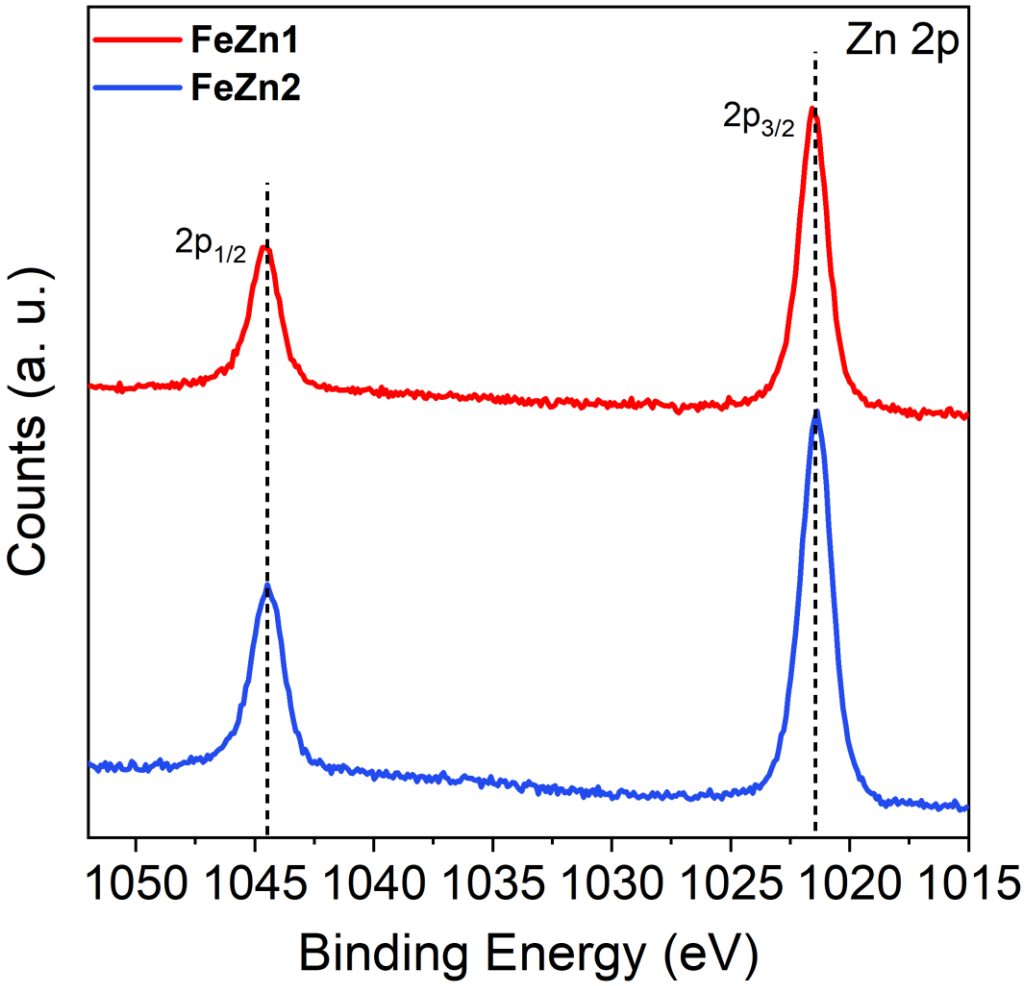

Figure 3.10. Zn 2p XP spectra of **FeZn1** and **FeZn2**.

3.2.2.4 XAS Studies

X-ray absorption spectroscopy studies were employed in the HESEB beamline of the SESAME synchrotron. For Co and Fe, L-edge measurements were performed, where electronic transitions from core $2p_{3/2}$ to molecular orbitals occur. Normally, with transition metal L-edge XAS, major signals come from metal-based orbitals.[40,48,103] However, with π-accepting ligands, new excited states can occur, which also show up as major peaks in the spectrum.

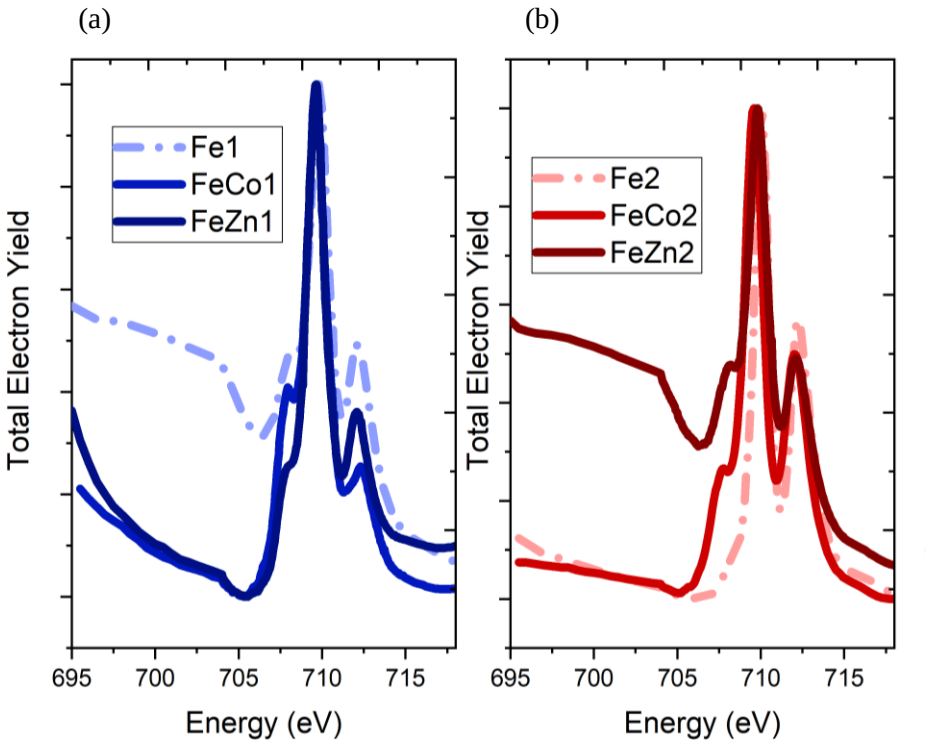

Figure 3.11. (a) Normalized Fe L3-Edge XA spectra of **Fe1**, **FeCo1,** and **FeZn1**. (b) Normalized Fe L3-Edge XA spectra of **Fe2**, **FeCo2,** and **FeZn2**.

From previously measured spectra of cyanopolypyridylferrates, it has been reported that the ordering of orbital energies is cyanide π*, Fe e_g*, and bpy π*, decreasingly.[38,48,104] Going from simple Fe compounds to dyads, e_g to CN π* ratio stays the same while e_g to bpy π* ratio decreases. This shows that Fe can communicate with Co and Zn-bound bpy species. However, this should not result in the previously discussed MLCT band shift. One small feature is observed to the right of the CN π* band. This is attributed to the weakly interacting empty CN σ* orbital (Figure 3.11.(a,b)). Generally, low-spin Fe^{3+} shows e_g feature as double peaks due to

Jahn-Teller distortion. Moreover, Fe^{3+} should exhibit a t_{2g} signal at around 704 eV, neither of which is observed in the compounds of interest. An oxidation state of 2+ for Fe sites is also in good agreement with FTIR and XPS measurements. It was also noticed that e_g signal is stabilized once metal ions are coordinated to the cyanide ligand. This is due to the previously mentioned decrease of the σ-donation characteristic in the FTIR part. This stabilization is around 200 meV with **Fe1**-based dyads and 400 meV with **Fe2**-based ones(Figure 3.12. (a,b)).

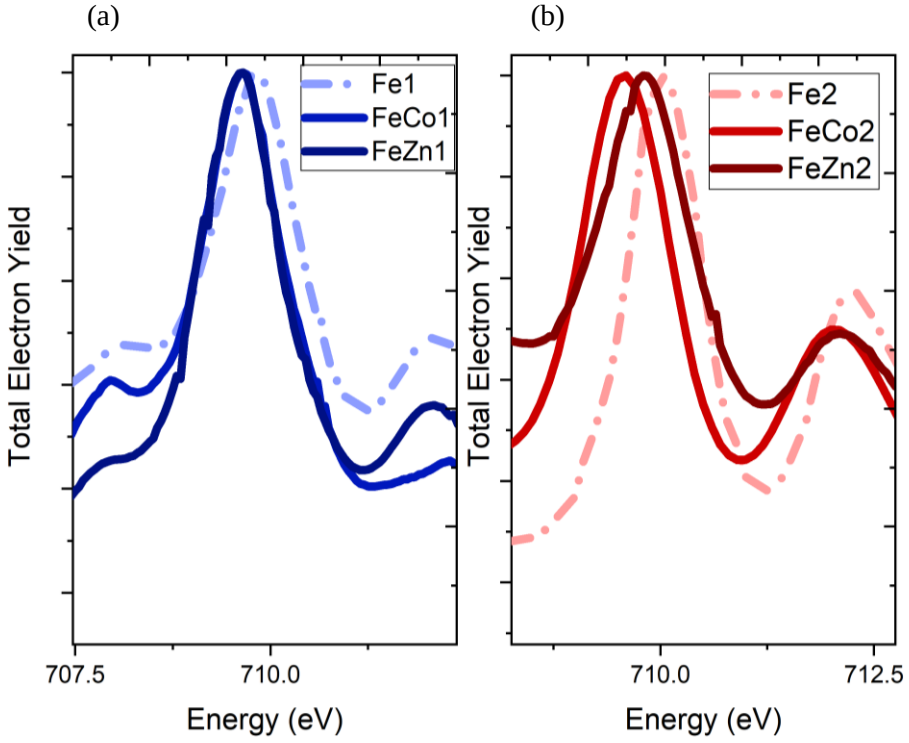

Figure 3.12. (a) Normalized Fe L3-Edge XA spectra of **Fe1**, **FeCo1,** and **FeZn1**. (b) Normalized Fe L3-Edge XA spectra of **Fe2**, **FeCo2,** and **FeZn2**.

The difference might be due to the fact that **Fe2** has more affected cyanide ligands on iron, which stabilizes the e_g level more effectively. No extra feature related to Co is observed in **FeCo** dyads.

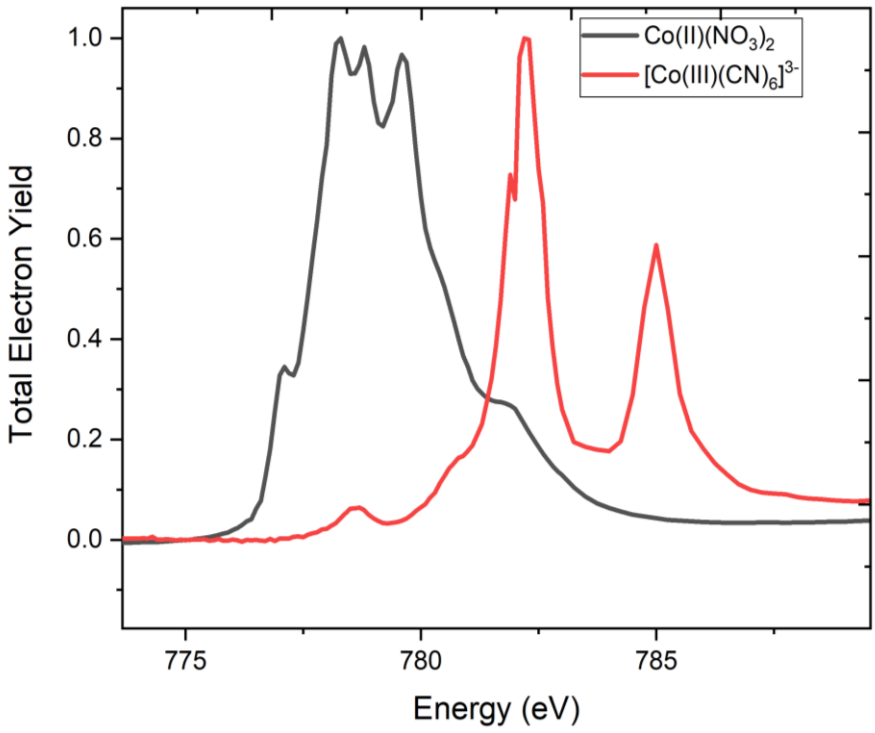

Figure 3.13. Normalized Co L3-Edge XA spectra of $K_3Co(CN)_6$ and $Co(NO_3)_2$.

Co(III) state is known to be low-spin, while it is high-spin for Co(II) sites in PBAs.[81] Thus, for reference, low spin d^6 $K_3Co(CN)_6$ and high spin d^7 $Co(NO_3)_2$ were measured (Figure 3.13). Interestingly, Co L3 edge spectra of both **FeCo** dyads do not match the profile of these references (Figure 3.14-15). However, Co L3-edge spectra of FeCo dyads resemble the profiles of $Co(bpy)Cl_2$and $Co(bpy)_2Cl_2$ precursors.

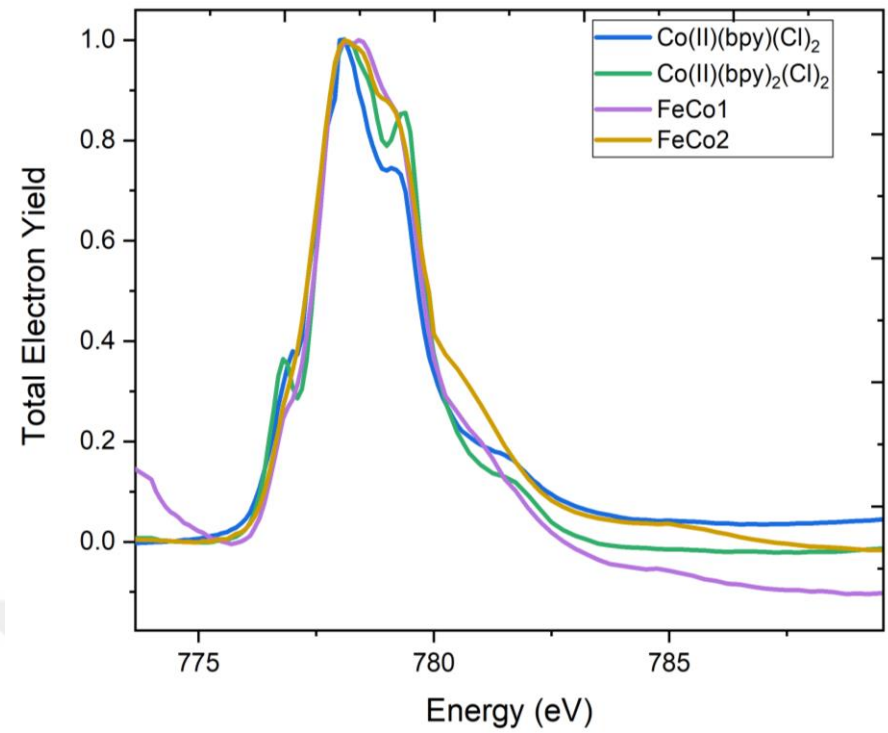

Figure 3.14. Normalized Co L3-Edge XA spectra of $Co(bpy)Cl_2$, $Co(bpy)_2Cl_2$, **FeCo1,** and **FeCo2**.

Although most features are similar, $Co(bpy)_2Cl_2$ shares a double peak feature at around 778 eV with the dyads, which is obtained as a single peak in the precursor. Co-L3 edge spectra reveal that Co sites are in a similar coordination environment as the precursors, which is dominantly a high-spin Co^{2+} species.

3.2.2.5 Electrochemical Studies

We performed electrochemical experiments to evaluate the HOMO and LUMO of the compounds (Figure 3.15). Differential pulse voltammetry (DPV) experiments reveal a reduction at -2.02 V vs Fc for **Fe1**, which is attributed to the bpy reduction ($bpy + 1e^- \rightarrow bpy^{\bullet -}$).[58]

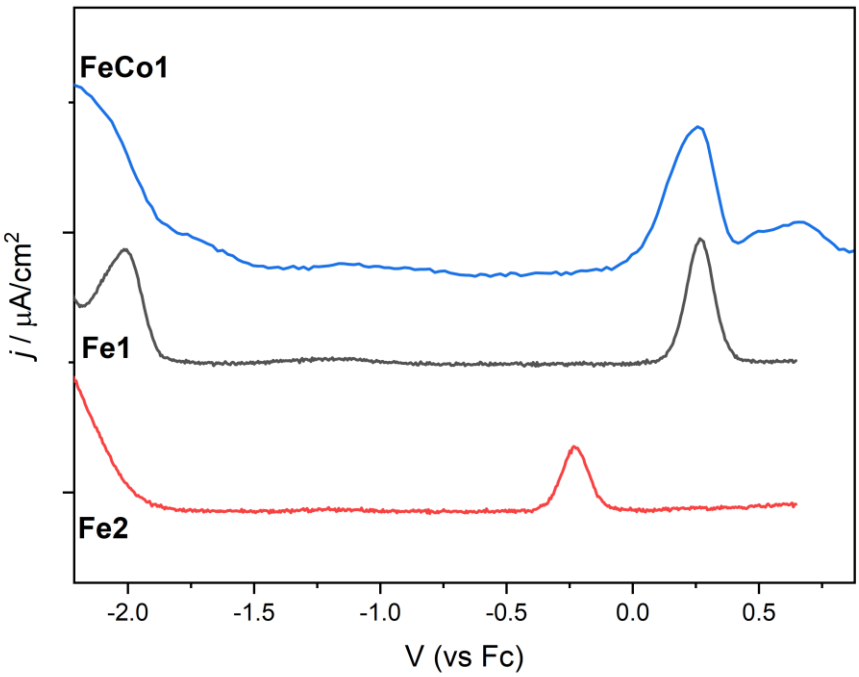

Figure 3.15. DPV experiments with **Fe1**, **Fe2**, and **FeCo1** in 0.1 M TBAP in MeOH.

This reduction peak could not be measured with **Fe2**, suggesting that the reduction of bpy occurs beyond the methanol reduction. The addition of Co(bpy) group to **Fe1** causes the bpy reduction to be overcrowded, thus the exact reduction potential is not seen. Fe(2+/3+) redox potentials of Fe species in methanol are higher than Fe species in acetonitrile in the literature. This is due to stabilization of the t_{2g} level of Fe due to the aforementioned decrease in the e^- density of Fe^{2+}. The addition of Co only decreases the potential to go down from +0.26 V to +0.25 V, which is an insignificant change, and it contradicts the lowered t_{2g} level, as seen by Figures 3.2 (a,b). Co(2+/3+) oxidation is seen to be higher than the Fe(2+/3+) redox, indicating that Co has more of an oxidizing character than Fe.

3.2.3 Photocatalytic Studies

Photocatalytic experiments were performed to compare the oxygen evolution performances of compounds. All experiments were done under neutral conditions (pH 7.0) in a 0.1 M phosphate buffer and 5 mM persulfate solution with 100 mW cm^{-2} Xe light.

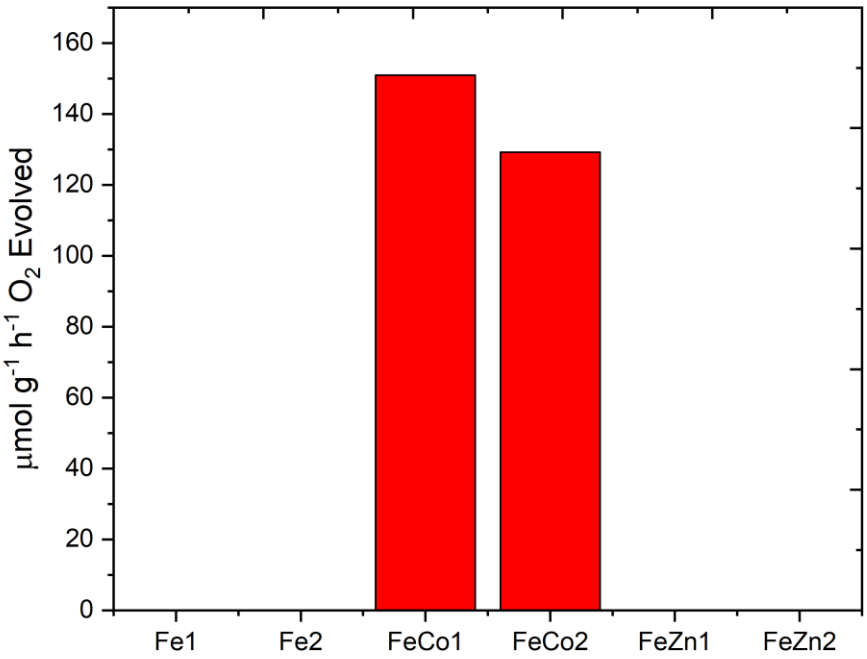

Figure 3.16. Photocatalytic water oxidation experiments with **Fe1, Fe2, FeCo1, FeCo2, FeZn1**, and **FeZn2**.

The first set of experiments is performed with **Fe1**, **Fe2**, **FeCo1**, **FeCo2**, **FeZn1**, **FeZn2**, and regular CoFe Prussian blue analogue (CoFe PBA). Of these, oxygen evolution was obtained only with **FeCo** dyads, suggesting that both Fe and Co sites are required for the photocatalytic process. The performance of **FeCo1** with 50.3 $\mu molg^{-1}h^{-1}$ O_2 evolved is slightly higher than the performance of **FeCo2**(43.1 $\mu molg^{-1}h^{-1}$). The slight difference in the activities of **FeCo1** (50 $\mu mol\ g^{-1}\ h^{-1}$) and **FeCo2** (43 $\mu mol\ g^{-1}\ h^{-1}$) could be attributed to the different solubilities and particle sizes of **FeCo** dyads. **FeCo2** dissolves less, thus the photocatalyst is more heterogeneous with larger particle sizes compared to **FeCo1**. Solubility of PBAs is a known factor in catalyst performance.[84]

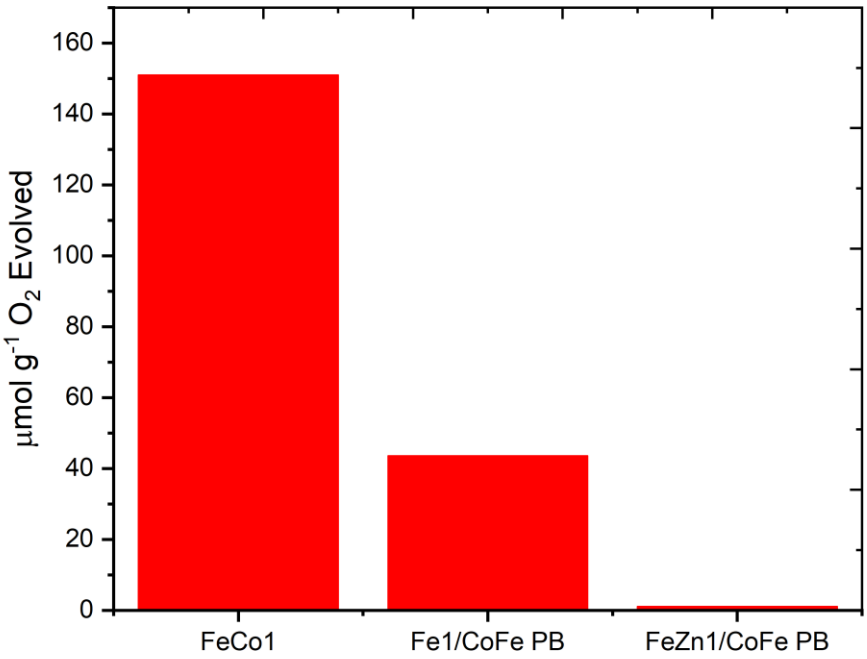

Figure 3.17. Photocatalytic water oxidation experiments with **FeCo1**, **Fe1**/CoFe PB, and **FeZn1**/CoFe PB.

Experiments with physical mixtures of a Co catalyst and a Fe photosensitizer were performed to understand the role of the bridging cyanide group on the photocatalytic activity (Figure 3.17). For this series of control experiments, samples were prepared that have both the Fe photosensitizer and Co catalyst group, but not coupled directly through the bridging cyanide group. CoFe PB was chosen as the catalyst since it is known to be an active water oxidation catalyst in the presence of ruthenium photosensitizers. **Fe1** and **FeZn1** were used as photosensitizers due to their relatively higher solubilities compared to **Fe2** and **FeZn2**. We observed that the CoFePBA/**FeZn1** pair does not reveal any activity, while the CoFePBA/**Fe1** pair exhibits an activity with only around 30% of that observed for **FeCo1**. It is also important to note that **Fe1**/CoFe PBA pair exhibits a much poorer activity compared to **FeCo1** even though it has much higher concentrations of both the catalyst and photosensitizer groups. As can be seen from Figure 3.18, although the TON of Co is similar, the TON of Fe photosensitizer by itself with CoFe PB is really low. Overall, the poor activity observed in systems that do not possess the Fe-CN-Co coordination

mode reveals that the metal-to-metal charge transfer (MMCT) between the catalytic site and the photosensitizer could play an active role in the photocatalytic water oxidation mechanism. To further evaluate the role of the MMCT in the mechanism and photophysics of the photosensitizer, transient absorption studies were performed.

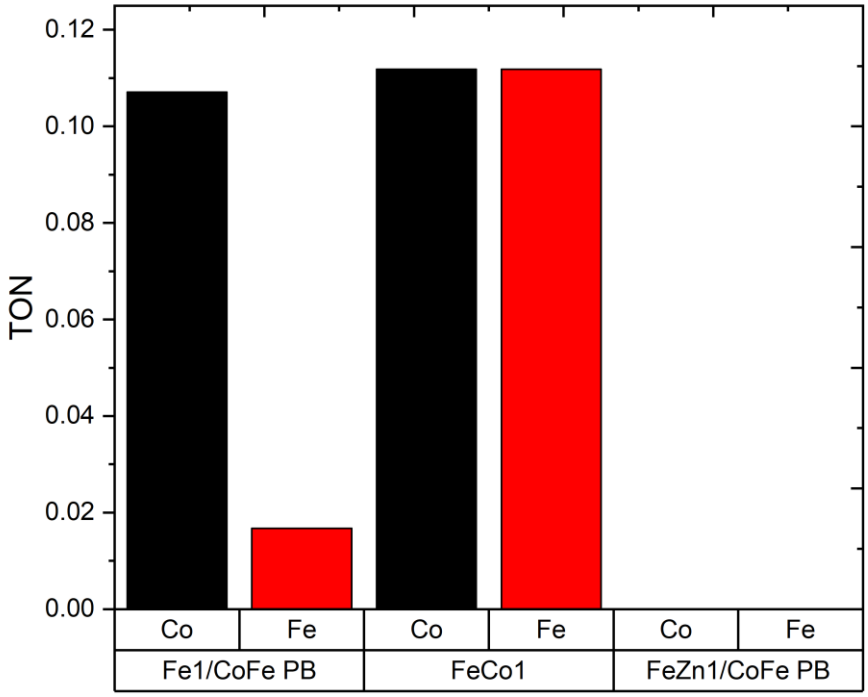

Figure 3.18. Photocatalytic water oxidation experiments with **FeCo1**, **Fe1**/CoFe PB, and **FeZn1**/CoFe PB.

3.2.4 Ultrafast-Transient Absorption Spectroscopy Studies

Femtosecond transient absorption (fs-TA) spectroscopy was employed to elucidate the excited-state dynamics of the dyads. Figures 3.19 (a-c) show the fs-TA spectra of **Fe1**, **FeCo1**, and **FeZn1** in methanol. Following excitation at 570 nm (corresponding to the excitation of the $^{1}A_{1}\rightarrow{}^{1}$MLCT transition), the differential absorption spectrum closely resembles the inverse of the steady-state absorption spectrum and is reminiscent of those reported by Kjaer et al., who used 550 nm excitation to study the excited state dynamics in the parent **Fe1** chromophore.[105] The spectral features were previously assigned to the formation of the ^{5}MC state, which is populated on a

sub-picosecond time scale. Therefore, we conclude that photoexcitation of**Fe1**, **FeCo1**, and **FeZn1** leads to the ultrafast formation of the Fe-centered ^{5}MC state.

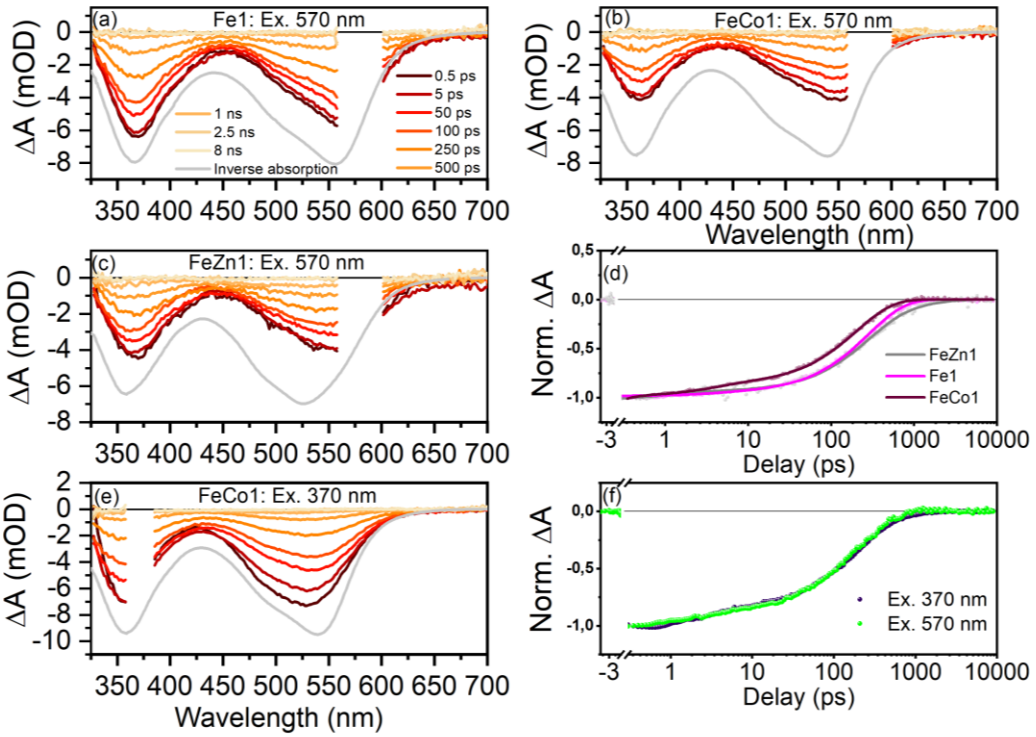

Figure 3.19. (a) TA spectrum of **Fe1** pumped at 570 nm in methanol. (b) TA spectrum of **FeCo1** pumped at 570 nm in methanol. (c) TA spectrum of **FeZn1** pumped at 570 nm in methanol. (d) TA kinetics of **Fe1**, **FeCo1,** and **FeZn1** pumped at 570 nm and probed at 540 nm in methanol. (e) TA spectrum of **FeCo1** pumped at 370 nm in methanol. (f) TA kinetics of **FeCo1** pumped at 370 and 570 nm and probed at 540 nm in methanol.

Despite the similar spectral features, a comparative kinetic analysis of the TA data obtained for **FeCo1** and **Fe1**reveals a significantly faster ground-state recovery for **FeCo1**(Figure 3.19 (d)). Within 50 ps, approximately 34% of the initial ground-state bleach of **FeCo1** recovers, compared to only 20% for **Fe1**, suggesting an additional excited-state quenching pathway is active in **FeCo1**. Since both **Fe1** and **FeCo1** are non-emissive, Förster resonance energy transfer (FRET) between the Fe and Co units can be excluded. Furthermore, Dexter energy transfer from the ^{5}MC (S=2) or MLCT (S=0 or 1) state of the Fe chromophore to the Co^{II} center (S=1/2 or 3/2) seems unlikely due to the conservation of angular momentum. Therefore, following the

rationale presented by McCusker *et al.*, we propose intermolecular reductive electron transfer from the Co^{II} center to the optically excited Fe-chromophore as the mechanism underlying excited-state quenching in **FeCo1**.[106]

To further investigate this hypothesis, we compare the fs-TA dynamics of **FeCo1** and **FeZn1**. The redox-inert Zn^{II} ion cannot participate in light-driven excited-state electron transfer to the Fe center. Nonetheless, coordination of the Zn^{II} or the Co^{II} ion is expected to alter the electron density and hence, the effective ligand field strength of the coordinating CN ligand, in a similar fashion. The IR spectrum of cyanide supports this notion, as both **FeCo1** and **FeZn1** exhibit a blueshift of the cyanide vibration from 2058 cm^{-1} for **Fe1** to 2082 cm^{-1} and 2109 cm^{-1} for **FeCo1** and **FeZn1**, respectively, which indicates similar modifications of the electron density on the CN ligand, through t_{2g} stabilizations and e_g stabilizations seen with UV-Vis and X-Ray Absorption Spectroscopies, respectively.

As for **Fe1**, the TA data of **FeZn1** (Figure 3.19 (c)) resemble the inverse steady-state absorption of the complex. Furthermore, the ground-state recovery rate of **FeZn1** matches that of **Fe1** at early time delays up to about 50 ps. For a more quantitative comparison of ground-state recovery rates, we performed a global analysis of the TA data using a sequential bi-exponential model, as proposed for similar Fe^{II} polypyridyl complexes.[107] For both complexes, a fast process ($\tau_1 \approx 5$ ps) causes only minor spectral changes. We associate this process with vibrational relaxation and cooling within the ^{5}MC state. In addition, a slower process is observed and characterized by a delay-time τ_2 of 400 ps for **FeZn1** and 300 ps for **Fe1**. We associate this process with the decay of the lowest-energy ^{5}MC state (see Figure 3.20 for the species-associated spectra of the hot and cooled ^{5}MC state).[105,107] The comparatively slower ^{5}MC decay in **FeZn1**is attributed to a comparably more stable ^{5}MC state in **FeZn1**. McCusker *et al.* reported previously that a decrease in the ligand field strength (for example, by replacing two cyanide ligands with a 1,10-phenanthroline ligand) reduces zero-point energy differences between the^{5}MC and $^1A_1$ states that lead to slower ground-state recovery ($^5MC \rightarrow {}^1A_1$) of the Fe chromophore.[107] Our work suggests that coordination of a secondary metal ion to the ligand sphere of Fe reduces the effective ligand field of CN, causing relative stabilization of ^{5}MC state, thus offering an alternative approach to ligand field modulation through secondary metal

coordination. This photophysics interpretation is supported by the increased π-back donation, shown by FTIR and UV-Vis, and decreased σ-donation, shown by FTIR and XAS. e_g, through XAS shows more stabilization, around 0.2 eV, than t_{2g} stabilization, around 20 meV, through UV-Vis spectroscopy. Such a case is known to stabilize ^{5}MC too much in comparison to Fe (II) and Ru(II) cyanopolypyridyls.

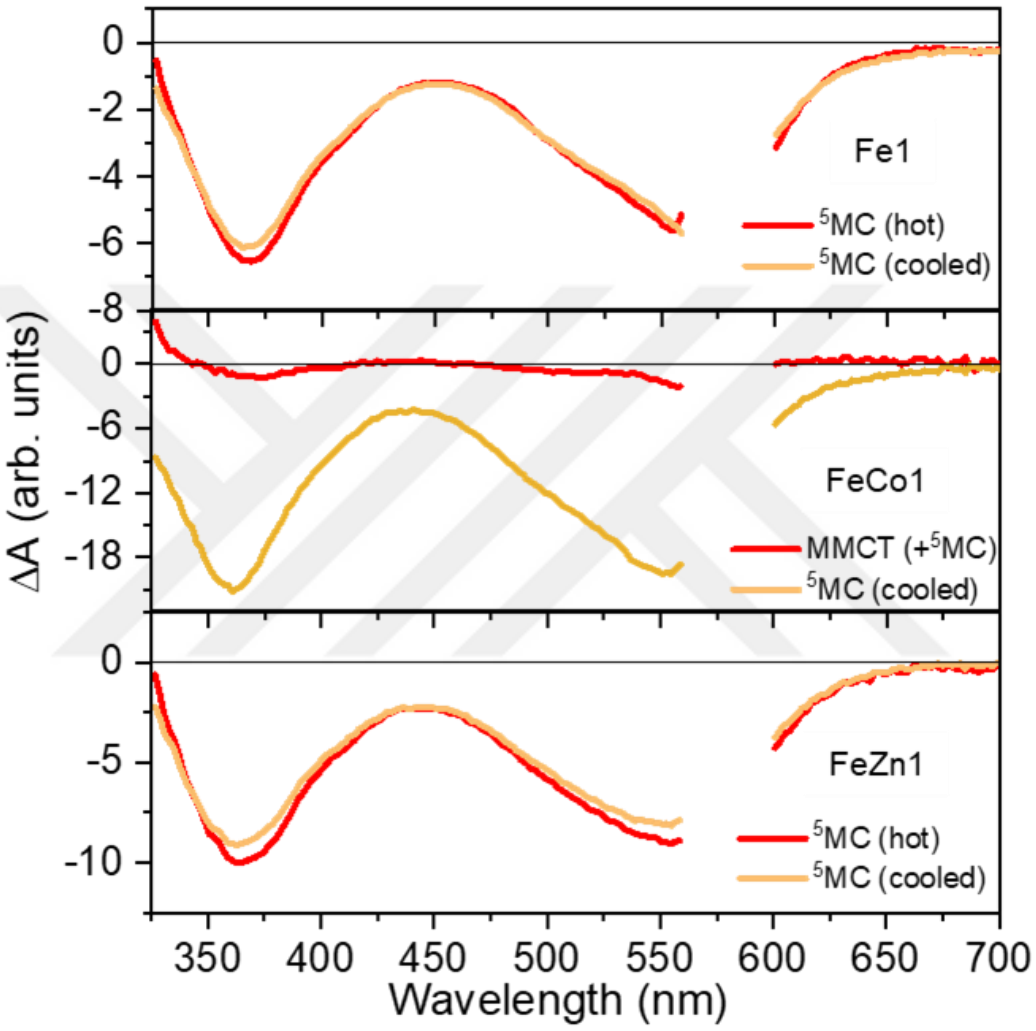

Figure 3.20. Fitting of TA spectra of **Fe1**, **FeCo1,** and **FeZn1** pumped at 570 nm in methanol.

The transient absorption data of **FeCo1** can be fitted by a model considering an intermetallic electron transfer in parallel to the intrinsic relaxation via MC states (as shown in Figure 3.20). We rule out the possibility of a sequential quenching through the ^{5}MC state (e^- transfer from Co(II) to Fe(II) ^{5}MC), as the latter would yield a Fe (I) center, which is unstable in the polar solvent methanol. And ^{5}MC should not have

enough zero-point energy to reduce Fe(II). The reverse case cannot be the case, as yielding Co(I) should result in hydrogen evolution, which was not detected. Fitting the kinetics shown in Figure 3.19(d) to the transient absorption data of **FeCo1** indicates that MLCT excitation populates an MMCT state on a sub-ps timescale in a fraction of the excited dyads, while the remaining excitations populate Fe-centered ^{5}MC states. Whereas the ^{5}MC states are comparatively long-lived (decay to the electronic ground state is estimated to take place in 230 ps), the MMCT state decays with an estimated lifetime of 5 ps. The species-associated spectra (Figure 3.20) reveal that the spectral characteristics of the species associated with the fast and slow decay components of **Fe1** and **FeZn1** are comparably similar. Hence, we identify the underlying states as vibrationally hot and cooled ^{5}MC states, in line with previous reports on similar Fe chromophores.[107] Conversely, the amplitudes of the two species-associated spectra of **FeCo1** differ significantly, indicating different electronic states associated with these two components. For example, the species associated with the faster decay component ($\tau_1 \approx$ 4-5 ps) show very weak and broad non-zero (and positive) absorption at wavelengths above 575 nm (Figure 3.20). Such weak, unstructured photoinduced absorption in this region can be ascribed to the Co(III) state.[85] This is due to thermodynamic oxidation of Co(II) in the Fe(III)-Co(II) excited state, as oxidation potential of Co(2+/3+) is higher than the oxidation potential of Fe(2+/3+). On the other hand, the spectral characteristic of the slower decay component of **FeCo1** resembles the inverse of its steady-state absorption. Herein, we assign the underlying states associated with the fast and slow decay components in **FeCo1** to the MMCT and ^{5}MC states, respectively.

In summary, the analysis of the transient absorption data recorded for **Fe1**, **FeCo1**, and **FeZn1** (Figure 3.19 (d)) indicates that the additional quenching pathway causing faster ground-state recovery in **FeCo1** is absent in **Fe1** and **FeZn1**. The faster quenching of the **FeCo1** makes a strong case in favor of intervalence electron transfer (IVCT) between Co(II) and Fe(III).

Next, transient absorption (TA) measurements were conducted upon 370 nm excitation, resonant with higher-energy MLCT transitions, to test for an influence of excitation energy on the intramolecular charge transfer dynamics. Under these conditions, the transient absorption data are very similar to the one observed upon

570nm excitation (see Figure 3.19 (e)). A comparative kinetic analysis (Figure 3.19 (f)) shows, for instance, identical ground state recovery following excitation at 370 nm and 570 nm, indicating excited **FeCo1** decays following the same mechanism in both cases. This suggests that, irrespective of whether the molecule is excited at higher or lower energy MLCT bands, the system undergoes ultrafast internal conversion (IC) to a common lowest energy MLCT state before branching into MMCT or ^{5}MC. Once the system reaches the lowest MLCT state, the branching ratio is determined by the relative position and coupling of the MMCT/^{5}MC to MLCT states. However, overlapping spectral features of MMCT and ^{5}MC state impede quantitative estimation of the branching ratio.

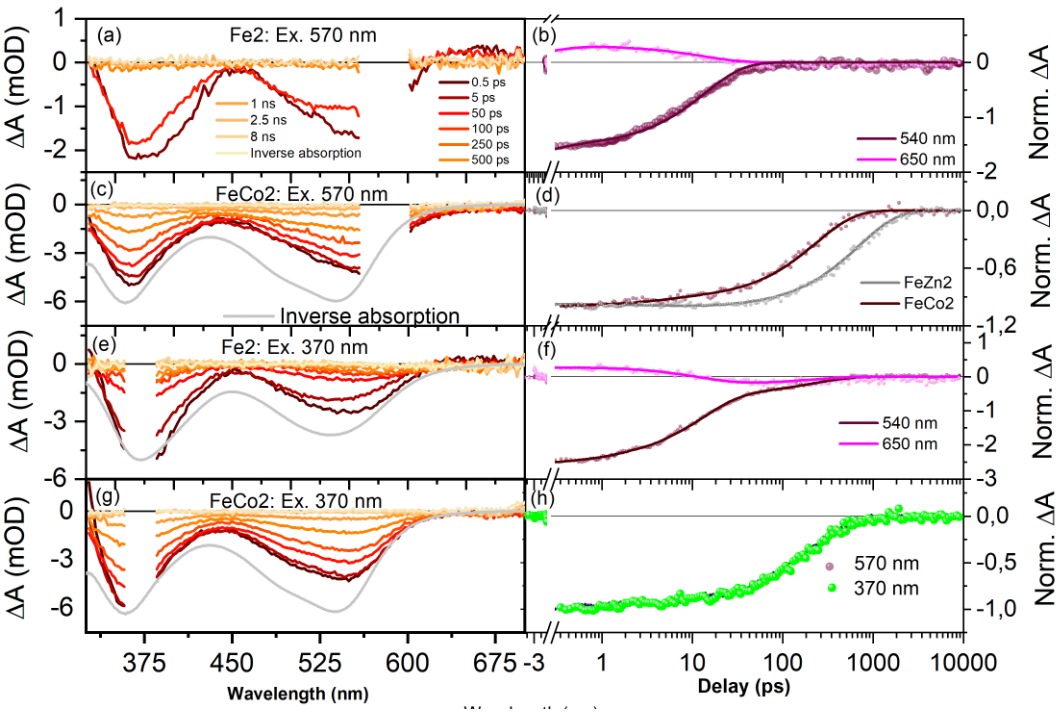

Figure 3.21. (a) TA spectrum of **Fe2** pumped at 570 nm in methanol. (b) TA kinetics of **Fe2** pumped at 570 nm and probed at 540 and 650 nm in methanol. (c) TA spectrum of **FeCo2** pumped at 570 nm in methanol. (d) TA kinetics of **FeCo2** and **FeZn2** pumped at 570 nm and probed at 540 nm in methanol. (e) TA spectrum of **Fe2** pumped at 370 nm in methanol. (f) TA kinetics of **Fe2** pumped at 370 nm and probed at 540 and 650 nm in methanol. (g) TA spectrum of **FeCo2** pumped at 370 nm in methanol. (h) TA kinetics of **FeCo2** pumped at 370 and 570 nm and probed at 540 nm in methanol.

Based on the similarities of the transient absorption spectra and the fact that both **FeCo1** and **FeCo2** show a more rapid excited state decay compared to their **FeZn** counterparts, we conclude that, similar to**FeCo1**, the excited states of**FeCo2** decay via MMCT and ^{5}MC states as shown in Figure 3.21 (d). This is in contrast to the excited-state relaxation in **Fe2**. (Figure 3.21 (a)) Since excitation of **Fe2** at 570 nm populates an MLCT state, which decays via a ^{3}MC state (in contrast to the ^{5}MC state observed for **FeCo2** and **FeZn2**).[94] This is evidenced by the excited-state absorption of **Fe2** at about 650 nm, which decays with a lifetime of 15 ps (Figure 3.21 (b) and 3.21 (e)). Both the spectral feature and lifetime are characteristic of a Fe-centered ^{3}MC state.[94,108] Furthermore, in contrast to the excitation-wavelength independent excited-state dynamics of **FeCo2** and **FeZn2**, **Fe2** shows significantly slower ground-state recovery when excited at 370 nm (in comparison to the excitation at 570 nm) (see Figures 3.21 (a) and 3.21 (e)). Global fitting revealed excitation at 370 nm yields an additional and slow decay component with a characteristic lifetime of 200 ps (Figure 3.21 (f)). This indicates the population of a significantly longer-lived ^{5}MC state upon excitation of higher-lying MLCT states. This is interesting, as one would expect this ^{5}MC population to decay to ^{3}MC due to Kasha's rule, which does not occur. This shows that ^{5}MC is destabilizing the complex to the point that the decay to the ^{3}MC is not favorable, or the reorganization energy is too large. Importantly, no spectral features of the ^{3}MC state were observed for **FeCo2** and **FeZn2**, neither upon excitation at 370 nm nor 570 nm (Figure 3.21 (g) and Figure 3.21 (h)). Instead, ^{5}MC states (spectral signature resembles the inverse of the steady state absorption as shown in Figure 3.21 (c)) are identified as the lowest energy excited state in the dyads. This stabilization of the ^{5}MC state compared to the ^{3}MC state originates in the binding of the secondary metal atom to the coordination sphere of Fe causing a relative stabilization of σ bonded Fe- e_g orbitals (^{5}MC state has 2 e_g electron whereas ^{3}MC has 1 e_g electron) as compared to the t_{2g} orbitals, as the coordination of the Co/Zn shifted e^- density of CN away from Fe center. Compared to other spectroscopic interpretations of **Fe1** based systems, although **Fe2** t_{2g} levels show similar stabilization, eg levels show double the stabilization seen with **Fe1**, 0.2 eV to 0.4 eV. Herein, it is evident from the TA spectra and dynamics discussed above that the coordination of the secondary metal ion (e.g., Fe or Zn) affects the relative stability of MC and MLCT states and influences the excited state photophysics of the dyad. And increasing the number of affected ligands influences the photodynamics

further. Similar excitation-wavelength independent excited-state dynamics were observed for **FeCo2** and **FeZn2** with 370 nm excitations of **FeCo1** and **FeZn1**.

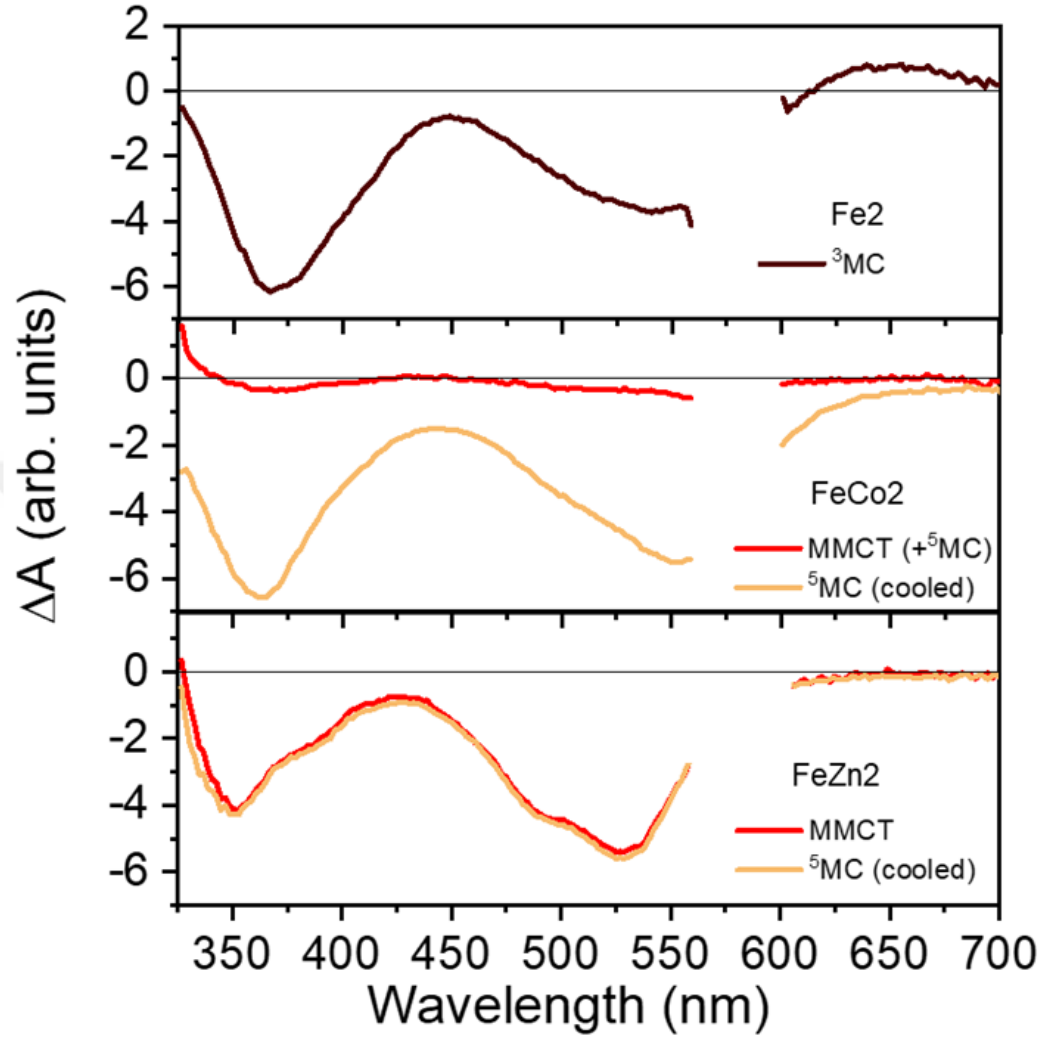

Figure 3.22. Fitting of TA spectra of **Fe2**, **FeCo2,** and **FeZn2** pumped at 570 nm in methanol.

In summary, we observed intermetallic electron transfer from Co(II) to Fe(III)-bpy^{*-} in both the **FeCo1** and **FeCo2** complexes (Figures 3.20 and 3.22). Generation of the MMCT state following the MLCT transition renders the **FeCo** dyads catalytically active for water oxidation, as evidenced by our photocatalytic water oxidation results. Below is a Jablonski diagram that represents the energy levels of ground and excited states according to TAS and other spectroscopic techniques (Figure 3.23).

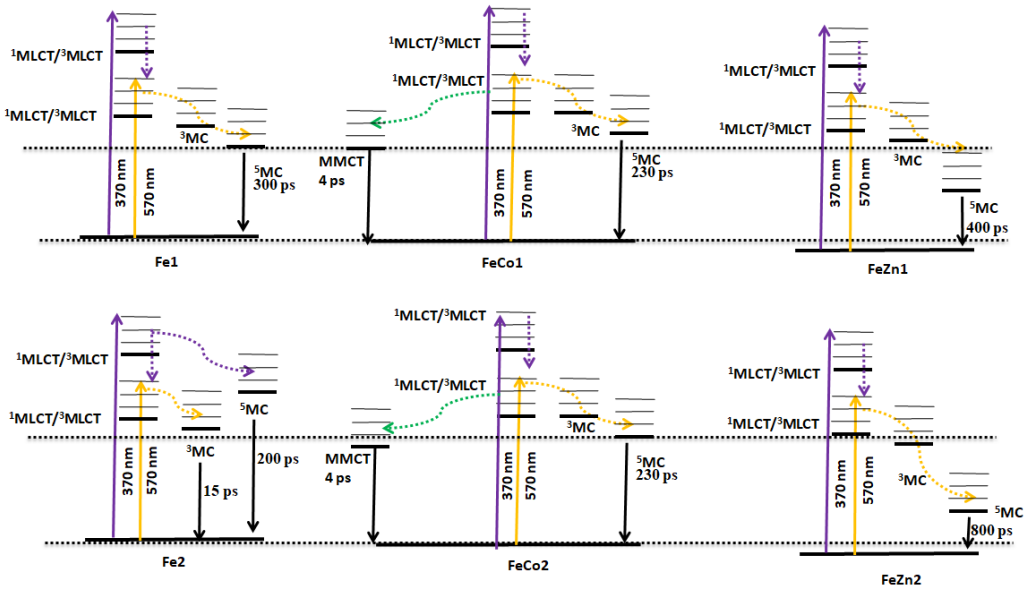

Figure 3.23. Jablonski diagram of **Fe1** and **Fe2** based systems.

CHAPTER 4

4.0 CONCLUSIONS

4.1 Summary

Although significant advances have been achieved in the field of iron chromophores, particularly with carbene-based ligands, their utilization for photocatalytic applications is rather limited due to synthetic challenges. Herein, in this thesis, we provide an easy method to prepare Fe photosensitizer-Co catalyst photocatalytic dyad assemblies, which can be used in the photocatalytic water oxidation process. The classical Prussian blue synthetic methodology has been modified by employing bipyridyl Fe and Co precursors. These novel systems exhibit both metal-to-metal charge transfer (MMCT) and metal-to-metal ligand charge transfer (MLCT) processes. We performed several characterization techniques to elucidate the structure of ligand-modified PBAs, performed a series of photocatalytic studies, and utilized ultrafast transient absorption experiments to establish a structure-property relationship and understand the role of MMCT on the decay dynamics of the MLCT process. We found that σ-donation on Fe is weakened when Co sites are coordinated

to the CN group, leading the stabilization of Fe $e_g$orbitals. Photophysics experiments show, for the first time, that fast-decaying, ~100 fs lifetime, MLCT states can be accessed by closely lying oxidizing metals, such as cobalt. We established Jablonski diagrams for both Fe and FeCo systems and found that MMCT creates an alternative pathway for the relaxation of the excited MLCT state, which is used for the activation of the catalytic site.

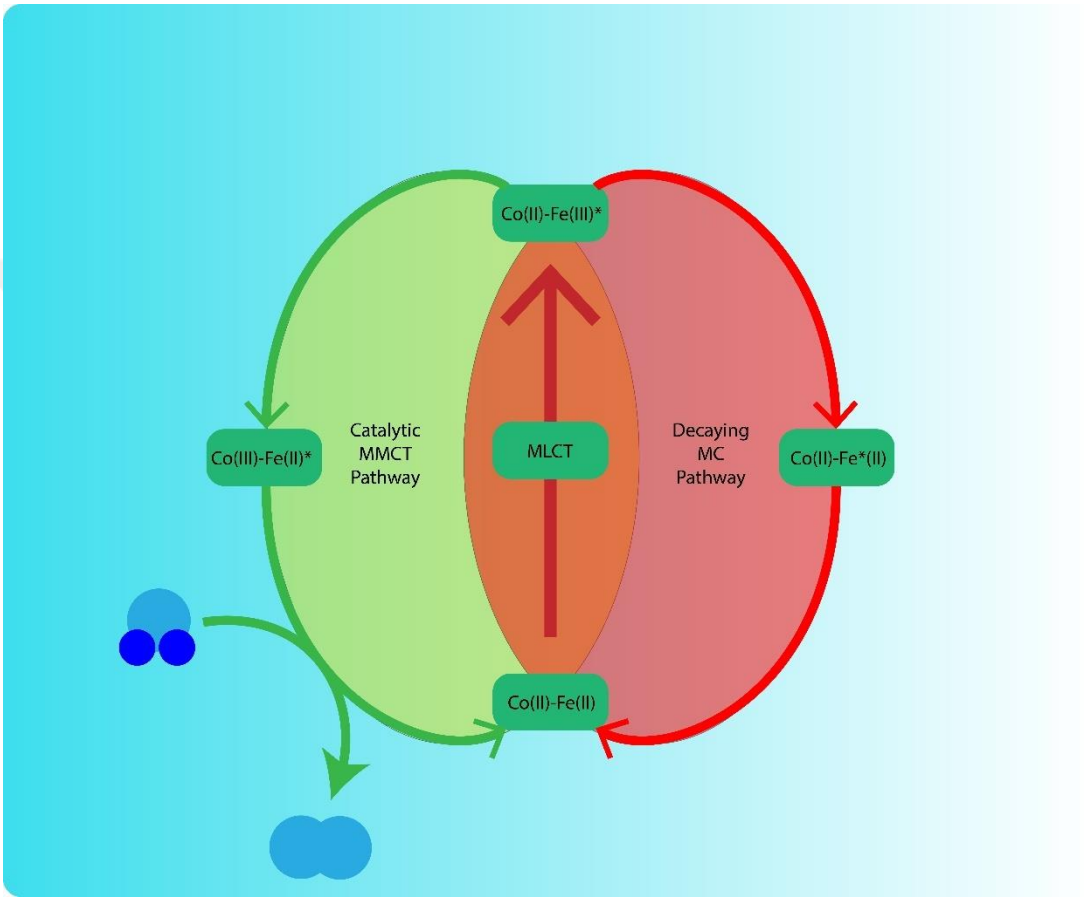

Figure 4.1. Schematic diagram of MLCT excitation of Fe(II) cyanopolypyridyls followed by decay to MMCT and MC states.

Based on these findings, we propose the following photocatalytic mechanism (Figure 4.1). The absorption of light creates an excited MLCT state, which has two possible relaxation pathways: 1) relaxation through the ^{5}MC state to the ground state (GS) and 2) Decay to MMCT state, which oxidizes and, thus, activates the Co site for water oxidation. Therefore, this mechanism could be described as an MMCT-coupled MLCT for the water oxidation process. Overall, this study shows that charge transfer processes could be used to enhance the photocatalytic performance, and cyanide-

based systems provide an ideal platform for such compact designs with several charge transfer processes.

4.2 Remarks

Attaching catalytic metals to Fe(II) polypyridyls through cyanide is shown to be a valid approach. Catalytic performance of such bound species is shown to be higher, as is seen by photocatalytic experiments where extra PBA catalyst was added. For the first time in the literature, a fast-decaying MLCT state is shown to be accessible. However, it is also seen that such a strategy has its drawbacks. Stabilization of e_g, being greater than that of t_{2g} decreases Δ_o and stabilizes ^{5}MC. This is not desirable.

Still, the aimed catalytic dyads have shown interesting properties, such as accessing the MLCT state through MMCT quenching. The usage of cyanide as a linker for such a dyad was done for the first time for Fe-Co systems. The photophysical behaviour of several Fe(II) cyanopolypyridyl systems was explained by the effect of the cyanide on the Fe core. PBA-based photocatalytic dyads are shown to be feasible systems, although their performances are yet to be enhanced to achieve satisfying catalysis.

CHAPTER 5

5.0 BIBLIOGRAPHY

(1) Sinha, N.; Wenger, O. S. Photoactive Metal-to-Ligand Charge Transfer Excited States in 3d6 Complexes with Cr0, MnI, FeII, and CoIII. *J. Am. Chem. Soc.* **2023**, *145* (9), 4903–4920. https://doi.org/10.1021/jacs.2c13432.

(2) Kumagai, H.; Hammarström, L.; Whang, D. R.; Shinohara, Y.; Martinez, J.; Karlsson, J.; Summers, P.; Windle, C. D.; Kodera, M.; Cogdell, R.; Tolod, K. R.; Apaydin, D. H.; Fujita, E.; Kibler, A.; Fan, F.; Gibson, E. A.; Usami, H.; Iwase, A.; Inoue, H.; Kudo, A.; Gust, D.; Domen, K.; Cassiola, F.; Takagi, K.; Kang, S. O.; Yamakata, A.; Li, C.; Sun, L.; Park, H.; Kang, Y. S.; Li, R.; Di Fonzo, F.; Setoyama, T.; Ishitani, O. Inorganic Assembly Catalysts for Artificial Photosynthesis: General Discussion. *Faraday Discuss.* **2017**, *198* (0), 481–507. https://doi.org/10.1039/C7FD90018J.

(3) FUJISHIMA, A.; HONDA, K. Electrochemical Photolysis of Water at a Semiconductor Electrode. *Nature.* **1972**, *238* (5358), 37–38. https://doi.org/10.1038/238037a0.

(4) Aitchison, C. M.; Andrei, V.; Antón-García, D.; Apfel, U.-P.; Badiani, V.; Beller, M.; Bocarsly, A. B.; Bonnet, S.; Brueggeller, P.; Caputo, C. A.; Cassiola, F.; Clausing, S. T.; Cooper, A. I.; Creissen, C. E.; de la Peña O'Shea, V. A.; Domcke, W.; Durrant, J. R.; Grätzel, M.; Hammarström, L.; Hankin, A.; Hatzell, M. C.; Karadas, F.; König, B.; Kuehnel, M. F.; Lamaison, S.; Lin, C.-Y.; Maneiro, M.; Minteer, S. D.; R. Paris, A.; Pastor, E.; Pornrungroj, C.; Reek, J. N. H.; Reisner, E.; Roy, S.; Sahm, C.; Shankar, R.; Shaw, W. J.; Shylin, S. I.; Smith, W. A.; Sokol, K.; Soo, H. Sen; Sprick, R. S.; Viertl, W.; Vogel, A.; Wagner, A.; Wakerley, D.; Wang, Q.; Wielend, D.; Zwijnenburg, M. A. Synthetic Approaches to Artificial Photosynthesis: General Discussion. *Faraday Discuss.* **2019**, *215* (0), 242–281. https://doi.org/10.1039/C9FD90024A.

(5) Förster, C.; Heinze, K. Photophysics and Photochemistry with Earth-Abundant Metals – Fundamentals and Concepts. *Chem. Soc. Rev.* **2020**, *49* (4), 1057–1070. https://doi.org/10.1039/C9CS00573K.

(6) Solak, E. K.; Irmak, E. Advances in Organic Photovoltaic Cells: A Comprehensive Review of Materials, Technologies, and Performance. *RSC Adv.* **2023**, *13* (18), 12244–12269. https://doi.org/10.1039/D3RA01454A.

(7) Chen, S.; Takata, T.; Domen, K. Particulate Photocatalysts for Overall Water Splitting. *Nat Rev Mater.* **2017**, *2* (10), 17050. https://doi.org/10.1038/natrevmats.2017.50.

(8) Abe, R.; Shinmei, K.; Koumura, N.; Hara, K.; Ohtani, B. Visible-Light-Induced Water Splitting Based on Two-Step Photoexcitation between Dye-Sensitized Layered Niobate and Tungsten Oxide Photocatalysts in the Presence of a Triiodide/Iodide Shuttle Redox Mediator. *J. Am. Chem. Soc.* **2013**, *135* (45), 16872–16884. https://doi.org/10.1021/ja4048637.

(9) Lazarides, T.; McCormick, T.; Du, P.; Luo, G.; Lindley, B.; Eisenberg, R. Making Hydrogen from Water Using a Homogeneous System Without Noble Metals. *J. Am. Chem. Soc.* **2009**, *131* (26), 9192–9194. https://doi.org/10.1021/ja903044n.

(10) Yuan, S.; Qin, J.-S.; Xu, H.-Q.; Su, J.; Rossi, D.; Chen, Y.; Zhang, L.; Lollar, C.; Wang, Q.; Jiang, H.-L.; Son, D. H.; Xu, H.; Huang, Z.; Zou, X.; Zhou, H.-C. [Ti8Zr2O12(COO)16] Cluster: An Ideal Inorganic Building Unit for Photoactive Metal–Organic Frameworks. *ACS Cent. Sci.* **2018**, *4* (1), 105–111. https://doi.org/10.1021/acscentsci.7b00497.

(11) Prier, C. K.; Rankic, D. A.; MacMillan, D. W. C. Visible Light Photoredox Catalysis with Transition Metal Complexes: Applications in Organic Synthesis. *Chem. Rev.* **2013**, *113* (7), 5322–5363. https://doi.org/10.1021/cr300503r.

(12) Glaser, F.; Wenger, O. S. Recent Progress in the Development of Transition-Metal Based Photoredox Catalysts. *Coord. Chem. Rev.* **2020**, *405*, 213129. https://doi.org/https://doi.org/10.1016/j.ccr.2019.213129.

(13) Cheung, K. P. S.; Sarkar, S.; Gevorgyan, V. Visible Light-Induced Transition Metal Catalysis. *Chem. Rev.* **2022**, *122* (2), 1543–1625. https://doi.org/10.1021/acs.chemrev.1c00403.

(14) Ahmad, A. A.; Ulusoy Ghobadi, T. G.; Buyuktemiz, M.; Ozbay, E.; Dede, Y.; Karadas, F. Light-Driven Water Oxidation with Ligand-Engineered Prussian Blue Analogues. *Inorg. Chem.* **2022**, *61* (9), 3931–3941. https://doi.org/10.1021/acs.inorgchem.1c03531.

(15) Wang, Q.; Domen, K. Particulate Photocatalysts for Light-Driven Water Splitting: Mechanisms, Challenges, and Design Strategies. *Chem. Rev.* **2020**, *120* (2), 919–985. https://doi.org/10.1021/acs.chemrev.9b00201.

(16) Zhang, F.; Shi, F.; Ma, W.; Gao, F.; Jiao, Y.; Li, H.; Wang, J.; Shan, X.; Lu, X.; Meng, S. Controlling Adsorption Structure of Eosin Y Dye on Nanocrystalline TiO2 Films for Improved Photovoltaic Performances. *J. Phys. Chem. C.* **2013**, *117* (28), 14659–14666. https://doi.org/10.1021/jp404439p.

(17) McCormick, T. M.; Han, Z.; Weinberg, D. J.; Brennessel, W. W.; Holland, P. L.; Eisenberg, R. Impact of Ligand Exchange in Hydrogen Production from Cobaloxime-Containing Photocatalytic Systems. *Inorg. Chem.* **2011**, *50* (21), 10660–10666. https://doi.org/10.1021/ic2010166.

(18) Wang, J.; Liu, Y.; Li, Y.; Xia, L.; Jiang, M.; Wu, P. Highly Efficient Visible-Light-Driven H2 Production via an Eosin Y-Based Metal–Organic Framework. *Inorg. Chem.* **2018**, *57* (13), 7495–7498. https://doi.org/10.1021/acs.inorgchem.8b00718.

(19) Oshima, T.; Nishioka, S.; Kikuchi, Y.; Hirai, S.; Yanagisawa, K.; Eguchi, M.; Miseki, Y.; Yokoi, T.; Yui, T.; Kimoto, K.; Sayama, K.; Ishitani, O.; Mallouk, T. E.; Maeda, K. An Artificial Z-Scheme Constructed from Dye-Sensitized Metal Oxide Nanosheets for Visible Light-Driven Overall Water Splitting. *J. Am. Chem. Soc.* **2020**, *142* (18), 8412–8420. https://doi.org/10.1021/jacs.0c02053.

(20) Akbari, S. S.; Karadaş, F. Investigation of Cyanide-Based Catalysts and Hybrid Assemblies for Artificial Photosynthesis, Turkey, 2022. https://www.proquest.com/dissertations-theses/investigation-cyanide-based-catalysts-hybrid/docview/2734703579/se-2?accountid=8623.

(21) Chalil Oglou, R.; Ulusoy Ghobadi, T. G.; Ozbay, E.; Karadas, F. "Plug and Play" Photosensitizer–Catalyst Dyads for Water Oxidation. *ACS Appl. Mater. Interfaces.* **2022**, *14* (18), 21131–21140. https://doi.org/10.1021/acsami.2c01102.

(22) Bell, J. D.; Murphy, J. A. Recent Advances in Visible Light-Activated Radical Coupling Reactions Triggered by (i) Ruthenium, (Ii) Iridium and (Iii) Organic Photoredox Agents. *Chem. Soc. Rev.* **2021**, *50* (17), 9540–9685. https://doi.org/10.1039/D1CS00311A.

(23) Li, Y.-L.; Li, A.-J.; Huang, S.-L.; Vittal, J. J.; Yang, G.-Y. Polypyridyl Ru(Ii) or Cyclometalated Ir(Iii) Functionalized Architectures for Photocatalysis. *Chem. Soc. Rev.* **2023**, *52* (14), 4725–4754. https://doi.org/10.1039/D3CS00053B.

(24) Abderrazak, Y.; Bhattacharyya, A.; Reiser, O. Visible-Light-Induced Homolysis of Earth-Abundant Metal-Substrate Complexes: A Complementary Activation Strategy in Photoredox Catalysis. *Angew. Chem. Int. Ed.* **2021**, *60* (39), 21100–21115. https://doi.org/https://doi.org/10.1002/anie.202100270.

(25) Wellauer, J.; Ziereisen, F.; Sinha, N.; Prescimone, A.; Velić, A.; Meyer, F.; Wenger, O. S. Iron(III) Carbene Complexes with Tunable Excited State Energies for Photoredox and Upconversion. *J. Am. Chem. Soc.* **2024**, *146* (16), 11299–11318. https://doi.org/10.1021/jacs.4c00605.

(26) Crisenza, G. E. M.; Melchiorre, P. Chemistry Glows Green with Photoredox Catalysis. *Nat. Commun.* **2020**, *11* (1), 803. https://doi.org/10.1038/s41467-019-13887-8.

(27) Pannwitz, A.; Wenger, O. S. Proton-Coupled Multi-Electron Transfer and Its Relevance for Artificial Photosynthesis and Photoredox Catalysis. *Chem. Commun.* **2019**, *55* (28), 4004–4014. https://doi.org/10.1039/C9CC00821G.

(28) Yang, M.; Thompson, D. W.; Meyer, G. J. Charge-Transfer Studies of Iron Cyano Compounds Bound to Nanocrystalline TiO2 Surfaces. *Inorg. Chem.* **2002**, *41* (5), 1254–1262. https://doi.org/10.1021/ic011069q.

(29) Cebrián, C.; Pastore, M.; Monari, A.; Assfeld, X.; Gros, P. C.; Haacke, S. Ultrafast Spectroscopy of Fe(II) Complexes Designed for Solar-Energy Conversion: Current Status and Open Questions. *ChemPhysChem.* **2022**, *23* (7), e202100659. https://doi.org/https://doi.org/10.1002/cphc.202100659.

(30) de Groot, L. H. M.; Ilic, A.; Schwarz, J.; Wärnmark, K. Iron Photoredox Catalysis–Past, Present, and Future. *J. Am. Chem. Soc.* **2023**, *145* (17), 9369–9388. https://doi.org/10.1021/jacs.3c01000.

(31) Alowakennu, M. M.; Ghosh, A.; McCusker, J. K. Direct Evidence for Excited Ligand Field State-Based Oxidative Photoredox Chemistry of a Cobalt(III) Polypyridyl Photosensitizer. *J. Am. Chem. Soc.* **2023**, *145* (38), 20786–20791. https://doi.org/10.1021/jacs.3c09374.

(32) Dierks, P.; Vukadinovic, Y.; Bauer, M. Photoactive Iron Complexes: More Sustainable, but Still a Challenge. *Inorg. Chem. Front.* **2022**, *9* (2), 206–220. https://doi.org/10.1039/D1QI01112J.

(33) Ilic, A.; Schwarz, J.; Johnson, C.; de Groot, L. H. M.; Kaufhold, S.; Lomoth, R.; Wärnmark, K. Photoredox Catalysis via Consecutive 2LMCT- and 3MLCT-Excitation of an Fe(Iii/Ii)–N-Heterocyclic Carbene Complex. *Chem. Sci.* **2022**, *13* (32), 9165–9175. https://doi.org/10.1039/D2SC02122F.

(34) Schmid, L.; Chábera, P.; Rüter, I.; Prescimone, A.; Meyer, F.; Yartsev, A.; Persson, P.; Wenger, O. S. Borylation in the Second Coordination Sphere of FeII Cyanido Complexes and Its Impact on Their Electronic Structures and Excited-State Dynamics. *Inorg. Chem.* **2022**, *61* (40), 15853–15863. https://doi.org/10.1021/acs.inorgchem.2c01667.

(35) Huber-Gedert, M.; Nowakowski, M.; Kertmen, A.; Burkhardt, L.; Lindner, N.; Schoch, R.; Herbst-Irmer, R.; Neuba, A.; Schmitz, L.; Choi, T.-K.; Kubicki, J.; Gawelda, W.; Bauer, M. Fundamental Characterization, Photophysics and Photocatalysis of a Base Metal Iron(II)-Cobalt(III) Dyad. *Chem. Eur. J.* **2021**, *27* (38), 9905–9918. https://doi.org/https://doi.org/10.1002/chem.202100766.

(36) Senthil Murugan, K.; Rajendran, T.; Balakrishnan, G.; Ganesan, M.; Sivasubramanian, V. K.; Sankar, J.; Ilangovan, A.; Ramamurthy, P.; Rajagopal, S. Visible-Light Activation of the Bimetallic Chromophore–Catalyst Dyad: Analysis of Transient Intermediates and Reactivity toward Organic Sulfides. *J. Phys. Chem. A.* **2014**, *118* (25), 4451–4463. https://doi.org/10.1021/jp501084b.

(37) Kaplaneris, N.; Ackermann, L. Earth-Abundant 3d Transition Metals on the Rise in Catalysis. *Beilstein J. Org. Chem.* **2022**, *18*, 86–88. https://doi.org/10.3762/bjoc.18.8.

(38) Zhang, W.; Kjær, K. S.; Alonso-Mori, R.; Bergmann, U.; Chollet, M.; Fredin, L. A.; Hadt, R. G.; Hartsock, R. W.; Harlang, T.; Kroll, T.; Kubiček, K.; Lemke, H. T.; Liang, H. W.; Liu, Y.; Nielsen, M. M.; Persson, P.; Robinson, J. S.; Solomon, E. I.; Sun, Z.; Sokaras, D.; van Driel, T. B.; Weng, T.-C.; Zhu, D.; Wärnmark, K.; Sundström, V.; Gaffney, K. J. Manipulating Charge Transfer Excited State Relaxation and Spin Crossover in Iron Coordination Complexes with Ligand Substitution. *Chem. Sci.* **2017**, *8* (1), 515–523. https://doi.org/10.1039/C6SC03070J.

(39) Wenger, O. S. Photoactive Complexes with Earth-Abundant Metals. *J. Am. Chem. Soc.* **2018**, *140* (42), 13522–13533. https://doi.org/10.1021/jacs.8b08822.

(40) Zhang, W.; Alonso-Mori, R.; Bergmann, U.; Bressler, C.; Chollet, M.; Galler, A.; Gawelda, W.; Hadt, R. G.; Hartsock, R. W.; Kroll, T.; Kjær, K. S.; Kubiek, K.; Lemke, H. T.; Liang, H. W.; Meyer, D. A.; Nielsen, M. M.; Purser, C.; Robinson, J. S.; Solomon, E. I.; Sun, Z.; Sokaras, D.; Van Driel, T. B.; Vankó, G.; Weng, T. C.; Zhu, D.; Gaffney, K. J. Tracking Excited-State Charge and Spin Dynamics in Iron Coordination Complexes. *Nature.* **2014**, *509* (7500), 345–348. https://doi.org/10.1038/nature13252.

(41) Li, Y.-L.; Li, A.-J.; Huang, S.-L.; Vittal, J. J.; Yang, G.-Y. Polypyridyl Ru(Ii) or Cyclometalated Ir(Iii) Functionalized Architectures for Photocatalysis. *Chem. Soc. Rev.* **2023**, *52* (14), 4725–4754. https://doi.org/10.1039/D3CS00053B.

(42) Bell, J. D.; Murphy, J. A. Recent Advances in Visible Light-Activated Radical Coupling Reactions Triggered by (i) Ruthenium, (Ii) Iridium and (Iii) Organic Photoredox Agents. *Chem. Soc. Rev.* **2021**, *50* (17), 9540–9685. https://doi.org/10.1039/D1CS00311A.

(43) Cheung, K. P. S.; Sarkar, S.; Gevorgyan, V. Visible Light-Induced Transition Metal Catalysis. *Chem. Rev.* **2022**, *122* (2), 1543–1625. https://doi.org/10.1021/acs.chemrev.1c00403.

(44) Chan, A. Y.; Ghosh, A.; Yarranton, J. T.; Twilton, J.; Jin, J.; Arias-Rotondo, D. M.; Sakai, H. A.; McCusker, J. K.; MacMillan, D. W. C. Exploiting the Marcus Inverted Region for First-Row Transition Metal–Based Photoredox Catalysis. *Science.* **2023**, *382* (6667), 191–197. https://doi.org/10.1126/science.adj0612.

(45) Kaplaneris, N.; Ackermann, L. Earth-Abundant 3d Transition Metals on the Rise in Catalysis. *Beilstein J. Org. Chem.* **2022**, *18*, 86–88. https://doi.org/10.3762/bjoc.18.8.

(46) de Groot, L. H. M.; Ilic, A.; Schwarz, J.; Wärnmark, K. Iron Photoredox Catalysis–Past, Present, and Future. *J. Am. Chem. Soc.* **2023**, *145* (17), 9369–9388. https://doi.org/10.1021/jacs.3c01000.

(47) Dierks, P.; Vukadinovic, Y.; Bauer, M. Photoactive Iron Complexes: More Sustainable, but Still a Challenge. *Inorg. Chem. Front.* **2022**, *9* (2), 206–220. https://doi.org/10.1039/D1QI01112J.

(48) Kasper S. Kjær; Wenkai Zhang; Roberto Alonso-Mori; Uwe Bergmann; Matthieu Chollet; Ryan G. Hadt; Robert W. Hartsock; Tobias Harlang; Thomas Kroll; Katharina Kubiček; Henrik T. Lemke; Huiyang W. Liang; Yizhu Liu;Martin M. Nielsen; Joseph S. Robinson; Edward I. Solomon; Dimosthenis Sokaras; Tim B. van Driel; Tsu Chien Weng; Diling Zhu; Petter Persson; Kenneth Wärnmark; Villy Sundström; Kelly J. Gaffney. Ligand Manipulation of Charge Transfer Excited State Relaxation and Spin Crossover in [Fe(2,2'-Bipyridine)2(CN)2]. *Struct. Dyn.* **2017**, *4* (4). https://doi.org/10.1063/1.4985017.

(49) Winkler, J. R.; Creutz, C.; Sutin, N. Solvent Tuning of the Excited-State Properties of (2,2′-Bipyridine)Tetracyanoferrate(II): Direct Observation of a Metal-to-Ligand Charge-Transfer Excited State of Iron(II). *J. Am. Chem. Soc.* **1987**, *109* (11), 3470–3471. https://doi.org/10.1021/ja00245a053.

(50) Ashley, D. C.; Jakubikova, E. Ironing out the Photochemical and Spin-Crossover Behavior of Fe(II) Coordination Compounds with Computational Chemistry. *Coord. Chem. Rev.* **2017**, *337*, 97–111. https://doi.org/10.1016/j.ccr.2017.02.005.

(51) Chábera, P.; Fredin, L. A.; Kjær, K. S.; Rosemann, N. W.; Lindh, L.; Prakash, O.; Liu, Y.; Wärnmark, K.; Uhlig, J.; Sundström, V.; Yartsev, A.; Persson, P. Band-Selective Dynamics in Charge-Transfer Excited Iron Carbene Complexes. *Faraday Discuss.* **2019**, *216*, 191–210. https://doi.org/10.1039/c8fd00232k.

(52) Auböck, G.; Chergui, M. Sub-50-Fs Photoinduced Spin Crossover in [Fe(Bpy)3]2+. *Nat. Chem.* **2015**, *7* (8), 629–633. https://doi.org/10.1038/nchem.2305.

(53) Nance, J.; Bowman, D. N.; Mukherjee, S.; Kelley, C. T.; Jakubikova, E. Insights into the Spin-State Transitions in [Fe(Tpy)2]2+: Importance of the Terpyridine Rocking Motion. *Inorg. Chem.* **2015**, *54* (23), 11259–11268. https://doi.org/10.1021/acs.inorgchem.5b01747.

(54) Gawelda, W.; Cannizzo, A.; Pham, V. T.; Van Mourik, F.; Bressler, C.; Chergui, M. Ultrafast Nonadiabatic Dynamics of [FeII(Bpy)3] 2+ in Solution.

J. Am. Chem. Soc. **2007**, *129* (26), 8199–8206. https://doi.org/10.1021/ja070454x.

(55) Vittardi, S. B.; Magar, R. T.; Schrage, B. R.; Ziegler, C. J.; Jakubikova, E.; Rack, J. J. Evidence for a Lowest Energy 3 MLCT Excited State in [Fe(Tpy)(CN) 3] -. *Chem. Comm.* **2021**, *57* (38), 4658–4661. https://doi.org/10.1039/D1CC01090E.

(56) Yang, M.; Thompson, D. W.; Meyer, G. J. Dual Pathways for TiO 2 Sensitization by Na2[Fe(Bpy(CN)4]. *Inorg. Chem.* **2000**, *39* (17), 3738–3739. https://doi.org/10.1021/ic000415l.

(57) Zhang, W.; Kjær, K. S.; Alonso-Mori, R.; Bergmann, U.; Chollet, M.; Fredin, L. A.; Hadt, R. G.; Hartsock, R. W.; Harlang, T.; Kroll, T.; Kubiček, K.; Lemke, H. T.; Liang, H. W.; Liu, Y.; Nielsen, M. M.; Persson, P.; Robinson, J. S.; Solomon, E. I.; Sun, Z.; Sokaras, D.; Van Driel, T. B.; Weng, T. C.; Zhu, D.; Wärnmark, K.; Sundström, V.; Gaffney, K. J. Manipulating Charge Transfer Excited State Relaxation and Spin Crossover in Iron Coordination Complexes with Ligand Substitution. *Chem. Sci.* **2016**, *8* (1), 515–523. https://doi.org/10.1039/C6SC03070J.

(58) Schmid, L.; Chábera, P.; Rüter, I.; Prescimone, A.; Meyer, F.; Yartsev, A.; Persson, P.; Wenger, O. S. Borylation in the Second Coordination Sphere of FeIICyanido Complexes and Its Impact on Their Electronic Structures and Excited-State Dynamics. *Inorg. Chem.* **2022**, *61* (40), 15853–15863. https://doi.org/10.1021/acs.inorgchem.2c01667.

(59) Schmidt, H.; Oglou, R. C.; Tunçer, H. O.; Ghobadi, T. G. U.; Tekir, Ş.; Sertcelik, K. N. O.; Ibrahim, A.; Döhler, L.; Özçubukçu, S.; Kupfer, S.; Dietzek-Ivanšić, B.; Karadaş, F. A Heterodox Approach for Designing Iron Photosensitizers: Pentacyanoferrate(II) Complexes with Monodentate Bipyridinium/Pyrazinium-Based Acceptor Ligands. *Inorg. Chem.* **2025**, *64* (14), 7079–7087. https://doi.org/10.1021/acs.inorgchem.5c00412.

(60) Liu, Y.; Persson, P.; Sundström, V.; Wärnmark, K. Fe N-Heterocyclic Carbene Complexes as Promising Photosensitizers. *Acc. Chem. Res.* **2016**, *49* (8), 1477–1485. https://doi.org/10.1021/acs.accounts.6b00186.

(61) Zimmer, P.; Burkhardt, L.; Friedrich, A.; Steube, J.; Neuba, A.; Schepper, R.; Müller, P.; Flörke, U.; Huber, M.; Lochbrunner, S.; Bauer, M. The Connection between NHC Ligand Count and Photophysical Properties in Fe(II)

Photosensitizers: An Experimental Study. *Inorg. Chem.* **2018**, *57* (1), 360–373. https://doi.org/10.1021/acs.inorgchem.7b02624.

(62) Fredin, L. A.; Wärnmark, K.; Sundström, V.; Persson, P. Molecular and Interfacial Calculations of Iron(II) Light Harvesters. *ChemSusChem.* **2016**, *9* (7), 667–675. https://doi.org/10.1002/cssc.201600062.

(63) Kjær, K. S.; Styring, S.; Persson, P.; Honarfar, A.; Uhlig, J.; Ericsson, T.; Bendix, J.; Bergquist, K.-E.; Wärnmark, K.; Prakash, O.; Yartsev, A.; Rosemann, N. W.; Gordivska, O.; Chábera, P.; Strand, D.; Lindh, L.; Kaul, N.; Lomoth, R.; Fredin, L. A.; Häggström, L.; Huang, P.; Sundström, V. Luminescence and Reactivity of a Charge-Transfer Excited Iron Complex with Nanosecond Lifetime. *Science.* **2018**, *363* (January), 249–253. https://doi.org/10.1126/science.aau7160.

(64) Wenger, O. S. Is Iron the New Ruthenium? *Chem. Eur. J.* **2019**, *25*, 6043–6052. https://doi.org/10.1002/chem.201806148.

(65) Pápai, M.; Abedi, M.; Levi, G.; Biasin, E.; Nielsen, M. M.; Møller, K. B. Theoretical Evidence of Solvent-Mediated Excited-State Dynamics in a Functionalized Iron Sensitizer. *J. Phys. Chem. C.* **2019**, *123* (4), 2056–2065. https://doi.org/10.1021/acs.jpcc.8b10768.

(66) Liu, Y.; Harlang, T. C. B.; Canton, S. E.; Chábera, P.; Suárez-Alcántara, K.; Fleckhaus, A.; Vithanage, D. A.; Göransson, E.; Corani, A.; Lomoth, R.; Sundström, V.; Wärnmark, K. Towards Longer-Lived Metal-to-Ligand Charge Transfer States of Iron(Ii) Complexes: An N-Heterocyclic Carbene Approach. *Chem. Comm.* **2013**, *49* (57), 6412–6414. https://doi.org/10.1039/c3cc43833c.

(67) Duchanois, T.; Etienne, T.; Cebrián, C.; Liu, L.; Monari, A.; Beley, M.; Assfeld, X.; Haacke, S.; Gros, P. C. An Iron-Based Photosensitizer with Extended Excited-State Lifetime: Photophysical and Photovoltaic Properties. *Eur. J. Inorg. Chem.* **2015**, *2015* (14), 2469–2477. https://doi.org/10.1002/ejic.201500142.

(68) Sinha, N.; Wenger, O. S. Photoactive Metal-to-Ligand Charge Transfer Excited States in 3d 6 Complexes with Cr 0 , Mn. https://doi.org/10.1021/jacs.2c13432.

(69) Liu, Y.; Persson, P.; Sundström, V.; Wärnmark, K. Fe N-Heterocyclic Carbene Complexes as Promising Photosensitizers. *Acc. Chem. Res.* **2016**, *49* (8), 1477–1485. https://doi.org/10.1021/acs.accounts.6b00186.

(70) Glaser, F.; Wenger, O. S. Recent Progress in the Development of Transition-Metal Based Photoredox Catalysts. *Coord. Chem. Rev.* **2020**, *405*, 213129. https://doi.org/10.1016/j.ccr.2019.213129.

(71) Lindh, L.; Chábera, P.; Rosemann, N. W.; Uhlig, J.; Wärnmark, K.; Yartsev, A.; Sundström, V.; Persson, P. Photophysics and Photochemistry of Iron Carbene Complexes for Solar Energy Conversion and Photocatalysis. *Catalysts.* **2020**, *10* (3). https://doi.org/10.3390/catal10030315.

(72) Liu, Y.; Persson, P.; Sundström, V.; Wärnmark, K. Fe N-Heterocyclic Carbene Complexes as Promising Photosensitizers. *Acc. Chem. Res.* **2016**, *49* (8), 1477–1485. https://doi.org/10.1021/acs.accounts.6b00186.

(73) Leis, W.; Argüello Cordero, M. A.; Lochbrunner, S.; Schubert, H.; Berkefeld, A. A Photoreactive Iron(II) Complex Luminophore. *J. Am. Chem. Soc.* **2022**, *144* (3), 1169–1173. https://doi.org/10.1021/jacs.1c13083.

(74) Chábera, P.; Kjær, K. S.; Prakash, O.; Honarfar, A.; Liu, Y.; Fredin, L. A.; Harlang, T. C. B.; Lidin, S.; Uhlig, J.; Sundström, V.; Lomoth, R.; Persson, P.; Wärnmark, K. FeII Hexa N-Heterocyclic Carbene Complex with a 528 Ps Metal-To-Ligand Charge-Transfer Excited-State Lifetime. *J. Phys. Chem Lett.* **2018**, *9* (3), 459–463. https://doi.org/10.1021/acs.jpclett.7b02962.

(75) Ortiz, R. J.; Mondal, R.; McCusker, J. K.; Herbert, D. E. Leveraging Intramolecular π-Stacking to Access an Exceptionally Long-Lived 3MC Excited State in an Fe(II) Carbene Complex. *J. Am. Chem. Soc.* **2025**, *147* (2), 1694–1708. https://doi.org/10.1021/jacs.4c12650.

(76) Arias-Rotondo, D. M.; McCusker, J. K. The Photophysics of Photoredox Catalysis: A Roadmap for Catalyst Design. *Chem. Soc. Rev.* **2016**, *45* (21), 5803–5820. https://doi.org/10.1039/C6CS00526H.

(77) Huber-Gedert, M.; Nowakowski, M.; Kertmen, A.; Burkhardt, L.; Lindner, N.; Schoch, R.; Herbst-Irmer, R.; Neuba, A.; Schmitz, L.; Choi, T.-K.; Kubicki, J.; Gawelda, W.; Bauer, M. Fundamental Characterization, Photophysics and Photocatalysis of a Base Metal Iron(II)-Cobalt(III) Dyad. *Chem. Eur. J.* **2021**, *27* (38), 9905–9918. https://doi.org/https://doi.org/10.1002/chem.202100766.

(78) Woodhouse, M. D.; McCusker, J. K. Mechanistic Origin of Photoredox Catalysis Involving Iron(II) Polypyridyl Chromophores. *J. Am. Chem. Soc.* **2020**, *142* (38), 16229–16233. https://doi.org/10.1021/jacs.0c08389.

(79) Arifin, K.; Majlan, E. H.; Wan Daud, W. R.; Kassim, M. B. Bimetallic Complexes in Artificial Photosynthesis for Hydrogen Production: A Review. *Int. J. Hydrogen Energy*. **2012**, *37* (4), 3066–3087. https://doi.org/https://doi.org/10.1016/j.ijhydene.2011.11.052.

(80) Kamioka, H.; Moritomo, Y.; Kosaka, W.; Ohkoshi, S. Dynamics of Charge-Transfer Pairs in the Cyano-Bridged Co(2+)-Fe(3+) Transition-Metal Compound. *Phys. Rev. B.* **2008**, *77* (18), 180301. https://doi.org/10.1103/PhysRevB.77.180301.

(81) Shatruk, M.; Avendano, C.; Dunbar, K. R. Cyanide-Bridged Complexes of Transition Metals: A Molecular Magnetism Perspective. In *Prog. Inorg. Chem.*; Progress in Inorganic Chemistry; 2009; pp 155–334. https://doi.org/https://doi.org/10.1002/9780470440124.ch3.

(82) Alsaç, E. P.; Ülker, E.; Nune, S. V. K.; Dede, Y.; Karadas, F. Tuning the Electronic Properties of Prussian Blue Analogues for Efficient Water Oxidation Electrocatalysis: Experimental and Computational Studies. *Chem. Eur. J.* **2018**, *24* (19), 4856–4863. https://doi.org/https://doi.org/10.1002/chem.201704933.

(83) Chalil Oglou, R.; Ulusoy Ghobadi, T. G.; Ozbay, E.; Karadas, F. "Plug and Play" Photosensitizer–Catalyst Dyads for Water Oxidation. *ACS Appl. Mater. Interfaces.* **2022**, *14* (18), 21131–21140. https://doi.org/10.1021/acsami.2c01102.

(84) Seki, Y.; Nakazono, T.; Yamada, Y. Size and Shape Effect of Countercations on Depolymerization and Water Oxidation Catalysis of Cyano-Bridged Coordination Polymers. *Inorg. Chem.* **2025**, *64* (11), 5354–5359. https://doi.org/10.1021/acs.inorgchem.4c05491.

(85) Kamioka, H.; Moritomo, Y.; Kosaka, W.; Ohkoshi, S. Dynamics of Charge-Transfer Pairs in the Cyano-Bridged Co(2+)-Fe(3+) Transition-Metal Compound. *Phys. Rev. B.* **2008**, *77* (18), 180301. https://doi.org/10.1103/PhysRevB.77.180301.

(86) Aksoy, M.; Nune, S. V. K.; Karadas, F. A Novel Synthetic Route for the Preparation of an Amorphous Co/Fe Prussian Blue Coordination Compound

with High Electrocatalytic Water Oxidation Activity. *Inorg. Chem.* **2016**, *55* (9), 4301–4307. https://doi.org/10.1021/acs.inorgchem.6b00032.

(87) Ulusoy Ghobadi, T. G.; Ozbay, E.; Karadas, F. How to Build Prussian Blue Based Water Oxidation Catalytic Assemblies: Common Trends and Strategies. *Chem. Eur. J.* **2021**, *27* (11), 3638–3649. https://doi.org/10.1002/chem.202004091.

(88) Ulusoy Ghobadi, T. G.; Ghobadi, A.; Buyuktemiz, M.; Akhuseyin Yildiz, E.; Yildiz, D. B.; Yaglioglu, H. G.; Dede, Y.; Ozbay, E.; Karadas, F. A Robust Precious Metal-Free Dye-Sensitized Photoanode for Water Oxidation: Nanosecond Long Excited State Lifetime via a Prussian Blue Analogue. *Angew. Chem. Int. Ed.* **2020**, *59* (10), 4082–4090. https://doi.org/10.1002/anie.201914743.

(89) Schilt, A. A. Mixed Ligand Complexes of Iron(II) and (III) with Cyanide and Aromatic Di-Imines. *J. Am. Chem. Soc.* **1960**, *82* (12), 3000–3005. https://doi.org/10.1021/ja01497a007.

(90) Su, C.-C.; Huang, S.-M. The Formation of Cobalt(II) Halide Complexes Containing Neutral Bidentate Ligands. *Transit. Met. Chem.* **1984**, *9* (6), 220–224. https://doi.org/10.1007/BF01227124.

(91) Witas, K.; Nair, S. S.; Maisuradze, T.; Zedler, L.; Schmidt, H.; Garcia-Porta, P.; Rein, A. S. J.; Bolter, T.; Rau, S.; Kupfer, S.; Dietzek-Ivanšić, B.; Sorsche, D. U. Beyond the First Coordination Sphere─Manipulating the Excited-State Landscape in Iron(II) Chromophores with Protons. *J. Am. Chem. Soc.* **2024**, *146* (29), 19710–19719. https://doi.org/10.1021/jacs.4c00552.

(92) Schilt, A. A. Mixed Ligand Complexes of Iron(II) and (III) with Cyanide and Aromatic Di-Imines. *J. Am. Chem. Soc.* **1960**, *82* (12), 3000–3005. https://doi.org/10.1021/ja01497a007.

(93) Schmid, L.; Chábera, P.; Rüter, I.; Prescimone, A.; Meyer, F.; Yartsev, A.; Persson, P.; Wenger, O. S. Borylation in the Second Coordination Sphere of FeII Cyanido Complexes and Its Impact on Their Electronic Structures and Excited-State Dynamics. *Inorg. Chem.* **2022**, *61* (40), 15853–15863. https://doi.org/10.1021/acs.inorgchem.2c01667.

(94) Kjær, K. S.; Kunnus, K.; Harlang, T. C. B.; Van Driel, T. B.; Ledbetter, K.; Hartsock, R. W.; Reinhard, M. E.; Koroidov, S.; Li, L.; Laursen, M. G.; Biasin, E.; Hansen, F. B.; Vester, P.; Christensen, M.; Haldrup, K.; Nielsen,

M. M.; Chabera, P.; Liu, Y.; Tatsuno, H.; Timm, C.; Uhlig, J.; Sundström, V.; Németh, Z.; Szemes, D. S.; Bajnóczi, É.; Vankó, G.; Alonso-Mori, R.; Glownia, J. M.; Nelson, S.; Sikorski, M.; Sokaras, D.; Lemke, H. T.; Canton, S. E.; Wärnmark, K.; Persson, P.; Cordones, A. A.; Gaffney, K. J. Solvent Control of Charge Transfer Excited State Relaxation Pathways in [Fe(2,2′-Bipyridine)(CN)4]2−. *Phys. Chem. Chem. Phys.* **2018**, *20* (6), 4238–4249. https://doi.org/10.1039/C7CP07838B.

(95) Yang, M.; Thompson, D. W.; Meyer, G. J. Charge-Transfer Studies of Iron Cyano Compounds Bound to Nanocrystalline TiO2 Surfaces. *Inorg. Chem.* **2002**, *41* (5), 1254–1262. https://doi.org/10.1021/ic011069q.

(96) Yatsimirskii, K. B.; Nemoshkalenko, V. V.; Nazarenko, Y. P.; Aleshin, V. G.; Zhilinskaya, V. V.; Tomashevsky, N. A. Use of X-Ray Photoelectron and Mössbauer Spectroscopies in the Study of Iron Pentacyanide Complexes. *J. Electron Spectros. Relat. Phenom.* **1977**, *10* (3), 239–245. https://doi.org/10.1016/0368-2048(77)85023-8.

(97) Cui, X.; Hong, L.; Lin, X. Electrochemical Preparation, Characterization and Application of Electrodes Modified with Hybrid Hexacyanoferrates of Copper and Cobalt. *J. Electroanal. Chem.* **2002**, *526* (1–2), 115–124. https://doi.org/10.1016/S0022-0728(02)00724-6.

(98) Oku, M. Kinetics of Photoreduction of Fe(III) in Solid Solution K3(Fe,M)(CN)6 (Where M Is Cr, Co) during XPS Measurement. *J. Electron Spectros. Relat. Phenom.* **1994**, *67* (3), 401–407. https://doi.org/10.1016/0368-2048(93)02044-M.

(99) Briggs, D.; Gibson, V. A. Direct Observation of Multiplet Splitting in 2P Photoelectron Peaks of Cobalt Complexes. *Chem. Phys. Lett.* **1974**, *25* (4), 493–496. https://doi.org/10.1016/0009-2614(74)85350-9.

(100) Atzei, D.; Rossi, A.; Sadun, C. Synthesis and Characterization of a Cobalt(III) Complex with 1-(d-3-Mercapto-2-Methylpropionyl)-l-Proline. *Spectrochim. Acta. A. Mol. Biomol. Spectrosc.* **2000**, *56* (10), 1875–1886. https://doi.org/10.1016/S1386-1425(00)00246-8.

(101) Ivanova, T.; Naumkin, A.; Sidorov, A.; Eremenko, I.; Kiskin, M. X-Ray Photoelectron Spectra and Electron Structure of Polynuclear Cobalt Complexes. *J. Electron Spectros. Relat. Phenom.* **2007**, *156–158*, 200–203. https://doi.org/10.1016/J.ELSPEC.2006.12.005.

(102) Haraguchi, H.; Fujiwara, K.; Fuwa, K. A STUDY OF COBALT COMPLEXES BY X-RAY PHOTOELECTRON SPECTROSCOPY. *Chem. Lett.* **1975**, *4* (5), 409–414. https://doi.org/10.1246/cl.1975.409.

(103) Kjær, K. S.; Kunnus, K.; Harlang, T. C. B.; Van Driel, T. B.; Ledbetter, K.; Hartsock, R. W.; Reinhard, M. E.; Koroidov, S.; Li, L.; Laursen, M. G.; Biasin, E.; Hansen, F. B.; Vester, P.; Christensen, M.; Haldrup, K.; Nielsen, M. M.; Chabera, P.; Liu, Y.; Tatsuno, H.; Timm, C.; Uhlig, J.; Sundstöm, V.; Németh, Z.; Szemes, D. S.; Bajnóczi, É.; Vankó, G.; Alonso-Mori, R.; Glownia, J. M.; Nelson, S.; Sikorski, M.; Sokaras, D.; Lemke, H. T.; Canton, S. E.; Wärnmark, K.; Persson, P.; Cordones, A. A.; Gaffney, K. J. Solvent Control of Charge Transfer Excited State Relaxation Pathways in [Fe(2,2′-Bipyridine)(CN)4]2-. *Phys. Chem. Chem. Phys.* **2018**, *20* (6), 4238–4249. https://doi.org/10.1039/c7cp07838b.

(104) Kjær, K. S.; Kunnus, K.; Harlang, T. C. B.; Van Driel, T. B.; Ledbetter, K.; Hartsock, R. W.; Reinhard, M. E.; Koroidov, S.; Li, L.; Laursen, M. G.; Biasin, E.; Hansen, F. B.; Vester, P.; Christensen, M.; Haldrup, K.; Nielsen, M. M.; Chabera, P.; Liu, Y.; Tatsuno, H.; Timm, C.; Uhlig, J.; Sundstöm, V.; Németh, Z.; Szemes, D. S.; Bajnóczi, É.; Vankó, G.; Alonso-Mori, R.; Glownia, J. M.; Nelson, S.; Sikorski, M.; Sokaras, D.; Lemke, H. T.; Canton, S. E.; Wärnmark, K.; Persson, P.; Cordones, A. A.; Gaffney, K. J. Solvent Control of Charge Transfer Excited State Relaxation Pathways in [Fe(2,2′-Bipyridine)(CN) $_4$] $^{2-}$. *Phys. Chem. Chem. Phys.* **2018**, *20* (6), 4238–4249. https://doi.org/10.1039/C7CP07838B.

(105) Kjær, K. S.; Zhang, W.; Alonso-Mori, R.; Bergmann, U.; Chollet, M.; Hadt, R. G.; Hartsock, R. W.; Harlang, T.; Kroll, T.; Kubiček, K.; Lemke, H. T.; Liang, H. W.; Liu, Y.; Nielsen, M. M.; Robinson, J. S.; Solomon, E. I.; Sokaras, D.; van Driel, T. B.; Weng, T.-C.; Zhu, D.; Persson, P.; Wärnmark, K.; Sundström, V.; Gaffney, K. J. Ligand Manipulation of Charge Transfer Excited State Relaxation and Spin Crossover in [Fe(2,2′-Bipyridine)2(CN)2]. *Struct. Dyn.* **2017**, *4* (4), 044030. https://doi.org/10.1063/1.4985017.

(106) Woodhouse, M. D.; McCusker, J. K. Mechanistic Origin of Photoredox Catalysis Involving Iron(II) Polypyridyl Chromophores. *J. Am. Chem. Soc.* **2020**, *142* (38), 16229–16233. https://doi.org/10.1021/jacs.0c08389.

(107) Paulus, B. C.; Nielsen, K. C.; Tichnell, C. R.; Carey, M. C.; McCusker, J. K. A Modular Approach to Light Capture and Synthetic Tuning of the Excited-State Properties of Fe(II)-Based Chromophores. *J. Am. Chem. Soc.* **2021**, *143* (21), 8086–8098. https://doi.org/10.1021/jacs.1c02451.

(108) Nair, S. S.; Bysewski, O. A.; Kupfer, S.; Wächtler, M.; Winter, A.; Schubert, U. S.; Dietzek, B. Excitation Energy-Dependent Branching Dynamics Determines Photostability of Iron(II)–Mesoionic Carbene Complexes. *Inorg. Chem.* **2021**, *60* (12), 9157–9173. https://doi.org/10.1021/acs.inorgchem.1c01166.